UNIVERSIDADE FEDERAL DE SÃO CARLOS

CENTRO DE CIÊNCIAS EXATAS E DE TECNOLOGIA

PROGRAMA DE PÓS-GRADUAÇÃO EM CIÊNCIA E

ENGENHARIA DE MATERIAIS

CONDUCTIVE POLYMERS DERIVED HETEROATOM DOPED CARBON

CATALYSTS FOR OXYGEN REDUCTION REACTION

Ana Maria Borges Honorato

São Carlos-SP

2020

UNIVERSIDADE FEDERAL DE SÃO CARLOS

CENTRO DE CIÊNCIAS EXATAS E DE TECNOLOGIA

PROGRAMA DE PÓS-GRADUAÇÃO EM CIÊNCIA E

ENGENHARIA DE MATERIAIS

CONDUCTIVE POLYMERS DERIVED HETEROATOM DOPED CARBON

CATALYSTS FOR OXYGEN REDUCTION REACTION

Ana Maria Borges Honorato

Tese apresentada ao Programa de Pós-Graduação em Ciência e Engenharia de Materiais como requisito parcial à obtenção do título de DOUTORA EM CIÊNCIA E ENGENHARIA DE MATERIAIS

DEDICATION

To my Husband, parents and Kids.

VITAE

Bachelor of Science in Physics - Federal University of Santa Catarina- Brazil (2010).

Degree in Physics - Federal University of Santa Catarina - Brazil (2014).

Master of Science in Mechanical Engineering - Federal University of Santa Catarina- Brazil (2013).

Folha de Aprovação

Defesa de Tese de Doutorado da candidata Ana Maria Borges Honorato, realizada em 02/12/2020.

Comissão Julgadora:

Prof. Dr. Luiz Antonio Pessan (UFSCar)

Prof. Dr. Sebastião Vicente Canevarolo Junior (UFSCar)

Prof. Dr. João Manuel Luís Lopes Maia (CWRU)

Prof. Dr. Chung-Chiun Liu (CWRU)

Prof. Dr. Lei Zhu (CWRU)

Prof. Dr. Michael Jon Ainsley Hore (CWRU)

Prof. Dr. Hossein Ghassemi (CWRU)

ACKNOWLEDGEMENTS

I want to express my gratitude to my Advisor Professor Luiz Antonio Pessan (Federal University of São Carlos). Thank you very much for your kind support and guidance throughout my journey. I also thank my advisor Professor Liming Dai for these 2 years of work in his laboratory. Thank you to Professor João Maia (Case Western Reserve University) for their support and help. It was a great privilege and blessing to be part of the Capes-CWRU Program.

Thank you very much to Theresa Claytor and Marcelo Cavallaro, that helped me in so different circumstances with warm kindness. Also, I had the good fortune of having found collaborators, colleagues and friends that gave me a good word and motivation in the hardest days. Today, I fondly remember them: Irlaine Machado, Luiz Fernando Vieira, Lucio Souza, Jucara, Lucivan Barros, Claudio, Alana,Erica, Prof. DaPeng, Jianin, Jia, Prof. Han, Prof. MingdaoZhang, ChingChing Chang, Jun Zhang, Quanbin, Dr.Shu, Linjiou, RuiGao, Wenchao, Xiaofan, among other dear friends, Special acknowledgement to Dr. Chuangang Hu.

I would like to pay special thanks to my Beloved Parents Maria and João, and the deepest sense of gratitude, thanks to My Husband Mohmmad Khalid for his patience and unconditional love throughout my Ph.D. duration.

RESUMO

CATALISADORES DE CARBONO DOPADO COM HETEROÁTOMOS DERIVADOS DE POLÍMEROS CONDUTORES PARA REAÇÃO DE REDUÇÃO DE OXIGÊNIO

A célula de combustível é um sistema de conversão de energia eletroquímica que promete produção de energia limpa e sustentável. Durante a operação, este dispositivo gera eletricidade diretamente a partir de reações eletroquímicas entre eletrodos e eletrólitos. A reação de redução de oxigênio (ORR) que ocorre no cátodo, é uma reação cineticamente lenta e necessita de catalisador para que aumente a cinética da reação catalítica de redução de oxigênio. Até agora, catalisadores baseados em platina (Pt) foram considerados os melhores para a reação de redução de oxigênio, mas o catalisador de platina sofre com três problemas: alto custo, baixa estabilidade e reservas limitadas; por isso, o uso para fins comerciais é limitado. Nesta busca, por baixar o preço e igualar o desempenho de um catalisador alternativo ao catalisador nobre, as pesquisas em nanomateriais de carbono emergiram como uma alternativa para a eletrocatálise de redução de oxigênio devido à sua excelente condutividade elétrica, grande área superficial, boa estabilidade e baixo custo. Esta dissertação compila nossa pesquisa em catalisadores de carbono dopados e co-dopados para reação de redução de oxigênio em meio alcalino. Polímeros condutores foram escolhidos devido ao baixo custo; presença de heteroátomo na unidade monômera. Para a preparação de materiais de carbono, os polímeros condutores polianilina, poli-(3,4-etilenodioxitiofeno) e politiofeno, foram sequencialmente polimerizados recobrindo nanosferas de dióxido de silício e (SiO_2) e nitreto de silício (Si_3N_4); seguidos de carbonização, resultando em materiais de carbono mesoporosos com alta área de superfície e intrinsecamente dopados com atividade catalítica de reação de redução de oxigênio em meio alcalino.

Palavras-chave: Polímeros condutores; PANI; PTH; PEDOT; SiO_2; Si_3N_4; Carbonização; Reação de redução de oxigênio.

.

ABSTRACT

Fuel cell is an electrochemical energy conversion system, that holds the promise for clean and sustainable energy source. During the operation, this device generates electricity direct from electrochemical reactions between electrodes and electrolyte. The limiting half-cell oxygen reduction reaction (ORR) that takes place at cathode is kinetically sluggish and needs catalysts to overcome the thermodynamic limitations by increasing the rate of catalytic ORR. So far, platinum Pt-based catalysts have been proven the best electrocatalyst, however, they suffer with high cost, poor stability, and limited reserves in the Earth's crust, restricting their use for commercial purpose. In this context, the search for metal-free carbon nanomaterials have emerged as an alternative to the counterpart Pt-based catalysts, especially owing to excellent electrical conductivity, large surface area, good stability, and low cost. This dissertation compiles the research work on heteroatom doped (single and co-doped) carbon catalysts for ORR electrocatalysis in alkaline medium. For the preparation of doped carbon nanomaterials, the conductive polymers, for example polyaniline (PANI), poly (3,4-ethylenedioxythiophene) (PEDOT), and polythiophene (PTH) were chosen as the precursors and sequentially polymerized by oxidative polymerization method onto silicon dioxide (SiO_2) and silicon nitride (Si_3N_4) nanospheres followed by carbonization process. The selection of conductive polymers to obtain doped carbon nanomaterials was based on the following reasons: low-cost monomers; presence of heteroatom in the monomer unit, and intrinsic conductivity. By selecting an appropriate synthetic route for the preparation of conductive polymers coated on the templates (SiO_2 and Si_3N_4), we produced high surface area, abundant mesoporous, and intrinsically doped carbon nanomaterials with ORR activity in alkaline medium.

Keywords: Conductive polymers; PANI; PTH; PEDOT; SiO_2; Si_3N_4; Carbonization; ORR

PUBLICATIONS

[1] **Ana Maria Borges Honorato**, Mohd. Khalid, Luiz Antonio Pessan, Quanbin Dai, *Nitrogen and sulfur co-doped fibrous-like carbon electrocatalyst derived from conductive polymers for highly active oxygen reduction catalysis*, **Synthetic Metals**, (2020), 264, 116383.

[2] **Ana Maria Borges Honorato**, Mohd. Khalid, Luiz Antonio Pessan, *Coral-like nitrogen doped carbon derived from polyaniline-silicon nitride hybrid for highly active oxygen reduction electrocatalysis*,
Electrochemical Science Advances, (2020), DOI: 10.1002/elsa.202000010.

x

INDEX

INDEX OF TABLES

INDEX OF FIGURES

Chapter 4

Chapter 5

Appendix

SYMBOLS AND ABBREVIATIONS

ω	Rotation speed
v	Kinetic viscosity
Φ	ORR activity parameter
A	Ampere
APS	Ammonium persulfate
BET	Brunauer-Emmett-Teller
B	Boron
C	Carbon
C_o	Concentration
CV	Cyclic voltammetry
CVD	Chemical vapor deposition
DBSA	Dodecylbenzene sulfonic acid
D_o	Diffuson coefficient
e	Electron
eV	Electron-Volt
EDOT	3,4-ethylenedioxythiophene
EDS	Energy dispersive X-ray spectroscopy
F	Faraday constant
Fe_3Cl	Iron chloride
j	Current density
H_2O	Water
H_2O_2	Peroxide
HCl	Hydrochloric acid
HF	Hydrofluoric acid
HWP	Half wave potential
I_D	Current collected at disk
I_R	Current collected at the ring
I_D/I_G	Intensity ration between D band and G band
K-L	Koutecky-Levich
KOH	Potassum hydroxide

LSV	Linear sweep voltammetry
mA	mili Ampere
N	Nitrogen
n	electron transfer number
OP	Onset potential
ORR	Oxygen reduction reaction
PANI	Polyaniline
PEDOT	Poly(3,4-ethylenedioxythiophene)
Pt	Platinum
Pt/C	Platinum/Carbon (20 wt%)
Raman	Ramman spectroscopy technique
RHE	Reversible Hydrogen electrode
RDE	Rotating disk electrode
RRDE	Rotating ring-disk electrode
RPM/rpm	Rotation per minute
S.A	Surface area (m^2/g)
SEM	Scanning electron microscopy
SiO$_2$	Silicon dioxide (Silica)
Si$_3$N$_4$	Silicon nitride
TEM	Transmission electron microscopy
V	Volts
vs	Versus
XRD	X-ray diffraction
XPS	X-ray photoelectron spectroscopy

1 INTRODUCTION

Over the past decades, enormous efforts have been devoted on developing renewable clean energy conversion and storage systems, such as fuel cells and metal-air batteries. [1]-[6] One of key processes of these clean energy systems is the oxygen reduction reaction that is a cathodic half-reaction of fuel cells and metal air batteries. [4] ORR is a sluggish kinetic reaction which proceeds by oxygen containing intermediates adsorbed on the active sites of electrocatalyst. [5] Therefore, the ORR performance of an electrocatalyst greatly depends on the interaction strength between active sites and oxygen intermediates. In general, the leading ORR cathodic materials are based on platinum (Pt), since Pt-based catalysts exhibit most positive onset potential and half wave potential for catalyzing ORR. Unfortunately, due to unaffordable cost and low abundance in nature, Pt-based catalyst renders their widespread commercial utilization impractical. [5], [6] Therefore, the development of substitutes for the Pt-based catalysts is imperative to realization of oxygen related energy conversion and storage systems at large scale. [8]-[10]

Among the many families of materials that have been scrutinized as catalysts for ORR, doped carbonaceous materials have appeared as promissory low cost and abundant materials. [11]-[12]

Recently, carbon based catalysts, with properly designed structures and appropriate doping / co-doping have been recognized as one of the highly competitive candidates to Pt-based catalysts, owing to their remarkable ORR activity. [11]-[12]

Optimizing the morphological structure and synergistic effect of co-doping in carbon network are cardinal strategies to achieve ORR activity near to benchmark Pt/C. For example, Qiu et al. synthesized carbon nanocages with diameter of 50 nm and shell thickness of 4 nm, using the precursors of polyethylene oxide-polypropylene oxide-polyethylene oxide (PEO-PPO-PEO) three-block copolymer (F127) and Zn $(OH)_2$ for ORR catalysis in alkaline solution. Taking the advantage of high surface area (1011 m^2 g^{-1}), optimized pyrolysis condition, and unique morphological structure, the as-prepared carbon nanocages showed excellent onset potential and half wave potential of 0.89 and

0.71 V, respectively. **[13]** Similarly, Zhang et al. prepared nitrogen doped carbon nanoflower using the precursors of pyrrole, aniline, and phenanthroline. The optimal catalyst derived from phenanthroline at 900°C (N-CNF-PHEN-900) containing largest specific surface area (1039 m^2 g^{-1}), demonstrated superior ORR activity by surpassing the benchmark Pt/C catalyst with 30 mV half wave potential in alkaline solution. **[14]**

Building hierarchical porous doped carbon has shown benefit in electron transfer and mass diffusion as well as increasing the surface/volume ratio and density of active sites for enhancing the catalytic performance of the catalyst. In this context, strategically preparing hierarchical porous doped carbon from polymer precursors by combining polymer precursors with different heteroatoms allows in situ doping and co-doping, and enables tailoring optimized nano-architectures. Such features promise to render high ORR activity. **[11]- [14]**

Based on these premises, our research focused on developing doped and co-doped carbon materials with activity towards ORR, derived from low-cost conductive polymers. This thesis provides a brief review of the literature, compiles the synthesis methods, physical and electrochemical characterizations of the produced catalyst materials.

2 LITERATURE REVIEW

2.1 Oxygen reduction reaction process

The ORR is a complex process which involves different intermediates that go through different pathways of adsorption/desorption in alkaline or acidic medium. There are two possible pathways, by which ORR processes, either *via* four electrons or two electrons pathways. The four-electron pathway is preferred in electrocatalytic ORR for fuel cell applications due to faster reduction rate. The two-electron pathway involves production of peroxide species and its re-adsorption. The two-electron path is not always unfavorable, since the H_2O_2 is a key oxidizing agent in green chemistry and environmental applications and can be directly produced by electrochemical reduction of O_2. Generally, the electrocatalytic test for ORR is operated under O_2 saturated acid/base electrolytes using a rotating disk electrode (RDE). The catalytic performance is evaluated by onset potential and half-wave potential ($E_{1/2}$) using the techniques of CV and LSV.

The four-electron pathway combines oxygen with electrons and protons directly, where hydrogen comes from oxidation on the anode to produce water as the end product. The two-electron pathway consists of formation of peroxide ions as intermediates and a second step in which the peroxide ions must be re-adsorbed and reduced at the electrode. **[7],[8]** Thermodynamic potentials at standard conditions of oxygen reduction reaction in alkaline medium versus reversible hydrogen electrode (RHE) at 25℃ give an idea of the energy involved in each step of the specific pathway. **[9],[10]**

In basic medium;

Four-electron pathway:

$$O_2 + 2H_2O + 4\ e^- \rightarrow 4OH^- \qquad E^o = 0.401 \quad V \qquad (2.1)$$

Two-electron pathway, with production of intermediate species:

$$O_2 + 2H_2O + 2\ e^- \rightarrow HO_2^- + OH^- \quad E^o = 0.080\ V \qquad (2.2)$$

$$HO_2^- + H_2O + 2\ e^- \rightarrow 3OH^- \qquad E^o = 0.0880\ V \qquad (2.3)$$
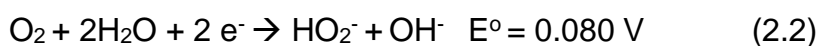
In acid medium;

Four-electron pathway:

$$O_2 + 4H^+ + 4e \rightarrow 2H_2O, \quad E^o = 1.229 \text{ V} \qquad (2.4)$$
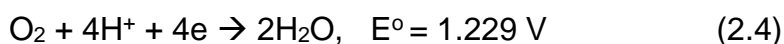
Two-electron pathway, with yielding H_2O_2:

$$O_2 + 2H^+ + 2e \rightarrow H_2O_2, \quad E^o = 0.695 \text{ V} \qquad (2.5)$$
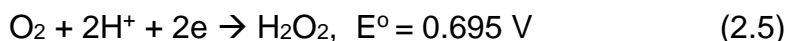
Due to the strong energy (498 kJ mol^{-1}) between O-O molecule, it is very difficult to break this bond. The efficient catalyst lowers the energy barrier for bond activation and cleavage in order to facilitate ORR electrocatalysis.[9] The kinetics of cathodic ORR is six order of magnitude lower than hydrogen oxidation at the anode, thus, ORR suffers with high overpotential. The overpotential might also result from electrolyte resistivity, mass transport limitations, low affinity of catalyst sites and other hindering effects, and energetic and kinetic barriers. [9]

The oxygen reduction reaction in aqueous electrolyte is a dynamic process, in which firstly the oxygen molecules must be adsorbed at the surface of the catalyst at the cathode. The site where the oxygen molecule is adsorbed is called an active site and can result from the presence of heteroatoms or defects. After adsorption at the active site and protonation (protons from anode) of oxygen molecule, its bond is broken, and various intermediate species are involved during the process.

To describe the mechanistic process, consider an active site given by an asterisk (*) on the surface of electrocatalyst, the intermediate adsorbed species are OH^*, HOO^*, O^*, and (l) and (g) refer to liquid and gas phases. The electrons come from the other half-cell anodic reaction and must transfer to the oxygen molecule that was adsorbed at the catalyst site. The process can be associative (eq. 2.6) or dissociative (eq. 2.11). [10]

Electrons that come from the anode are responsible for breaking the O-O bond and release of OH^- ions. When the process occurs directly, four electrons will break the O-O bond, releasing 4 OH^- ions (eq. 2.13, 2.14, 2.15).

When the reaction happens via the two-electrons path, firstly, the two electrons turn oxygen molecule into peroxide ions (HO_2^-), then the adsorbed HO_2^- species convert into water by taking the next two electrons (eq. 2.7 to 2.10). [10]

Mechanism via association involving peroxide ions:

$O_2(g) + * \rightarrow O_2^*$ (2.6)

$O_2^* + H_2O(l) + e^- \rightarrow HOO^* + OH^-$ (2.7)

$HOO^* + e^- \rightarrow O^* + OH^-$ (2.8)

$O^* + H_2O\ (l) + e^- \rightarrow HO^* + OH^-$ (2.9)

$HO^* + OH^- \rightarrow * + OH^-$ (2.10)
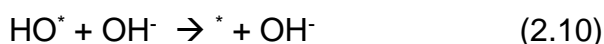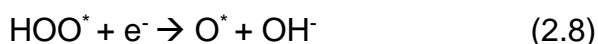
Mechanism via direct dissociation of oxygen:

$O_2(g) + * + * \rightarrow O^* + O^*$ (2.11)

$O^* + H^+ + e^- \rightarrow HO^*$ (2.12)

$HO^* + H^+ + e^- \rightarrow * + H_2O\ (l) + *$ (2.13)

$O^* + H_2O\ (l) + e^- \rightarrow HO^* + OH^-$ (2.14)

$HO^* + OH^- \rightarrow * + OH^-$ (2.15)
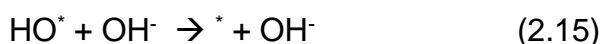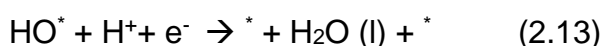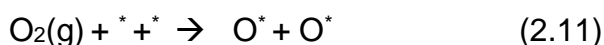
The rate-determining step is the elementary reaction presenting minimum free energy, and commonly identified either as the adsorption of O_2 as HOO^* (eq.2.7 for associative, or eq. 2.12 and 2.14 for dissociative) or desorption of OH^* as water (eq.2.10 for associative, and eq. 2.3).

2.1.1 Koutecky-Levich equations

In order to measure the electrochemical properties of the catalysts during ORR, standard tests are performed in three electrodes cell setup with the use of a ring-disk electrode.[10] The electrochemical measurements of current at the disk can be related to Koutecky-Levich equations (eq. 2.16 and 2.17):

$J^{-1} = J_K^{-1} + J_L^{-1} = J_K^{-1} + (B\ \omega^{1/2})^{-1}$ (2.16)

$B = 0.2\ n\ FD_O^{\ 2/3} v^{1/6} C_O$ (2.17)

where ω corresponds to rotation speed in rpm, 0.2 is a coefficient related to the angular rotation speed in rpm, J is current density, B is the reciprocal to slope.

For the 0.1 MKOH electrolyte, C_O is the bulk concentration of oxygen (1.2 10^{-6} mol cm^3), D_O is the oxygen diffusion coefficient (1.9 x 10^{-5} $cm^2 s^{-1}$), and v is the kinematic viscosity of electrolyte (0.01 $cm^2 s^{-1}$). With the use of these equations, it is possible to construct the Koutecky-Levich plot, and calculate the electron transfer number.

When the current is measured by electrode containing ring and disk, it is possible to calculate the electron transfer number and peroxide production (% H_2O_2) (eq. 2.18 and 2.19) :

$$n = 4 * I_D * (I_D + I_R/N)^{-1} \qquad (2.\ 18)$$
$$\% H_2O_2 = 200 * I_R/N * (I_D + I_R/N)^{-1} \qquad (2.\ 19)$$

where I_D and I_R are experimental data and stand for the currents collected in the disk and ring, N is the current collection efficiency of the ring (values vary according to the material), and 4 and 200 are coefficients for adjustment of equations.

2.2   Metal-free carbon based electrocatalysts for ORR

Dai and coworkers introduced vertically aligned nitrogen containing carbon nanotubes (VA-NCNTs) as the first metal-free doped carbon catalysts for ORR in 2009. The 'metal-free' VA-NCNTs were able to catalyze ORR even better than benchmark Pt/C catalyst due to active catalytic sites resulting from the changes in the sp^2 arrangement of pristine carbon nanotubes by the introduction of nitrogen atom dopants, which produced a substantial positive net charge. [6] Since then, various research strategies have been developed to prepare heteroatom doped carbon electrocatalysts. [11]

It is known that the doping in the carbon network with heteroatoms, possessing various electronegativities, different atomic sizes, and binding states, alters the electronic properties by changing the charge distribution and spin

density on adjacent carbon atoms. Additionally, heteroatom doping in carbon lattice tunes the feature of hydrophobicity/hydrophilicity of carbon and can also contribute in formation of porosity and channels. **[11],[12]**

Therefore, the efficient intrinsic ORR performance of doped carbon results from the combination of electronic and morphological features acquired during the synthetic process. It is also known that the heavily doped carbon materials do not reach the best performance unless the high surface area of catalyst material is achieved. Because the ORR occurs on the surface of the catalyst, the more exposed active sites, the better ORR activity. Producing carbon materials with large surface area and optimal porosity facilitate the mass transfer and high contact of electrolyte and active sites. **[11]**

Among the various heteroatoms doped carbon, nitrogen doped carbons have been widely studied, due to its high catalytic activity. Nitrogen shows nearly the same atomic radius as a carbon atom and is more electronegative (N: 3.04) than carbon (C: 2.55), creating a nonhomogeneous charge distribution and enlarging spin density. These modifications of electronic properties of carbon lattice promote the interaction between the oxygen intermediates during reaction and result in high oxygen reduction reaction activity. **[12]**-**[15]**

Nitrogen atoms can form different coordination with the carbon lattice. There are three types of coordination that result in active sites, namely pyridinic-nitrogen, pyrrolic-nitrogen, and quaternary-nitrogen. Kondo and coworkers defined the mechanisms for ORR in nitrogen doped carbon. The nitrogen atoms having high electronegativity causes a covalent electron transfer from the neighbor carbon atom, leaving it with net positive charge density, and creating active sites for ORR. The adsorbed oxygen molecule is protonated following either via four-electron path or two-electron path. The four-electron pathway directly converts oxygen molecule to water molecule. In this case two protons attach to the oxygen atoms and break the bond O-OH producing OH species. The additional proton reacts with the OH to form water, without sub-products. In a two-electron pathway, H_2O_2 is evolved as an intermediate species. The adsorbed OOH reacts with one proton and forms H_2O_2, which is re-adsorbed and reduced with two protons to form water. **[16]**

Pyridinic-nitrogen weakens the oxygen bond of the oxygen molecule by bonding oxygen with the carbon neighboring with nitrogen. **[16]**,**[17]** Pyridinic-nitrogen influences the onset potential, whereas the quaternary-nitrogen (or graphitic-nitrogen), influences the limiting current density. **[16]** Quaternary-nitrogen offers one electron to each carbon and donates one electron to the sp^2 carbon. Overall, these three types of nitrogen species promote ORR: pyridine, pyrrole, and quaternary. **[18]**

Liu and coworkers identified pyridinic-nitrogen and pyrrolic-nitrogen catalytic sites as more favorable for a four-electron path, whilst the quaternary-nitrogen tends to produce a two-electron pathway. Some researchers identify the ORR most active sites as follows: pyridinic-nitrogen (higher activity- four electron path) > pyrrolic-nitrogen > quaternary-nitrogen (two-electron path). **[18]** However, it is still debatable which is the most active site in nitrogen doped carbon, and furthermore ORR itself might induce transformation from pyridinic-nitrogen and quaternary-nitrogen to pyrrolic-nitrogen species. **[18]**, **[19]**

The main reason for considering pyridinic-nitrogen, the most active site is because of its reduction of oxygen molecule via a four-electron path, whereas, quaternary-nitrogen tends to indirect two-electron path. **[20]** But, most mechanistic studies use a "reductionist methodology", that correlates activity with the amount of a specific kind of nitrogen. One can also take into consideration that pyridinic-nitrogen and quaternary-nitrogen can impact each other's activity due to the synergistic effect generated from their different electronic arrangement. **[20]**

Identification of which exact nitrogen species is an actual active site is not an easy task, since ORR activity depends on multiple structural parameters, defects, and degree of graphitization. Li and research group tried to establish a method for controlling the nitrogen species doped into the carbon, however, they found variations batch-to-batch. **[20]** They also identified that the most active site among the nitrogen species in carbon materials tested in alkaline electrolyte was actually the quaternary-nitrogen instead of pyridinic-nitrogen. It is general consensus that the less active site is oxidized -nitrogen specie. **[20]**, **[21]**

Another important study published by Yao and Dai in 2019, showed that the defects also impart catalytic activity to carbon materials. Such findings, raised the question, if the highest catalytic activity identified in diverse nitrogen-doped carbons, were actually imparted from the presence and synergy of the dopants and defects. **[22]**, **[23]**

The study directly compared the catalytic activity arising from pentagon defects with the catalytic activity of pyridinic-nitrogen sites. The presence of defects produced different results; when they were in bulk, they decreased the conductivity resulting in lower performance, however, when located at the edges or at exposed surfaces, defects were highly active sites, and even better catalytic sites than pyridinic-nitrogen sites. **[22]**

Beyond nitrogen moieties, other heteroatoms were doped into the carbon lattice for preparation of electrocatalysts towards ORR. Among the most common elements used are boron, sulfur and phosphorus. **[24]** A volcano-plot was proposed by Xia and coworkers to relate the intrinsic properties of different heteroatom-dopants with an activity descriptor for the ORR performance of doped carbon materials. **[25]**

Considering that the overpotential is the potential at which the energy barrier of the reactions is conquered, the lower the overpotential, the lower is the energy required to overcome such barrier and proceed the reaction. Therefore, thermodynamically, the lower the overpotential, the better the performance. Calculating the free energy and overpotentials of ORR reactions of a list of elements (N, B, P, S, Si, Se, F, Cl) can be useful to identify the rate-limiting step by selecting the maximum overpotentials in elementary reaction steps. The ORR activity descriptor Φ for the p-block element-doped graphene structure was based on the relation between catalytic activity and intrinsic properties of dopants. The intrinsic properties of dopants were described using E_X and A_X. E_X is the ability of acquiring electrons when covalent bonds are formed (electronegativity), and A_X is the energy given off when a neutral atom gains an extra electron to form negatively charged ions (electron affinity). The descriptor $\Phi = E_X / E_C \times A_X / A_C$ is a dimensionless factor consisting of the product between the relative electronegativity and electron affinity. By plotting this descriptor in relation with

the best performance, it is possible to visualize a volcano plot. The elements located in the positions Φ = 1-3, represent the best dopant elements to produce best performance. The lower limit of ORR overpotentials for heteroatom doped graphene structures versus the descriptor is shown in the **Figure 2.1**. **[25]**
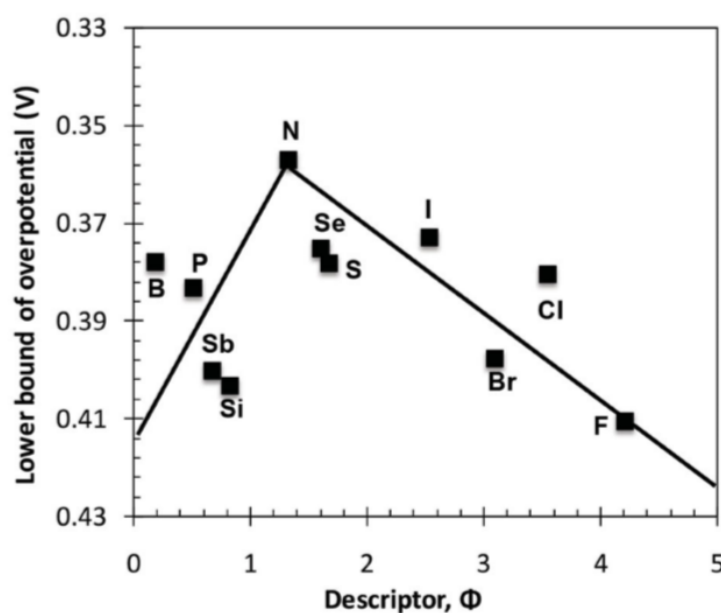
Figure 2.1 - The lower limit of ORR overpotentials for heteroatom-doped graphene structures. Reproduced with permission, copyrights to Wiley and Sons **[25]**

Nitrogen, at the top of the volcano is considered the best dopant of graphene, followed by boron, sulfur, and phosphorus. Such dopants are among the most common elements exploited as dopants in single doped and co-doped carbon materials for enhanced ORR. **[25]**

In the case of sulfur-doped carbon materials, the nature of active sites is different from that of the sites present in nitrogen-doped carbon. Because the atomic radius of the sulfur atom is much larger than that of a carbon atom, when sulfur is introduced into carbon materials, it causes distortions in the carbon lattice. According to the synthetic approach, sulfur atoms can exist as adsorbed to the catalyst surface, substituted at the edges, forming S/S-oxides and sulfur clusters connecting to layers of nanocarbons (such as in graphene case). **[26]** There is no significant change in charge distribution for sulfur-doped carbon,

because the electronegativity of sulfur is similar to the carbon atom (2.5), therefore, mostly sulfur dopants are located at the edges or defective regions due to its large size. **[27]**

The main cause of catalytic activity in sulfur doped carbon materials is attributed to enhancement in spin density of carbon atoms neighboring the sulfur atoms and favored interactions with oxygen due to large size of sulfur atoms. **[27]**

The introduction of sulfur atoms into the carbon matrix introduces strain and defects in the carbon lattice, which promote charge localization and enhance the adsorption of oxygen molecules. The ORR process in sulfur-doped carbon starts with the oxygen molecule being adsorbed on the catalytic sites, which are the carbon atoms adjacent to the sulfur atom or the sulfur atom itself. This is followed by protonation, and breaking of the O-O bond. Following, ORR either proceeds by a four-electron path or two-electron path as previously explained. **[27]**-**[29]**

Boron is another heteroatom that is generally used in co-doped catalysts towards ORR. The introduction of boron in nitrogen doped material has been reported to produce enhanced catalytic activity, by changing electronic arrangement in nitrogen doped carbon matrix. Also, its presence into the carbon lattice enhances graphitization, which means increasing the conductivity. **[30]** Owing to the smaller value of electronegativity of boron with respect to carbon, the presence of boron atoms in the carbon lattice creates positive charged sites, which attract the oxygen molecule. The adsorption of oxygen molecules occurs at the boron atom itself due to its positive charge in relation to the adjacent carbon atoms. **[31]** The π^*-electrons accumulated in the $2p_z$ vacant orbital of boron dopant in the conjugated system can easily be transferred to the adsorbed oxygen molecule. This transferred charge elongates the O-O from 1.21 Å to 1.32 Å, and weakens the oxygen bond within the oxygen molecule, therefore, promoting ORR. **[31]**

Boron atoms have lower electronegativity than carbon atoms and when introduced among carbon neighbors, the boron moieties become positively polarized, which attracts the negatively charged oxygen molecules.**[32]**,**[33]** As

the oxygen molecules approach the catalytic sites, the adsorption distance is decreased, resulting in the chemisorption of oxygen molecule. **[34]**

Boron doped graphene presented four different atomic arrangements, which have higher oxygen adsorption than non-doped graphene. Theoretical calculations demonstrated that substitution of carbon atoms with boron atoms in graphene lattice, greatly affects its interactions with oxygen molecules. **[35]**

During ORR, when two oxygen molecules directly bond with boron, they cause two boron-carbon bonds to break, resulting in a highly oxidized boron. When one oxygen molecule bonds with boron, the configuration is more stable. In both cases, the resulting dissociation of oxygen and bonding with boron atoms are exothermic processes. On the other side, such exothermic processes from oxygen dissociation during its bonding with boron -doped graphene are not observed in pristine graphene. **[35]** Through computational studies, Ferrighi and coworkers showed that there are two possible pathways for oxygen reduction reaction in boron doped graphene, the associative pathway (two-electron pathway) and dissociative pathway (four-electron pathway). The associative pathway is energetically more favorable than the dissociative, which explains why hydrogen peroxides species are formed before completing ORR. **[36]** They also showed that while breaking the oxygen-oxygen bond is an exothermic process, binding of oxygen molecule at surface of boron doped graphene is endothermic, and there are many intermediate uphill steps that play energetic role hindering the straight conversion of oxygen molecules into water. When boron and nitrogen are co-doped into the carbon, they produce electron rich (N) and an electron deficient (B) sites in relation to the ocean of carbons that constitutes the lattice. **[36]**

Depending on the configuration, boron and nitrogen will enhance or not the catalytic activity towards ORR. When they bond with each other they will not produce catalytic performance towards ORR, due to the compensation effect of a n-type and p-type dopant. Therefore, to produce higher catalytic activity towards ORR, boron and nitrogen moieties must be bonded with the carbon atoms neighbors in the co-doped material. **[36]**

In conjunction with heteroatom doping, it is also crucial to design the structure of nanocarbons. Highly porous structure of nanocarbon provides efficient mass transport/diffusion of electrons and ions providing better electrolyte permeability, resulting in better ORR performance. **[37]**

The relationship between microstructure and electrocatalytic properties takes an important part in determining the final ORR. Macropores can work as buffering reservoirs where the electrolyte can access to the interior surfaces within shorter distances, mesopores can provide a large accessible surface area for ion exchange and transport. Therefore, hierarchical doped carbons with porous structures are considered attractive for enhancing catalytic activity. **[39]**,**[40]**

Co-doping is a known strategy for enhancing catalytic activity. Nitrogen and sulfur specially, have been considered a pair of dopants capable to boosting the ORR activity in carbon materials. **[38]**,**[39]** Co-doping of carbon with sulfur and nitrogen, requires special attention, because in one side, the content of sulfur may increase the content of pyridinic-nitrogen during carbonization, but on the other side, sulfur contributes for the decomposition of carbon lattice during the pyrolysis and even lowering nitrogen contents. **[41]**

When it comes to sulfur and nitrogen co-doping, certain configurations such as S=C-N and C-S-C enhance the ORR performance, while the oxidized sulfur (-C-SO$_X$-C-) was assigned as an ineffective site. Sulfur and nitrogen co-doping increases the selectivity towards ORR by lowering the energy barrier of both oxygen adsorption and adsorbate hydrogenation to form OOH, because it provides robust electronic interactions and tunes hydrophobicity of the carbon materials. **[42]**

According to Sun and coworkers, the nitrogen-sulfur co-doped carbon in which the elements sulfur and nitrogen were near to each other led to more active sites and a synergistic effect due to greater electron density.**[38]** Complementary, the overpotentials for nitrogen-doped carbon, isolated nitrogen and isolated sulfur doped carbon and coupled nitrogen-sulfur-doped carbon were calculated and the respective values of overpotentials were measured to be 0.403 V, 0.270 V and -0.004 V at the electrode potential 0 V. The lowest value of overpotential belonged

to coupled nitrogen-sulfur-co-doped carbon, which showed best catalytic activity for ORR, indicating that the co-doped regions have greater electron density, and more active sites than the one with only one kind of isolated heteroatom. [43]

Due to the importance of doping and co-doping in carbon, various techniques have been used to preparation of these materials, including hydrothermal reaction, microwave assisted methods, solvothermal treatments, chemical vapor deposition, thermal annealing, microbial method, refluxing and etc. [44]-[47]

The synthesis process is crucial in determining the ORR catalytic activity of the material; therefore, it is desirable to invest efforts in the co-doping strategy (for tuning electronic features) and in the preparation of carbon materials with high specific surface area and appropriate porosity, thus maximizing the presence of active sites in the bulky and surface of catalyst material. [43]-[46]

2.3   Conductive polymer precursors

As previously discussed, in-situ doped and co-doped carbon materials with homogeneously distributed active sites, high specific surface area and appropriate porosity, favor higher catalytic activity towards ORR. [44]-[46] And for the development of ideal doped/co-doped carbon catalysts, it is very advantageous to have a diverse group of precursors from inexpensive sources.

Synthetic polymers are perfect candidates, being considered low-cost, abundant, containing heteroatoms moieties and being versatile for preparation of varied nanostructures. After polymerization, the polymeric structures containing unsaturated bonds can be converted into doped / co-doped carbon materials via thermal treatment. [44], [45]

Pyrolysis of conjugated polymers possessing heteroatoms in their chain backbone creates different species of dopants, defective sites, edge states, porosity and surface area, which are beneficial for catalysis. The conductivity and active sites of the as-produced carbon materials are intrinsic properties resulting from the polymer precursor and synthetic protocol. [46]

The various kinds of structures and chemical compositions are not absolutely controllable, because of the complexity involved during polymerization, and posterior steps of pyrolysis and activation. During pyrolysis, some polymer may degrade and gasify easier than others, requiring more complex pre-treatments before the thermal treatment. Therefore, choosing precursors which can crosslink during carbonization is beneficial. This stabilization step prevents depolymerization and gasification and allows the crosslinked polymer to turn into the carbon structure as the thermal treatment progresses instead of being decomposed into smaller molecules. **[47]**, **[48]**

The preparation of heteroatom doped carbons from polymers requires precursors with abundant number of functional groups. The heteroatoms already present in the polymers are incorporated into the carbon structure; thus, the preparation does not require pos-treatment for doping. The content of heteroatoms may vary according to the polymerization process, temperature, time, atmosphere used during the pyrolysis and pos-treatments. The specific position of the heteroatom into the carbon lattice is not easy to tune and it is known that the temperature of thermal treatment is not the only factor controlling the state of heteroatoms. During the polymerization process, the use of rigid or inorganic templates affects the development of the polymeric structure and during carbonization, it may affect the final carbon structure. Templates can also be employed to maximize the surface area, pore structure, and also nanostructure. Also, removal of the template during post treatment, may change or distort the final structure. Using silicon nitrides and silicon oxides during the synthesis of polymers, allows to produce materials with unique morphological structures.

Silica cores used during the polymerization reactions are beneficial because they work: as electrostatic attractive surfaces for the anchoring of the monomers and guide the growing chains of polymer during polymerization; to reduce the agglomeration and increasing the surface area/volume ratio; and to avoid the collapse of polymeric structure during the process of carbonization at high temperatures, aiding it to keep its shape. **[49]**

2.3.1 PANI as precursor for nitrogen doped carbon

PANI is a versatile conductive polymer and used for diverse energy applications. Upon pyrolysis, PANI is converted into nitrogen-doped carbon. The types and percentage of nitrogen species within the carbon lattice are due to decomposition and re-arrangement of the PANI during carbonization.[50]

According to literature, when PANI is carbonized at temperatures below 700℃, it produces high content of pyrrolic-nitrogen, while at higher carbonization temperatures (> 700℃), it produces pyridinic-nitrogen. Graphitic-nitrogen arises from the conversion of pyrrolic-nitrogen and pyridinic-nitrogen into this form at higher temperatures ~ 900℃. [50], [51]

Annealing treatment of PANI at temperatures higher than 800℃, results in shrinkage of polymeric chains, reorganization of carbon-carbon and carbon-dopants bonds, and eruption of gases producing interior porosity. [51], [52] The as-produced carbon material demonstrates high conductivity, which plays crucial role in enhancement of ORR activity. After pyrolysis, PANI retains its bulk morphology producing different kinds of structures.

Higher carbonization temperature favors higher conductivity but reduces the content of nitrogen dopant. Additionally, the defects sites and graphitization also play vital roles in improving the catalytic activity, which can be varied by changing the annealing temperature. [52]-[54]

When PANI was carbonized at temperatures of 600℃ and 800℃, nitrogen species were predominantly pyrrole-nitrogen, pyridone-nitrogen and pyridinic-nitrogen, while quaternary-nitrogen species were not identified, however low temperatures of carbonization fail in producing carbon with high graphitization and good conductivity. [53] The carbon catalysts produced with carbonization of PANI at 600℃ and 800℃, showed low catalytic activity towards ORR, reaching onset potential values of only 0.66 V vs RHE (600℃) and 0.74 V vs RHE (800℃). [53]

Three types of nitrogen species were observed in carbon produced by carbonization of PANI at temperatures higher than 800℃, such as pyridinic-nitrogen, pyrrolic-nitrogen, and graphitic-nitrogen, according to the previously reported works. [52],[54]

Pyridinic-nitrogen and graphitic-nitrogen species are beneficial for high ORR activity, and in order to produce such species, the carbonization of polyaniline at temperatures higher than 800℃, seems to be a reasonable choice. Besides that, temperatures of carbonization higher than 800℃ produce carbon materials with good conductivity, and may cause defects that also work as active sites for ORR. **[51]**, **[55]**-**[57]**

Figure 2.2 represents pyrolysis of PANI producing different nitrogen-species: pyrrolic-nitrogen, pyridinic-nitrogen, quaternary-nitrogen and oxidized-nitrogen.
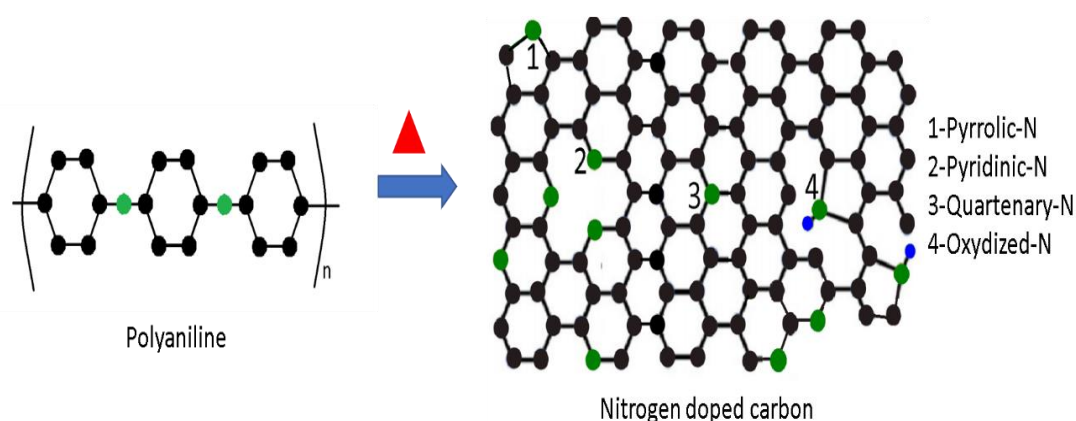
Figure 2.2 - PANI conversion into nitrogen doped carbon producing different nitrogen species: pyrrolic-nitrogen, pyridinic-nitrogen, quaternary-nitrogen and oxidized-nitrogen. **[51]**, **[55]**

2.3.2 Polythiophene and PEDOT as precursors for sulfur doped carbon materials

The "in situ" doping strategy for preparation of sulfur-doped carbons requires carbonization of polymers containing sulfur functional groups. Because, in the polymer precursor the heteroatoms are distributed homogeneously, upon pyrolysis, it is expected that sulfur species also will be homogeneously distributed in the doped carbon material. The active sites produced by the presence of

heteroatoms are located beyond the surface and can be found intrinsically anchored in the inner channels and pores of the doped carbon material. **[58]**

Pyrolysis of polythiophene produces sulfur-doped carbon with good conductivity, porosity, high surface area per unit volume, high density of active sites and mainly -S-C- bonds. Pyrolysis and activation processes determine the surface area and pore volumes.**[58]**, **[59]** Sulfur-doped carbon materials with different properties have been prepared from polythiophenes using different carbonization temperatures.**[58]**

According to literature, carbonization temperature of 900℃ is used to obtain highly graphitized sulfur doped carbon with high surface area, however not achieving high pore size distribution. **[58]** Carbonization temperatures of 600ºC and below were found not suitable to convert polythiophene into sulfur doped carbon materials for ORR applications.

High surface area and high graphitization are extremely important features in a carbon-based electrocatalyst, because they benefit high electron access and mass transfer, allowing more interface for contact between active sites and ions. In order to achieve these features, besides high carbonization temperatures, sometimes activation processes are necessary.

During carbonization, the curing of polymer chains takes place, in which the linear polythiophene forms disulfide bridges, sulfone, and oxidized groups. At the same time that, there is loss of sulfur content with eruption of gases, it is through this process that the porous structure is formed. **[58]**-**[61]** Because of the size of sulfur atoms, the thiophenic configuration of sulfur atoms (-C-S-C-) is normally observed in the edges of the materials, and sulfur atoms presented into the core of carbon lattice produce strain and defects. The sulfur doped carbon resulting from the dynamic transformation during pyrolysis is different from the polymer precursor in terms of its electronic and physical properties. **[62]**-**[64]**

Recently, sulfur doped carbon was prepared from flame synthesis of polythiophene. **[65]** They found excellent ORR activity with an onset potential of -0.16 V vs Ag/AgCl in 0.1M KOH and high tolerance for methanol poisoning effect. They attributed the performance of catalysts due to the n-type dopant

behavior of sulfur. The optimal presence of sulfur in carbon materials increases the conductivity of amorphous carbon. **[60]**

High surface areas and abundant porosity can be obtained using special sacrificial templates during polymerization with posterior removal. Although it is rather preferable to have a straightforward synthetic process, this step seems a necessary evil to enhance activity. **[66]**-**[68]**

Sevilla and coworkers reported polymerization of polythiophene using $FeCl_3$ as an oxidizing agent, followed by carbonization and activation process at temperature between 650-800℃. As a result, highly porous sulfur doped carbonaceous materials were obtained. **[60]** Thiophene was also polymerized inside SBA 15 and KIT-6 template and carbonized between 600-800℃, producing highly porous carbon, and sulfur content between 0.9-6.1%, respectively. **[68]** Shin and coworkers prepared templated mesoporous sulfur doped carbons, from polymerization of thiophene-methanol also using oxidizer $FeCl_3$, followed by pyrolysis. They carbonized polythiophene - methanol coated SBA15 templates in a range of temperatures 700-900℃, obtaining content of sulfur between 7-4% respectively. **[67]** Although the surface area increases with higher carbonization temperatures, the content of sulfur dopant decreases with increasing temperature of carbonization. **[67]** Single sulfur doped graphene was prepared by Yang and coworkers using graphene oxide and benzyl disulfide annealed at 600℃, 900℃ and 1050℃. The respective contents of sulfur were found 1.53%, 1.35%, and 1.30%, with the oxygen reduction peak potential values of -0.32, -0.31, 0.29 V vs Ag/AgCl, and the electron transfer numbers of 2.51, 3.27, and 3.82, respectively. **[69]**

In general, the sulfur content decreases with increasing temperature of carbonization. To solve this issue, a strategy for retaining the dopants during the harsh conditions of carbonization consists in confining the polymer precursor inside templates pre-carbonization. Removing the templates, after carbonization, through activation process also causes loss in the content of dopants. **[60]**, **[69]**

Figure 2.3 shows the schematic representation of the conversion from polythiophene into sulfur-doped carbon.
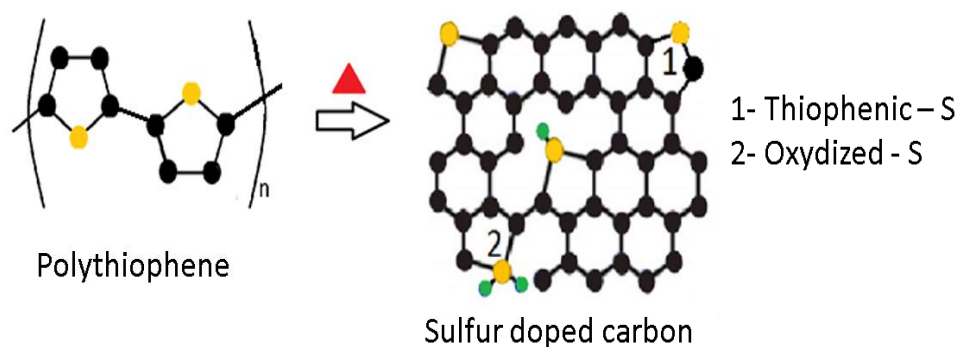
Figure 2.3 - Polythiophene conversion into sulfur-doped carbon containing thiophenic-sulfur and oxidized-sulfur species. **[62]**

Sulfur doped carbonaceous materials can also be produced via carbonization of PEDOT in the same way as produced by carbonization of polythiophene. According to literature, carbonization at 800℃ produces thiophene-like (-S-C-) and oxidized (C-S-O$_x$) species. **[70]** PEDOT was prepared via oxidative polymerization for applications as Lithium -ion battery anodes. **[71]**, **[72]** And via carbonization at 700℃, PEDOT was transformed into sulfur doped carbon with enlarged carbon interlayers (due to the presence of large sulfur atoms≈ 0.39nm), which benefits its catalytic properties. **[71]**

PEDOT films produced by electro-polymerization were carbonized in the range of temperatures of 600-1100℃. Sulfur content (in the resulting carbon) varied according to the carbonization temperatures, from 2% sulfur (1100℃), up to 26% sulfur (600℃), while raw PEDOT sulfur content was 18%. Once again, sulfur contents dropped with increase in carbonization temperatures, but on the other hand, the carbon content was found higher for carbonization at higher temperatures. **[73]** From the XPS analysis, the main sulfur species incorporated into carbon after carbonization of PEDOT at 800℃ and 900℃ were thiophenic -like (-S-C) species, which are desirable when planning to obtain catalysts toward ORR. The conductivities also increased with higher temperatures of carbonization. **[73]**

2.3.3 Boric acid and sucrose as precursors for boron doped carbon

The selection of low-cost, and environmentally friendly precursors with the ability to produce doped materials with good activity towards ORR has been a real challenge for preparation of boron doped carbon materials. Precursors are not only the immediate sources of carbon and dopant (in this case boron), but also the generator of final structure via the synthetic method. Among the most common precursors for preparation of boron doped carbons, are trimethyl boron [74], Borax ($Na_2B_4O_7$) [75], orthoboric acid and boric acid. [76]

Hydrothermal carbonization method using water, sucrose/glucose and boric acid followed by carbonization is reported in literature as feasible, efficient, and low-cost method for preparation of boron doped carbon materials. [77], [78]

During hydrothermal carbonization process, sucrose molecules are hydrolyzed, due to autoionization of water, followed by auto condensation reaction of the molecules forming the spherical particles with size around 5 nm, and gradually growing in posterior stages until larger sizes, according to the treatment time. [77]-[79] By combining sucrose as carbon source and boric acid as dopant agent, via hydrothermal/ carbonization method, it is possible to produce boron-doped carbon materials. [80],[81] The type of bond between boron moieties into the boron-doped carbon can be visualized in **Figure 2.4**.
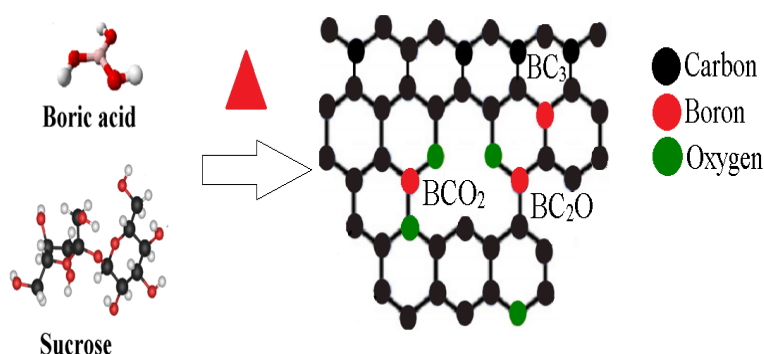
Figure 2.4 – Boric acid and sucrose for preparation of boron doped carbon. [77]

2.4   Physical and electrochemical characterizations

Standard techniques were used to characterize the catalyst materials and are shortly-described as follows.

2.4.1   Raman spectroscopy

Raman spectroscopy is an important tool to identify the degree of disorder in the carbon materials. In this technique a scattering monochromatic light (visible, infra-red, and near ultraviolet) is used. The monochromatic light constituted by photons interacts with the molecules of the sample and is scattered. By plotting the intensity of shifted light against frequency, the Raman spectrum of the sample is obtained. The appearance of a band at 1580 cm^{-1} (G-band) represents all kinds of sp^2 carbon systems that originate from the stretch of C-C bond in graphitic materials. The band located at 1350 cm^{-1} (D-band) represents the hybridized vibrational mode associated with graphene-like edges and disorder or defects. It is the relative intensity ratio between D and G bands that shows how much the material is disordered. [82]

2.4.2   Brunauer- Emmett-Teller method

Brunauer-Emmet-Teller (BET) technique is used to acquire information about the surface area and porous volume of the carbon materials. The method is based on the fact that gas molecules can be adsorbed on the walls of the carbon material. The amount of adsorbate adsorbed on a surface is described by the adsorption isotherm, which is a function of amount adsorbed versus the partial pressure at constant temperature. [83] The solid must be cooled in order to perform the test and the measurement of the external surface area and surface area due to channels and pores. The formation of a monolayer through physisorption requires a specific quantity of gases, such as nitrogen, and based on that, the surface area can be calculated.

Before the measurements, the samples must be degassed for removal of gases and vapors that may have been adsorbed onto the surface of the material.

The original weight of the sample before degassing and after degassing is recorded. The material is placed inside the test tube (**Figure 2.5-a**), placed in the thermal bath at 125℃ and degassed with inert(nitrogen) gas inside the thermal bath over 15 hours. The tubes are removed from the thermal bath and cooled at room temperature (**Figure 2.5-b**). For the actual test, nitrogen liquid is collected in a bucket (**Figure 2.5-c**), the tubes are connected into the machine connector (**Figure 2.5-d**), the bucket with liquid nitrogen will be used to cool the tubes containing the samples during the measurement operation (**Figure 2.5-e**).
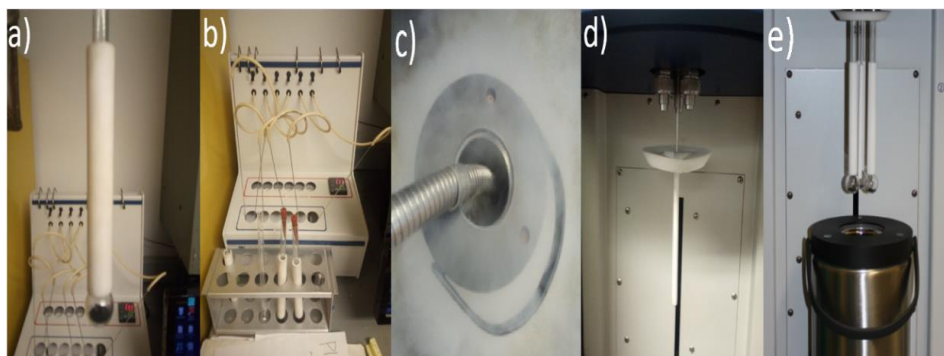
Figure 2.5-**a)** Sample is submitted to 24 hours nitrogen degassing at 124℃, **b)** Sample is cooled at room temperature, **c)** Nitrogen liquid collected in the bucket and placed under the of glass tubes containing the samples, **d)** Connection of tubes into nitrogen gas supply, and **e)** Set up ready for perform measurements.

2.4.3 X-ray photoelectron spectroscopy

X-Ray photoelectron spectroscopy is an essential technique for surface characterization for the investigation of chemical states and composition of components in the carbon materials. It provides the information of the bonding environment, distribution and percentage of heteroatom dopants incorporated into the carbon structure.

When a sample is irradiated by X-ray with specific energy, electrons at certain bound states are excited. The electrons, that are ejected due to the photon's incidence, scatter towards the surface, some inelastically, others with loss of energy. It is possible to associate the specific binding energy (the energy

that electrons have before they left the atom) to an element. The energy spectrum associates the number of electrons versus time (intensity) with each binding energy, therefore, it is possible to know which elements are present by identifying the binding energies and how much by the peak intensities. **[84]**

2.4.4 X-ray diffraction

X-ray diffraction is a technique used for characterization of crystallinity of the materials. For carbon materials the typical peak is identified at 24°, representing (002) and at 43° representing the (100) lattice of graphitic carbon. Sharper peaks indicate higher graphitization than broad peaks.

2.4.5 Cyclic voltammetry

The CV test is performed for electrochemical characterizations of samples in a standard three-electrode cell, connected to computer controlled electrochemical workstation. CV allows a rapid access to qualitative performance of the material by visualization of its onset potential, half-wave potential and current density at peak potential (**Figure 2.6**). CV is performed in stationary regime without rotation, while LSV is performed with rotation of the disk-ring electrode. The CV correlates the flow of electric charge, that is the number of electrons passed through the electrode per unit time, as a function of applied potential. During the CV measurement, the applied electrode potential is linearly ramped up and down as a function of time and the current is recorded as a function of the applied potential. In case of redox couple in electrolyte solution, the CV shows oxidation and reduction peaks due to the oxidation of redox species at the electrode surface and concomitant charge transfer across the interface.

The CV experiment can be carried out by using standard three electrodes cell set up. The working electrode is the electrode where the catalyst material is cast, second electrode is the reference electrode (should be stable and non-polarizable), which requires to set the applied potential of working electrode and third electrode is the counter electrode (should be chemically inert and preferentially carbon based for tests of metal-free catalysts). **[10]**, **[85]**

Figure 2.6 shows two CV curves. When the electrolyte is purged with nitrogen or argon, there is no ORR, and therefore there is no current density peak in the background curve (black curve). Upon purging the electrolyte with oxygen, the catalyst material will start the ORR, and as a result, a cathodic peak in the current density will appear (red curve).
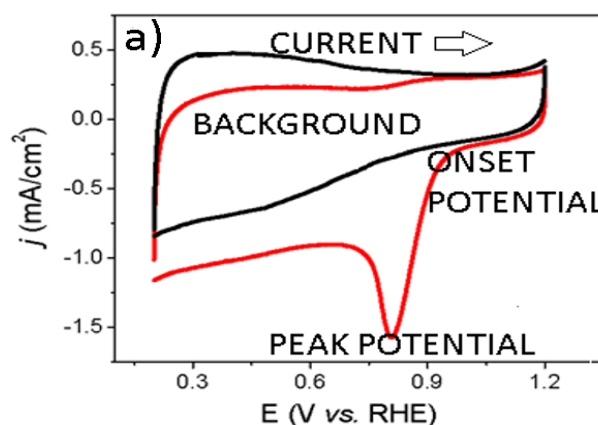
Figure 2.6- Cyclic voltammetry curves.

2.4.6 Linear Sweep Voltammetry

For the evaluation of CV and LSV tests, the catalyst material is typically dispersed in a solution containing Nafion binder and ethanol. The LSV characterization of the electrode is tested using standard three-electrode cell system in acid/base electrolyte purged with argon gas and oxygen. The LSV is performed with disk and ring-disk electrodes at various rotation speeds. When the electrolyte is purged with oxygen, a gradual increase of rotation speed of the electrode causes an increase of current density collected in the disk electrode.

When a ring-disk electrode is used, it is possible to collect the value of current in the disk, and use the values of current collected in the disk and ring to calculate the peroxide production and evaluate the four- and two-electron pathways for ORR. The limiting current density collected in the electrode is a function of the electrode rotating rate and the reactant concentration. The limited current density regime is reached when the current density curve is a straight horizontal curve(plateau), which means that the ORR is controlled mainly by

mass transport/diffusion. The better the diffusion and interchange of species, the higher values the current density will be reached. **[10]**, **[86]**, **[87]**

Figure 2.7-a, b, c show the three electrodes set up in the electrochemical station, ring-disk electrode, and disk-electrode, respectively. **Figure 2.8** shows the schematic illustration of the rotating disc electrode and the solution pattern near to the disk electrode surface and the shape of the curves referent to currents collected at the ring and at the disk in ring-disk electrode.
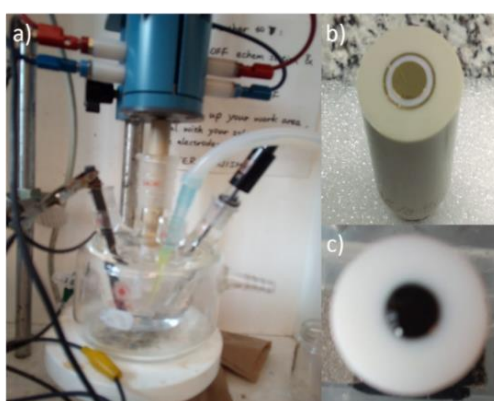
Figure 2.7- a) Photo of electrochemical station, gas inlet, calomel electrode (reference) and carbon electrodes (counter), **b)** Ring-disc electrode, and **c)** Disk-electrode after ink is casted.
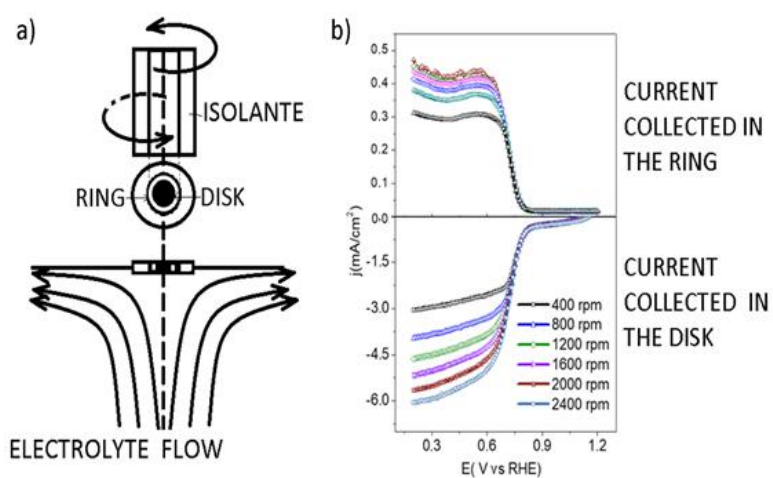
Figure 2.8-a) Schematic representation of flow onto the rotating ring-disk electrode surface, and **b)** Current collected at the disk(lower) and ring(upper).

3 MATERIALS AND METHODS

3.1 Materials and methods: PANI and PEDOT derived carbons

The synthesis of the carbon catalysts is presented in this chapter. Polythiophene, PEDOT and PANI are the polymer precursors that were polymerized and carbonized for the preparation of single sulfur-doped, single nitrogen-doped and nitrogen-sulfur co-doped carbon materials.

Herein, we present the different batches of samples prepared from the polymer precursors. We also distinguish the samples prepared with silicon nitride or silicon dioxide nanospheres as core particles. We used silicon nitride (Si_3N_4, 20 nm) and silicon dioxide (SiO_2, 200 nm) as core particles during polymerization followed by carbonization.

3.1.1 Synthesis of nitrogen doped carbon coated silicon nitride nanospheres (Si_3N_4, 20 nm)

The typical synthetic method is described as follows, 0.2 g of Si_3N_4 nanospheres were added to 40 ml of water and sonicated for 120 min (**Figure 3.1-a**). In a separate beaker, an anilinium solution was prepared with 10 ml of 1M HCl and 200 µl aniline monomers. **[88]** After the anilinium solution was prepared, it was stirred for 1 h, then Si_3N_4 dispersion was added with intense stirring for 2 h at 0℃ (**Figure 3.1-b**). Then, the Si_3N_4 - anilinium solution was injected vigorously into 50 ml of chloroform in another beaker, placed in a dry ice bath inside a frigorific room at -10℃. Afterwards, a 50 ml of oxidizer solution was prepared (monomer-oxidizer ratio of 1:1) and cooled at 0 ℃ for 1 hour and then slowly added into the Si_3N_4 -anilinium solution to 45 min. The total polymerization reaction was carried out during 14 h, resulting in the dark green colored PANI coated Si_3N_4 nanospheres (**Figure 3.1-c**). The schematic illustration of the synthesis is represented in **Figure 3.2**. After 5 cycles of centrifugation (**Figure 3.1-d,e**), the samples were freeze dried, and then, carbonized at 900℃ and 1000℃ by a gradual step process, holding 1 h at 400℃, and 2 h at 900℃ or 1000℃ under argon atmosphere, as represented by sketch drawing in (**Figure 3.1-g**) The names of as-prepared samples (NC-14-900-20 and NC-14-1000-20)

were expressed according to the polymerization time (14 h), carbonization temperature (900℃ or 1000℃) and size of the core (20 nm).
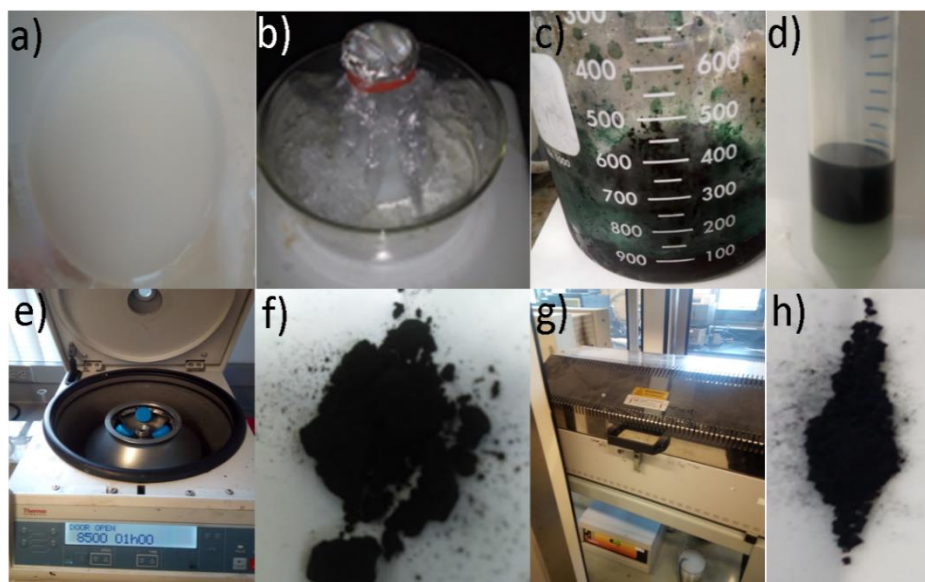
Figure 3.1 - Synthesis steps of the PANI coated Si₃N₄ nanospheres via self-stabilized polymerization: **a,b)** Si₃N₄ nanosphere were dispersed in water followed by addition of anilinium cation solution at 0℃, **c)** After mixing the two solutions and chloroform, the oxidant was added, **d)** Polymer solution formed separated phase from chloroform, **e)** The polymer was separated from the chloroform via centrifugation, **f)** Dark-green polymer after freeze-dried, **g)** Carbonization of polymer in furnace, **h)** Final product of doped carbon material.
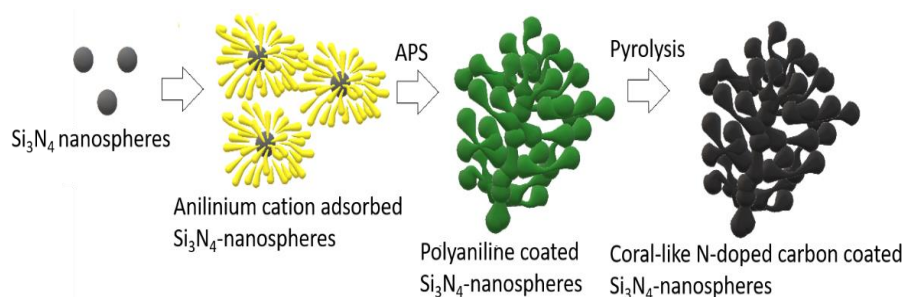
Figure 3.2 - Schematic representation of synthesis of the PANI coated Si₃N₄ nanospheres resulting in coral like nitrogen doped carbon coated Si₃N₄.
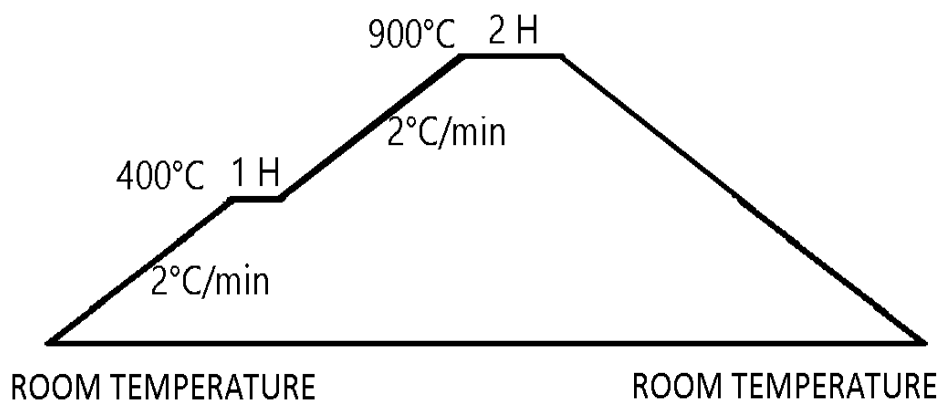
Figure 3.3 - a) Carbonization process with two-stages for preparation of doped carbon materials from polymer precursors.

3.1.2 Synthesis of sulfur and nitrogen co-doped carbon coated silicon nitride nanospheres (Si3N4, 20 nm)

For the preparation of the sulfur nitrogen co-doped carbon catalyst (SNC), the nitrogen doped carbon coated - Si_3N_4 nanospheres (as prepared sample NC-14-900-20) was used as core.

Firstly, 0.1 g of nitrogen doped carbon (sample NC-14-900-20), and 3.5 ml of emulsifier 4-dodecylbenzene sulfonic acid were added to 200 ml of water and stirred for 2 h. Next, the 400 μl of EDOT monomers were added with continuous stirring. After 24 h, the oxidizer ammonium persulfate was added to polymerize the monomers of EDOT at room temperature for 24h. The process is represented by digital photographs in **Figure 3.4**. After complete polymerization, the material was washed using distilled water, freeze dried and carbonized at 900°C for 2 h (ramp rate 2°C/min) in argon atmosphere to obtain final dual doped carbon materials of SNC (black powder) (**Figure 3.4 - d)**.

Figure 3.4 - Synthesis steps for preparation of sulfur-nitrogen co-doped carbon, **a)** Nitrogen-doped carbon is dispersed in solution with emulsifier, followed by addition of oxidizer, **b)** Polymerization of PEDOT onto nitrogen doped carbon coated Si_4N_3, **c)** Carbonization of material in furnace, and **d)** Nitrogen-sulfur doped carbon.

3.1.3 Synthesis of sulfur doped carbon coated silicon dioxide spheres (SiO2, 200 nm)

For the preparation of sulfur doped carbon coated SiO_2 particles, we polymerized EDOT in an emulsion containing SiO_2 particles with 200nm of diameter. **Figure 3.5** shows the steps for the preparation of PEDOT coated SiO_2 particles. **[71]**

In brief, 4 ml of emulsifier DBSA and 400 µl of EDOT monomers were dispersed in 200 ml of water (**Figure 3.5-a**). After gradual and slow addition of oxidizer solution (containing 3.5 g of ammonium persulfate), the polymerization was carried out for 20 h. **Figure 3.5-b, c** show a dark blue paste-like material, which was collected via 5 cycles of centrifugation and washed with distilled water (**Figure 3.5-e**). After the freeze-drying step, the resulting powder (PEDOT coated SiO_2 particles) presented a dark blue color. This material was thermally treated at 400°C for 1 h (ramp rate of 2°C /min), followed by a carbonization step of 2 h, at one of the selected temperatures 800°C, 900°C or 1000°C (ramp rate of 2°C/min). The whole carbonization process was performed inside a quartz tube in argon atmosphere. The resulting material from the carbonization of PEDOT-coated SiO_2 was turned into a black powder material (**Figure 3.5-f**). The obtained

materials were named SC-800, SC-900, and SC-1000, corresponding to the carbonization temperatures of 800℃,900℃ and 1000℃.

Sample SC-900 was further treated with hydrofluoric acid for removal of SiO_2 core. Briefly 15 ml of deionized water, 5 ml of hydrofluoric acid (38-40% Alfa-Aesar) and 1ml of nitric acid were mixed with 0.1 g of sample SC-900, and stirred for two days at 50℃, then washed thoroughly and dried in oven overnight. Resulting sample was named SC-HF.
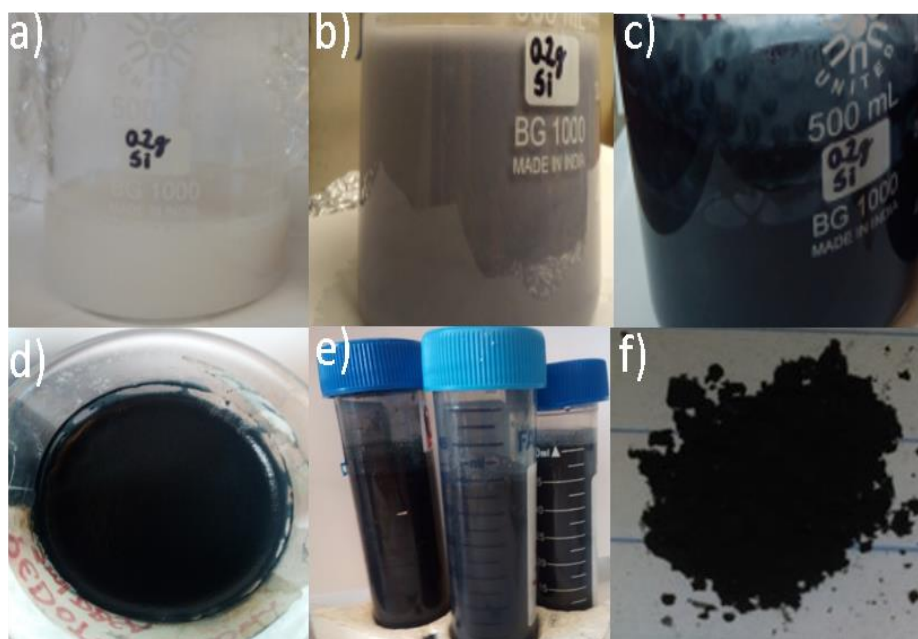
Figure 3.5 - Synthesis steps for the preparation of the sulfur-doped carbon, **a**) Silica nanospheres dispersed into the emulsion of DBSA, **b)** Change in the color of the emulsion as the polymerization progresses, **c), & d)** Polymerization completed showing the dark blue PEDOT, **e)** Centrifugation and collection of polymers coated silica, **f)** After carbonization PEDOT coated silica is converted into sulfur-doped carbon coated silica.

3.1.4 Synthesis of nitrogen and sulfur co-doped carbon coated silicon dioxide nanospheres (SiO2, 200 nm)

Sample SC-900 was used for preparation of nitrogen and sulfur co-doped carbon materials. Firstly, SC-900 was treated in an acidic solution (0.1M HNO_3) for 2 h at 50℃ and washed thoroughly with distilled water and ethanol and dried

in the oven overnight. After this pre-treatment, SC-900 powder was used as core for polymerization of aniline. In brief, 0.1 g of SC-900 was dispersed in 50 ml of water, sonicated 15 min, and left stirring in a beaker (**Figure 3.6-a**). In another beaker, 200 µl aniline monomers were added to10 ml of 1M HCl at 0°C and kept stirring for 1 h in a frigorific room (-10 °C). Thereafter, the anilinium solution was added into the beaker containing the SC-900 and placed in bath at 0℃ for 2 h with vigorous stirring (**Figure 3.6-b**). Later, chloroform (80 ml) was added into the beaker and kept at 0°C.

Then the oxidizer (3.4 g of ammonium persulfate in 10 ml of 1 M HCl) was added dropwise and left for polymerization for 24 h. After the complete polymerization, a dark green color material (**Figure 3.6-c, d**) was obtained. The dark green product was washed, collected via centrifugation, and freeze dried for 3 days. The dry powder was thermally treated at 400℃ for 1 h, followed by carbonization for 2 h at 900℃ (ramp rate of 2 ℃/min). The resulting sample was named as NSC-900 with respected carbonization temperature.

Further, the sample NSC-900 was treated with hydrofluoric acid for removal of the SiO_2 core particles. For preparation of etched sample, 0.2 g of sample NSC-900, 5 ml of hydrofluoric acid (38-40% Alfa-Aesar), 15 ml of distilled water and 1 ml nitric acid were stirred during 72 h at 50℃ inside plastic tube. Following, the solution was diluted in 500 ml of distilled water, and repeatedly washed with water, centrifuged, and freeze-dried for 3 days. **Figure 3.6 a-e)** shows the photographs of the sample SC-900 (sulfur doped carbon), dispersion, polymerization, dark-green colored composite and after carbonization: black powder. **Figure 3.7** shows representation of the synthesis of NSC-900 and NSC-HF.
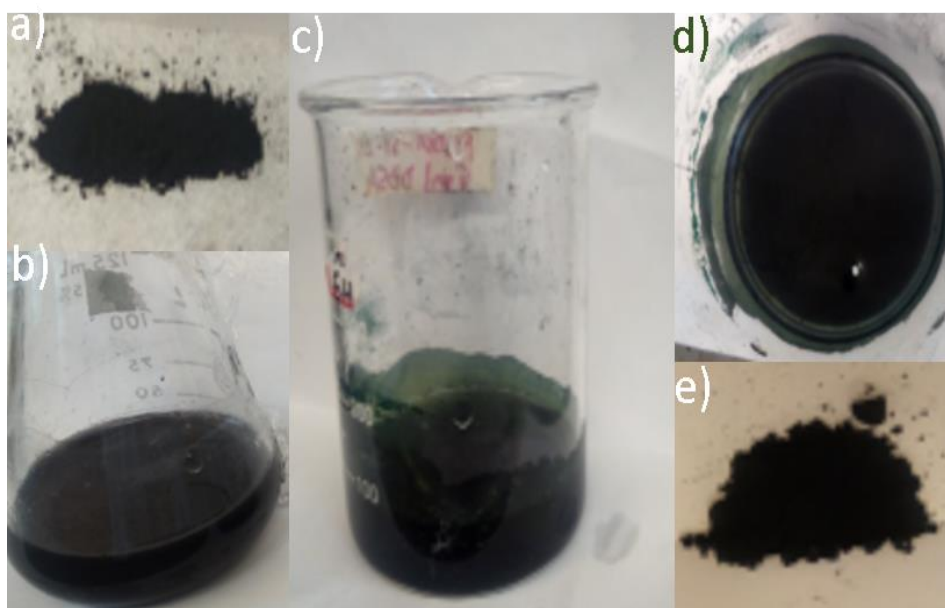
Figure 3.6- Synthesis steps for the preparation of the sample nitrogen-sulfur co-doped carbon. **a**) Sulfur-doped carbon coated silica powder. **b)** Sulfur doped carbon is dispersed in water, **c, d)** PANI coated over the sulfur-doped carbon (after polymerization), **e)** Nitrogen-sulfur co-doped carbon after the pyrolysis.
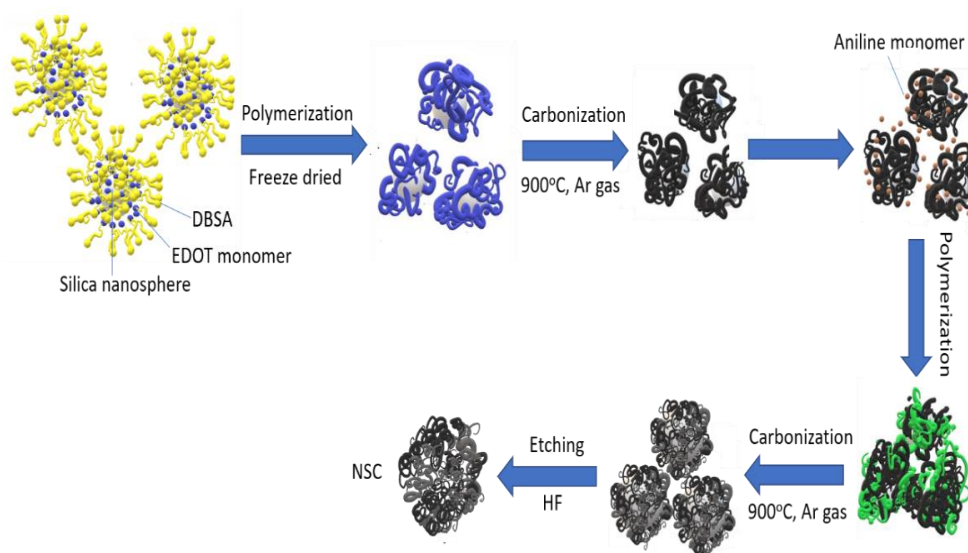
Figure 3.7- Synthesis process of sample NSC-900 and NSC-HF. **[88]**, **[89]**

3.1.5 Synthesis of nitrogen doped carbon coated silicon dioxide nanospheres (SiO2, 200 nm)

PANI was grown onto the surface of SiO_2 nanospheres (200 nm) using the same method as described in section 3.1.1. **Figure 3.8-a** shows the dispersion of SiO_2 nanospheres in water and **Figure 3.8-b**, **c** show the dark green colored product of PANI coated SiO_2 particles after polymerization. The obtained material was washed with distilled water and centrifuged for several times (**Figure 3.8-d**). After carbonization, the material turned into a black colored powder. This product of carbonization step, is nitrogen doped carbon coated SiO_2 particles, as shown in **Figure 3.8-e**. This sample was named NC-900. The sample NC-900 was treated by hydrofluoric acid bath, (10ml water, 5 ml hydrofluoric acid (38-40% Alfa-Aesar), 1 ml nitric acid) for 2 days at 50°C to remove silica core particles.
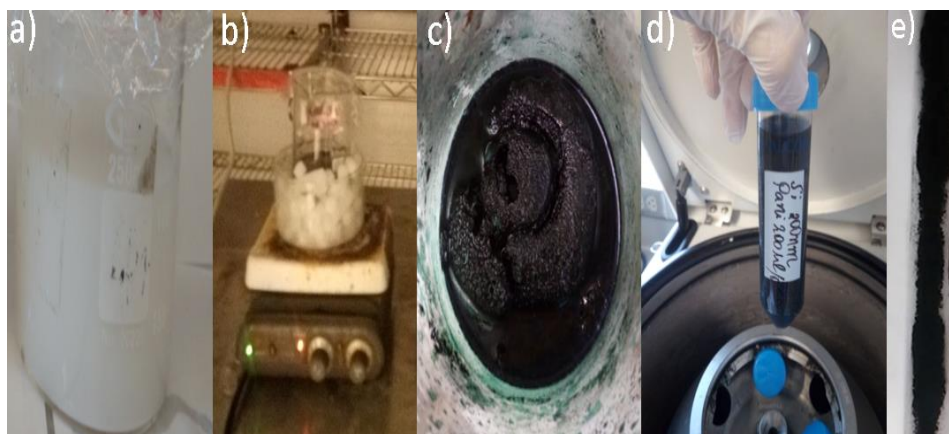
Figure 3.8 - Synthesis steps for preparation of the sample constituted by nitrogen-doped carbon using silica of 200 nm, **a)** Silica dispersed in water in one beaker, and anilinium cationic solution in a separate beaker, **b)** Silica and aniline cations solution were poured together followed by addition of oxidizer, **c)** Polymerization was finished, resulting in dark green PANI, **d)** Centrifugation and collection of the product, and **e)** Nitrogen-doped carbon after carbonization.

3.1.6 Synthesis of sulfur and nitrogen co-doped carbon coated silicon dioxide nanospheres (SiO2, 200 nm)

Sample NC-900 was used as core for the polymerization of EDOT monomers, forming a polymeric shell/coating onto it. With subsequent carbonization, the composite was converted into sulfur and nitrogen co-doped carbon coated SiO_2 nanospheres.

In brief, 0.2 g of NC-900 was dispersed in water with sonication. Next, a mixture of 3 ml of DBSA and 500 μl of EDOT monomers in 400 ml of water was added and left stirring for 2 h. Afterward, an oxidizing solution of ammonium persulfate was added with constant stirring and left for polymerization for over 24 h. Gradually, the emulsion was turned into a dark blue colored material. The resulting material was washed thoroughly and centrifuged with 5 cycles and freeze-dried for 3 days. The material was collected and thermally treated at 400℃ for 1h (ramp rate of 2℃/min), followed by carbonization for 2 h at 800℃ or 900℃ (ramp rate of 2℃/min), under an argon atmosphere. After carbonization, the samples cooled down naturally at room temperature. The final products were denoted as SNC-SiO2-900 and SNC-SiO2-800, according to the respective carbonization temperatures. Sample SNC-HF was prepared via hydrofluoric acid bath treatment of sample SNC-SiO2-900, in the same fashion as mentioned in the previous section.

3.2 Materials and methods: PANI and PTH derived carbon materials

Herein, we report samples prepared with PTH and PANI. We started with preparation of PTH via oxidative polymerization. The polymerization of thiophene monomers was carefully carried out with the use of 'metal free' oxidizer, ammonium persulfate. Traditionally, iron chloride ($FeCl_3$) is used for polymerization of thiophene, but we abstain from its use to prevent any metal contaminations.

3.2.1 Synthesis of sulfur doped carbon coated silicon dioxide nanospheres (SiO₂, 200 nm)

The synthetic protocol consists in chemical oxidative polymerization using oxidant ammonium persulfate for polymerization of thiophene monomers. The solvent system consisted of 300 ml of methanol and 50 ml of mercaptoethanol. Monomers (2 ml) of thiophene, and 1 g of silica nanoparticles were added in the system sonicated during 20 minutes, and stirred vigorously for 2 h. Oxidant ammonium persulfate (6 g) in 200 ml of water was added into the above system containing the silica and monomers with vigorous stirring at 60℃. After 3 days of polymerization, a brown solid product was obtained. The product was collected and washed with distilled water via 5 cycles of centrifugation. After freeze drying for 3 days, the dark brown powder was obtained then carbonized under an argon atmosphere at 900℃ for 2.5 h. The resulting material was named SC-SiO₂-PTH-900. **Figure 4.1-a,b,c,d,e** show the general steps of the synthesis process.
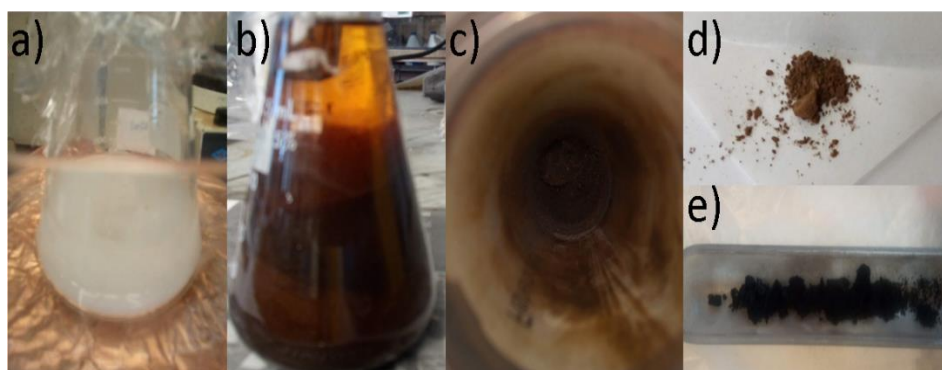
Figure 3.9- Photographs of the preparation of sulfur doped carbon coated SiO₂ particles. **a)** dispersion of silica in water, **b)** After polymerization of polythiophene, **c, d)** after washed and freeze dried, **e)** after carbonization.

3.2.2 Synthesis of nitrogen and sulfur co-doped carbon coated silicon dioxide nanospheres (SiO$_2$, 200 nm)

For the preparation of nitrogen and sulfur co-doped carbon material, firstly, 0.2 g of SC-SiO$_2$-PTH-900 was mixed into a beaker containing 100 ml water and sonicated for a few minutes and then kept stirring for 1 h. An anilinium solution was prepared using 200μl of monomers and 10 ml of 0.1 M HCl in another beaker. Both beakers were placed inside a frigorific room at 0℃ bath for 1h under vigorous stirring. The solutions of both beakers were mixed under vigorous stirring for another 2 h. Then, an oxidizing solution of water and ammonium persulfate was poured into the above mixture to oxidative polymerization of aniline monomers and left for 24 h to polymerize. After the polymerization, the material was washed thoroughly and collected via filtration.

The dark green colored material was carbonized at 900℃ and 1000℃, in an argon atmosphere for 2 h. The samples were named as NSC-PANI-PTH-SiO$_2$-900 and NSC-PANI-PTH-SiO$_2$-1000.

The etching process with hydrofluoric acid was done for sample NSC-PANI-PTH-SiO$_2$-900 using diluted hydrofluoric acid solution for 3 days at 50℃, to remove the SiO$_2$ nanospheres. The method of etching is the same as previously described. The etched sample was named NSC(PANI-PTH-HF).

3.3 Materials and methods: boric acid, sucrose and polyaniline derived carbon materials

In this phase of work, we synthesized boron doped carbon spheres via hydrothermal method using simply boric acid, sucrose and water. Then, the boron doped carbon spheres were used again during the polymerization of aniline monomers. The product of the polymerization was carbonized and resulted in boron and nitrogen co-doped carbon materials.

3.3.1 Synthesis of boron doped carbon

The synthetic protocol consists of a simple hydrothermal process (**Figure 3.4.1**). In brief, 40 ml of water, 0.01mol of sucrose, and 0.065 mol of boric acid were stirred for 25 min, and transferred to Teflon-lined stainless-steel autoclave, then heat treated at 180℃ for 20 h. The brown solid product obtained was washed several times with distilled water and collected via centrifugation, then freeze dried for three days. Thereafter, the collected material was carbonized in an argon atmosphere at 900℃ and 1000℃ for 2 h (ramp rate of 2℃/min). The resulting samples were named as BC-900 and BC-1000.

Figure 3.10- Schematic representation of hydrothermal synthesis of boron-doped carbon samples. **a)** Sucrose and Boric acid were dispersed in water, followed by hydrothermal synthesis in autoclave and, **b, c)** the product collected, washed, dried, and **d)** carbonized, resulting in boron-doped carbon.

3.3.2 Synthesis of boron and nitrogen co-doped carbon

For the synthesis of boron and nitrogen co-doped carbon, the boron doped carbon as synthesized above was intended to work as core during PANI preparation, followed by carbonization.

Polymerization of aniline monomers was performed using 0.1 g of sample BC-900 dispersed in 40 ml of water. An acidic solution with100µl of aniline and 60µl of HCl, was prepared and added to the beaker with constant stirring at cold bath (0℃). Oxidizing solution (ammonium persulfate) was added dropwise and left for polymerization up to 24 h. Then the product was collected and washed

with distilled water and methanol via filtration and dried in an oven overnight at 60℃.

The dark green product in powder form was submitted to the thermal treatment; it was carbonized for 2 h at 900℃ for preparation of NBC-900; and it was carbonized at 1000℃ for preparation of NBC-1000. The increase in temperature followed a very slow ramp rate at 2℃/min. The carbonization process was performed in argon gas flow. After the carbonization finished, the oven was left to cool down at room temperature. The nitrogen and boron doped carbon materials were named NBC-900 and NBC-1000. The steps of the synthesis process are shown in the **Figure 3.11 - a, b, c, d, e**.

Figure 3.11- Preparation of the sample constituted by nitrogen-boron co-doped carbon material. **a)** Dispersion of boron doped carbon BC-900 into water, **b)** boron doped carbon, aniline monomers and acid dispersed in beaker and placed in cold bath, **c)** PANI coated onto boron doped carbon, **d)** Dark green colored PANI coated boron doped carbon, and **e)** Boron and nitrogen co doped carbon after carbonization.

4   RESULTS AND DISCUSSION

The characterizations of the materials were performed by X-Ray Diffraction, Raman spectroscopy, Brunauer-Emmett-Teller (BET) surface area analysis and pore size distribution, X-ray photoelectron spectroscopy, transmission electron microscopy and scanning electron microscopy were used for characterization of morphological features. The electrochemical characterizations were performed through the standard CV and LSV measurements in alkaline medium.

4.1 Physical and electrochemical characterizations of nitrogen doped carbon coated silicon nitride nanospheres (Si_3N_4)

TEM images of the sample NC-14-900-20 (**Figure 4.1-a, b** and **Figure 4.2-a, b**) show a coral-like structure, revealing Si_3N_4 nanoparticles encapsulated by the carbon shell and joined by carbon branches as coral-like structures. TEM images of sample NC-14-1000-20 (**Figure 4.3-a, b** and **Figure 4.4-a,b**) also show similar morphological structure to that of the sample NC-14-900-20, corroborating that the Si_3N_4 nanospheres were successfully wrapped by the carbon layers.
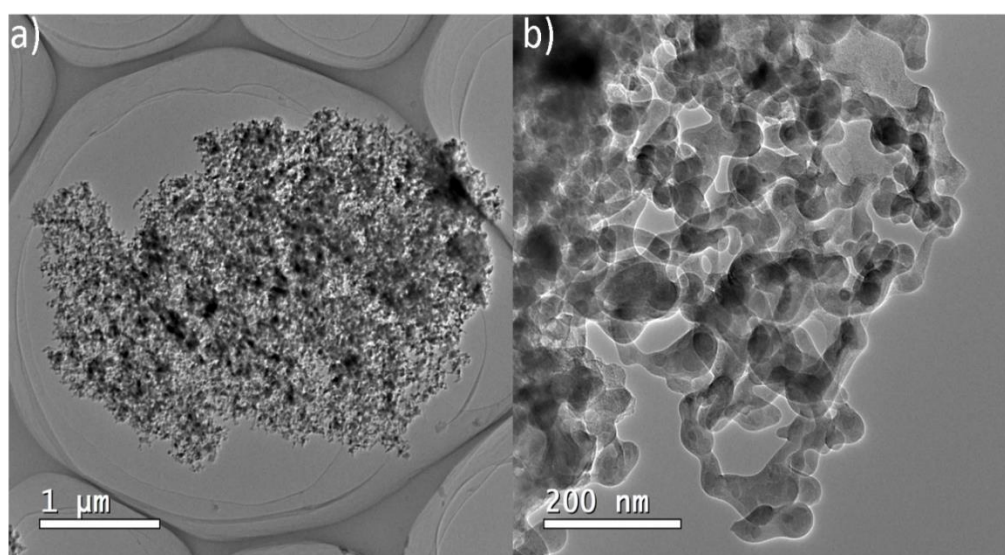
Figure 4.1-a) TEM image of sample NC-14-900-20 shows the Si_3N_4 nanospheres coated by nitrogen doped carbon layer. **b)** High resolution TEM image of NC-14-900-20 at 200 nm revealing a coral-like structure.
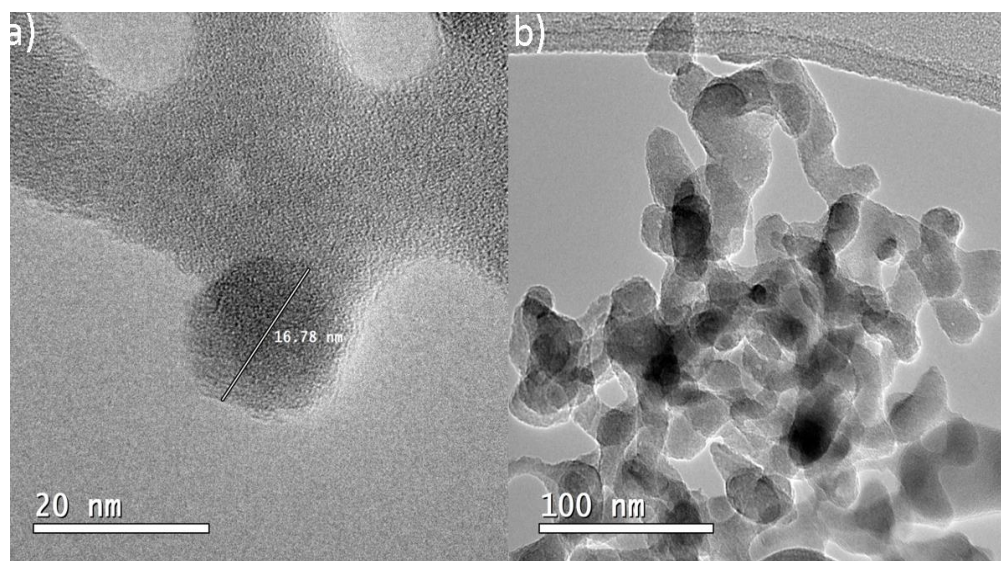
Figure 4.2-a) High resolution TEM image of sample NC-14-900-20 shows Si_3N_4 nanosphere with the diameter around 16.78 nm wrapped by nitrogen doped carbon material. **b)** TEM image of sample NC-14-900-20 shows a coral-like structure.
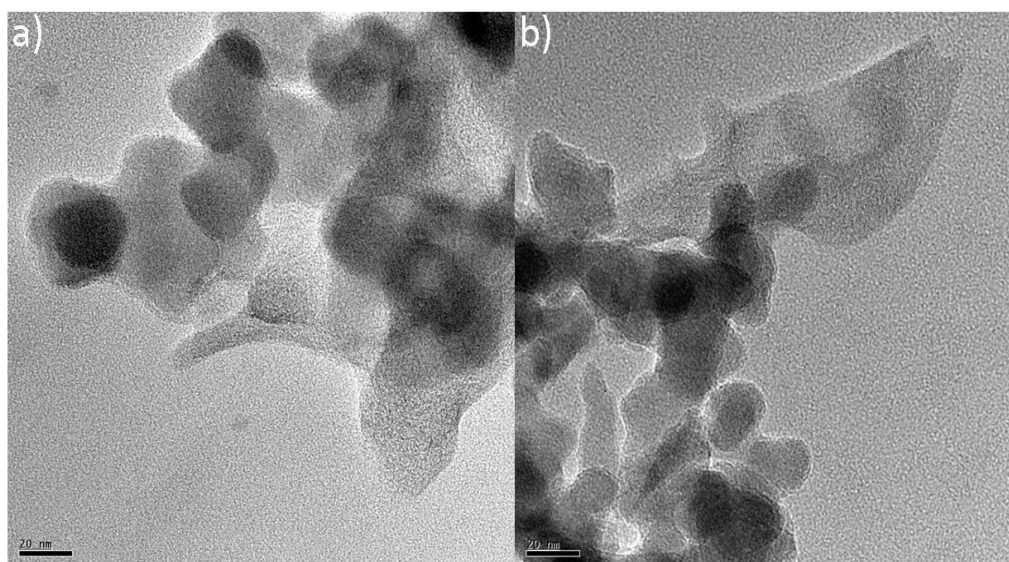
Figure 4.3-a, b) TEM images of the sample NC-14-1000-20, also showing the fine coating of nitrogen doped-carbon coated onto the Si_3N_4 nanospheres.
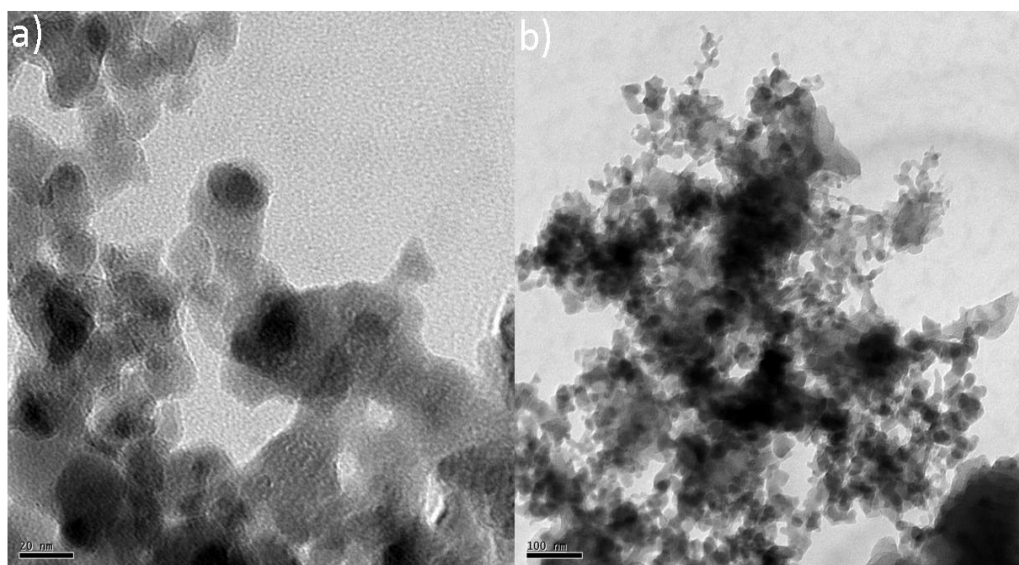
Figure 4.4-a, b) TEM images of the sample NC-14-1000-20 showing the fine coating of nitrogen doped-carbon coated onto the silica nanoparticles and a coral-like structure at different magnifications.

The physical characterizations of the materials were also evaluated by X-ray photoelectron spectroscopy, X-ray diffraction, Raman spectroscopy, and nitrogen adsorption-desorption isotherms (BET surface area).

XPS survey analysis (**Figure 4.5-a**) for the sample NC-14-1000-20 presents 33.6% of oxygen, 27% of carbon, 22.6% of silicon, and 16.8% of nitrogen elements. The high content of nitrogen (16.8%) was due to the presence of Si_3N_4 nanosphere. By deconvolution of the peaks in the XPS spectra of N 1s, the species of nitrogen were identified at its respective binding energies, as 79.5% pyridinic-nitrogen (397.5 eV) and 20.5% pyrrolic-nitrogen (398.6 eV), as shown in **Figure 4.5-b**. The C 1s XPS spectra (**Figure 4.5-c**) show the peaks for C-C/ C-N (53%), and C=C- (47%). The O1s XPS spectra (**Figure 4.5-d**) can be deconvoluted into two characteristic peaks, one at 532.6 eV corresponding to the oxygen bound to carbon and another one at 534 eV assigned to the surface adsorbed oxygen.
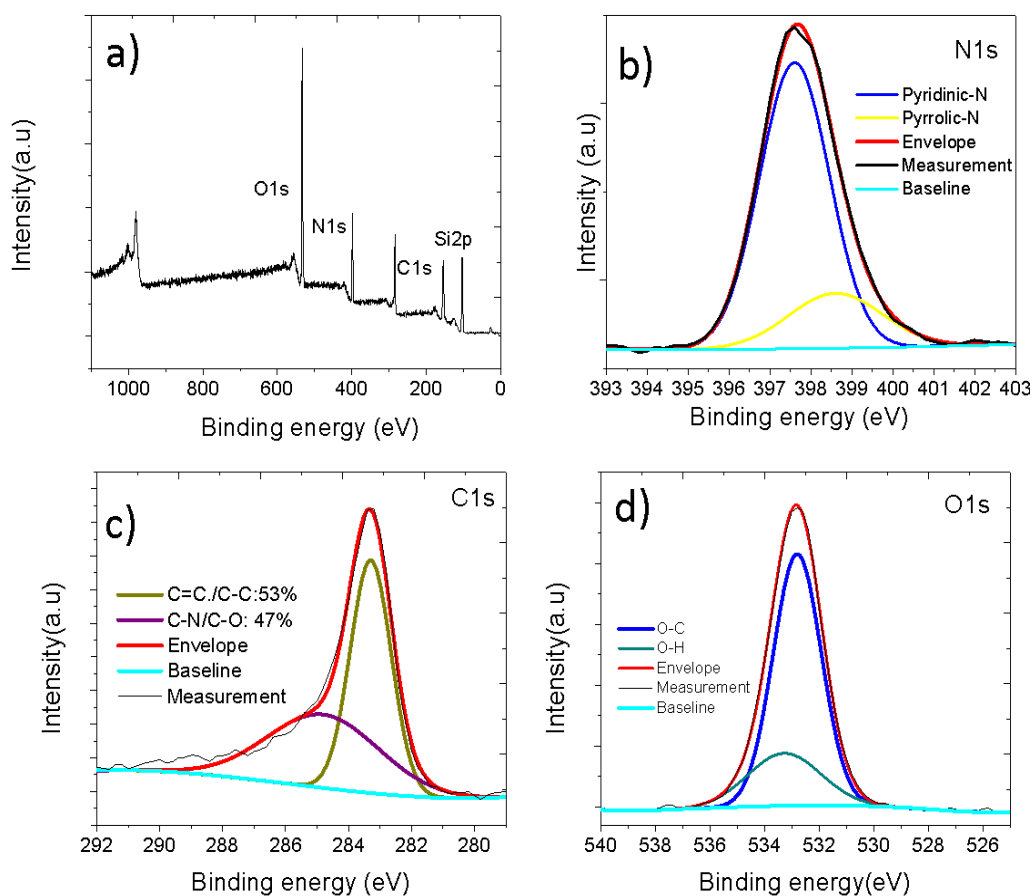
Figure 4.5-a) XPS survey of sample NC-14-1000-20, **b)** XPS spectra of N 1s, **c)** XPS spectra of C 1s, and **d)** XPS spectra of O 1s.

XPS survey (**Figure 4.6-a**) for the sample NC-14-900-20 shows the percentage of oxygen (33.4%), carbon (26.9%), silicon (21.3%), and nitrogen (18.4%). Deconvolution of N1s XPS spectra (**Figure 4.6-b**) of sample NC-14-900-20 showed 70.4% pyridinic-N (398 eV), 29% pyrrolic-N (399 eV) and 0.6% quaternary-N (400 eV). The XPS spectra of C 1s (**Figure 4.6-c**) was assigned to C=O (37%), and C=C (63%). The O1s XPS spectra (**Figure 4.6-d**) showed two peaks corresponding to oxygen bound with carbon (532.8 eV) and surface adsorbed oxygen (533.8 eV).

The variation in percentage of nitrogen content in samples NC-14-1000-20 (16.8%) and NC-14-900-20 (18.4%) can be explained due to the difference in carbonization temperatures. Higher temperature (1000 °C) causes further loss of nitrogen species.
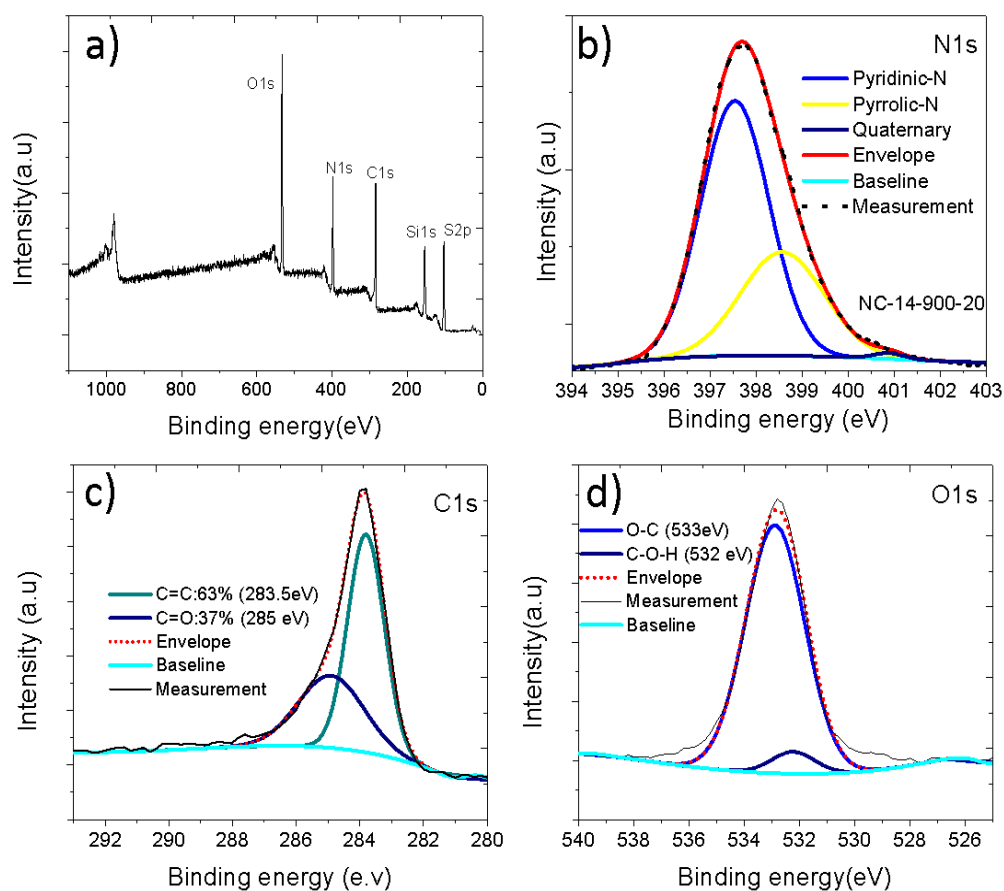
Figure 4.6-a) XPS survey spectra of NC-14-900-20. **b)** XPS spectra of N 1s, **c)** XPS spectra of O 1s, and **d)** XPS spectra of C1s.

The Raman spectra of NC-14-900-20 and NC-14-1000-20 (**Figure 4.7-a**) show D- and G-bands at 1353 and 1592 cm^{-1}. The D band is due to out of plane vibrations and signals the presence of structural defects, and the G band is the result of in-plane vibrations of Sp2 carbon. **[90]** The ratio of peak intensities (I_D/I_G) were calculated 0.89 (NC-14-900-20) and 0.88 (NC-14-1000-20) suggesting that there is a considerable graphitized carbon in both samples. In **Figure 4.7-b**, the XRD patterns of NC-14-900-20 and NC-14-1000-20 represent the most relevant peaks at 2θ = 24° and 43°, indicating that the both samples are graphitized carbon, which can greatly improve the electronic conductivity of the materials. **[90]**
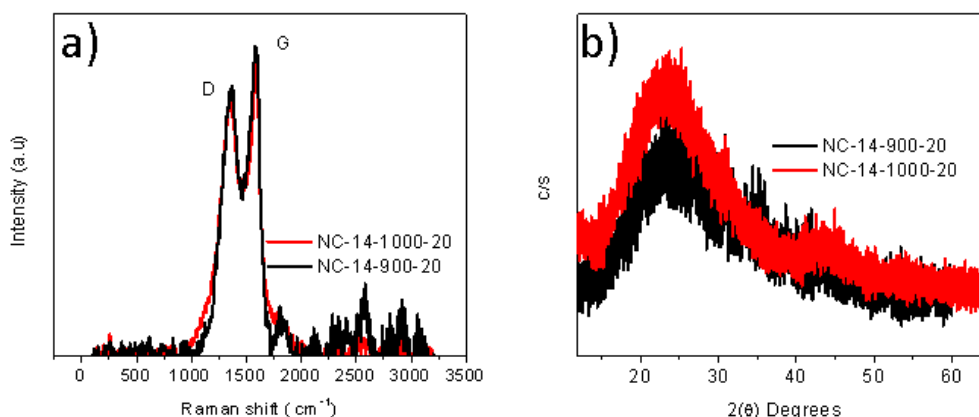
Figure 4.7-a) Raman spectra of NC-14-900 and NC-14-1000-20, and **b)** XRD patterns of NC-14-900-20 and NC-14-1000-20.

BET surface area and pore size distribution were investigated by a nitrogen adsorption-desorption analysis. As shown in **Figure 4.8-a**, both samples are classified as mesoporous materials and show type IV isotherm. **[91]**

BET specific surface areas were measured to 403 and 420 m^2 g^{-1} for NC-14-900-20 and NC-14-1000-20, respectively. It can be suggested that increasing temperature from 900 to 1000°C, slightly increases the specific surface area and can introduce more active sites and defects for enhancing catalytic performance. But on the other hand, higher temperatures of carbonization inevitably cause loss of the active sites, resulting in less catalytic activity. Dollimore Heal pore distribution plot derived from the nitrogen desorption isotherm (**Figure 4.8-b**), further pointed towards the majority of mesopores with diameter ranging from 10 to 50 nm. Such characteristics of the carbon and its coral-like morphology facilitate rapid ion/mass transport and expose more active sites in the material.
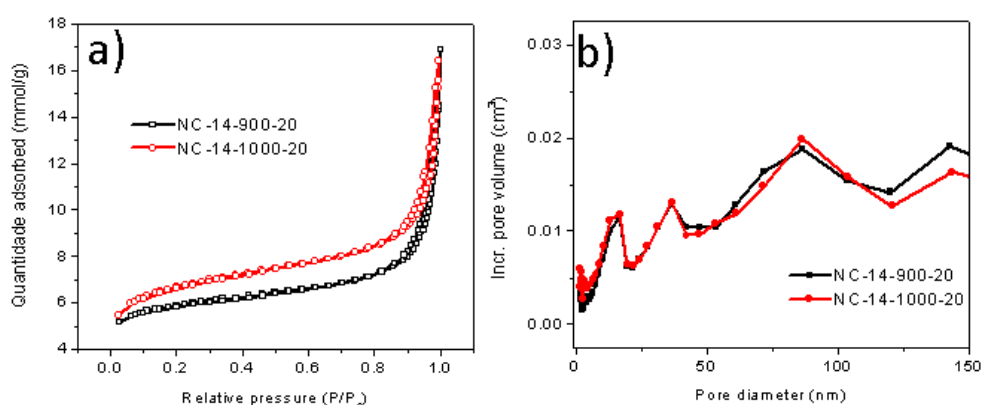
Figure 4.8-a) BET measurement of NC-14-900-20 and NC-14-1000-20, and **b)** Pore size distribution of NC-14-900-20 and NC-14-1000-20.

CV curve of the sample NC-14-900-20 (**Figure 4.9-a**) shows the peak potential of the curve at 0.82 V, half -wave potential at 0.85 V vs RHE, and onset potential of 0.9 V vs RHE (blue curve). The peak appears only when electrolyte is purged with oxygen; in contrast the peak was absent when the solution was purged with argon or nitrogen (black curve). This indicates that the material is electrocatalytic active for oxygen reduction. **Figure 4.9-b** (and **Figure 7.1-a** in Appendix) show the LSV curves at different rotational speeds, as can be seen, the current proportionally increases with increasing rotation speed. The current density curves are almost horizontal lines, suggesting a diffusion-controlled oxygen reduction and first order kinetic for ORR in alkaline solution (0.1M KOH). **[23], [92]-[94]**
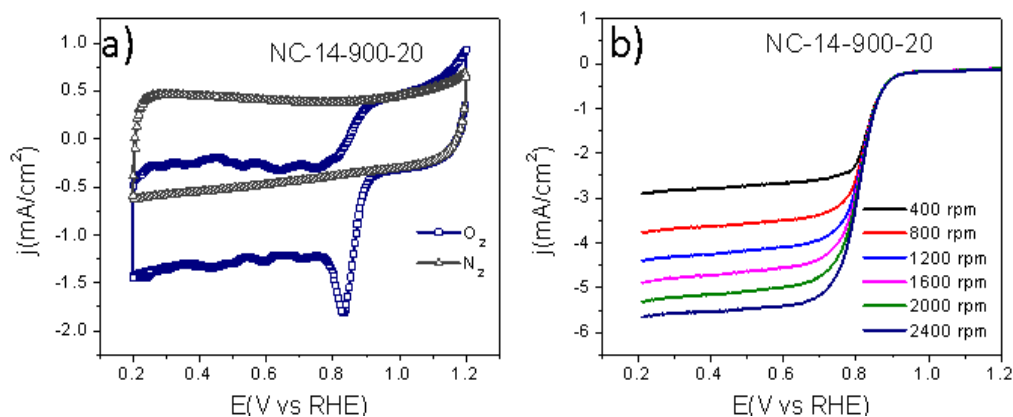
Figure 4.9- a) CV curves of NC-14-900-20 and **b)** LSV curves of NC-14-900-20.

Figure 4.10-a presents the linear Koutecky-Levich plot (j^{-1} vs. $\omega^{-1/2}$). The values of current density collected at the disk electrode at different rotating speeds were used to calculate the values of electron transfer number at different potential. The average values of electron transfer number of NC-14-900-20 was calculated for each potential using the electron transfer number values from the four tests, 3.6 (0.2V vs RHE),3.4 (0.3V vs RHE), 3.45 (0.4V vs RHE), 3.44 (0.5V vs RHE). The specific electron transfer number values to each potential were calculated according the tests as shown in **Figure 4.10-b**. The supplementary linear sweep voltammetry curves used to calculation of electron transfer numbers are in **Figure 7.1 a**, (Appendix). These values of electron transfer number reveal the high ORR selectivity with electron transfer path near to the four-electron transfer path. The superior ORR activity was further observed from the low amount of peroxide species generated on rotating ring disk electrode at 1600 rpm **(Figure 4.11-a)**. The electron transfer number values calculated from the currents collected at the disk and ring were 3.41(0.2 V vs RHE),3.42 (0.3 V vs RHE), 3.40 (0.4 V vs RHE), 3.40 (0.5 V vs RHE) and 3.39 (0.6 V vs RHE) and the average electron transfer number was near to 3.4 **(Figure 4.10-b)** which was close to the electron transfer number calculated from the Koutecky-Levich plot. As shown in **Figure 4.11- c**, the ring current is much lower than the disk current, suggesting low production of peroxide species, the yield of peroxide for NC-14-900-20 was measured lower than 20% to all potentials, suggesting high selectivity of the catalyst for ORR.
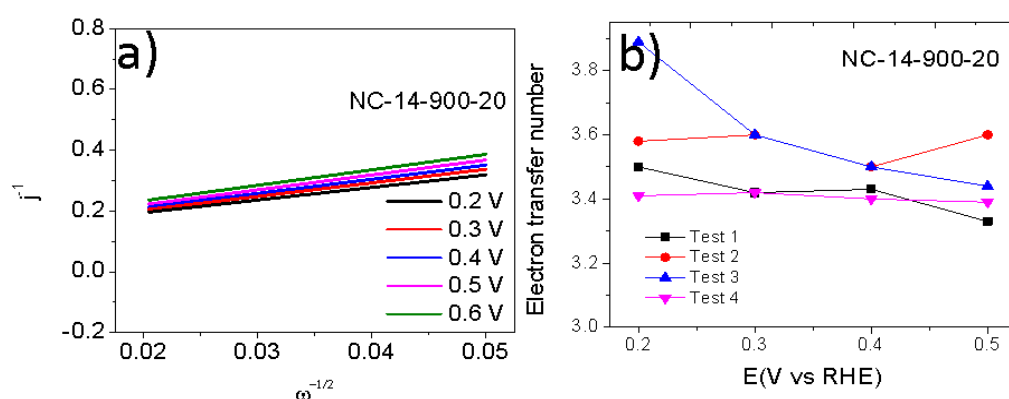
Figure 4.10-a) Koutecky-Levich plot and **b)** corresponding electron transfer number values.
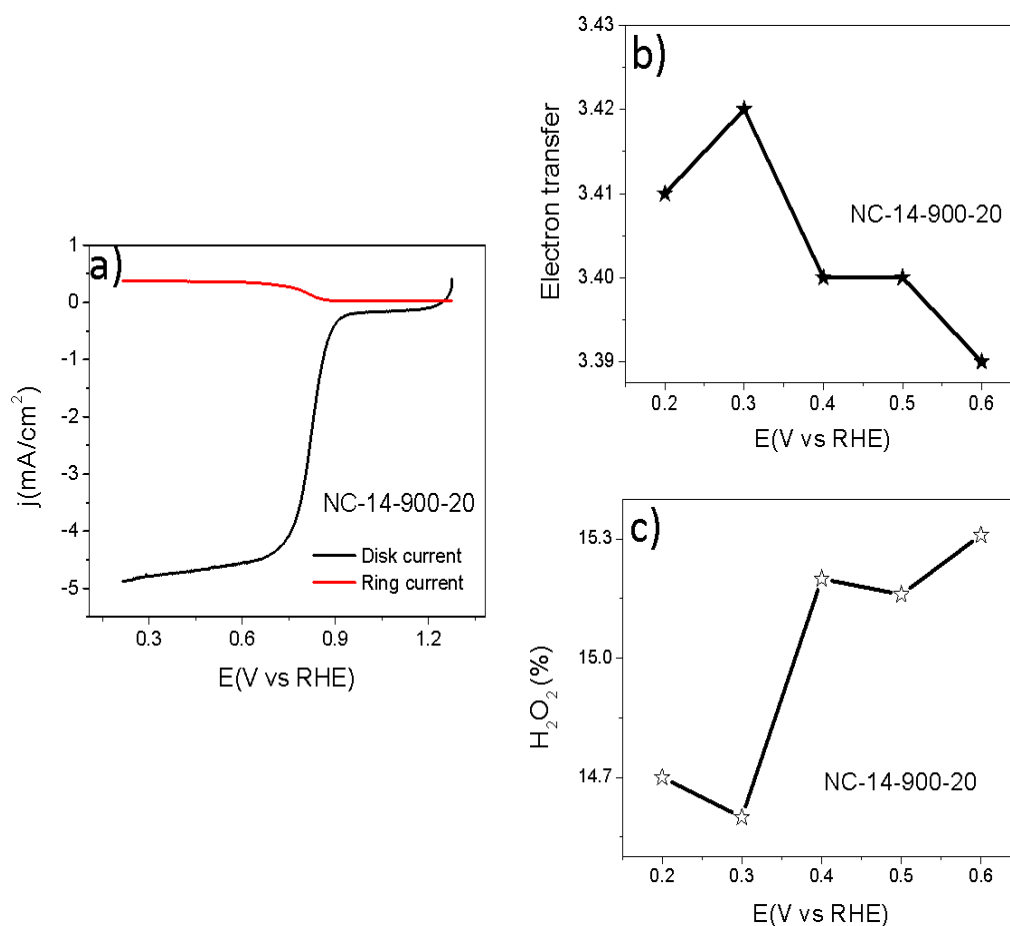
Figure 4.11-a) LSV curves show the current collected at ring and disk, and **b)** corresponding electron transfer number, and **c)** Peroxide generation.

The catalyst also possesses a remarkable stability in alkaline solution. After chronoamperometric operation of 10 h, the NC-14-900-20 catalyst shows almost no attenuation in current, while commercial catalyst Pt/C showed the current decrease of about 20% (**Figure 4.12-a**). Apart from high ORR performance and stability test, the sample NC-14-900-20 was also made subject for methanol poisoning crossover effect. As can be seen in **Figure 4.12-b**, the catalyst shows excellent resistance towards methanol, corroborated by almost mirror image of CV curves with and without methanol.
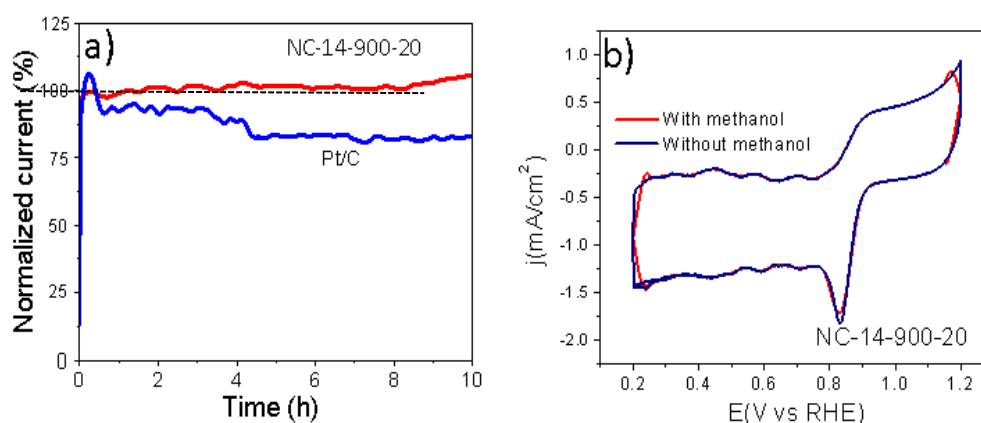
Figure 4.12-a) Stability test shows the normalized current and **b)** CV before and after the methanol poisoning test of the catalyst sample NC-14-900-20.

Figure 4.13-a shows the CV curves of the sample NC-14-1000-20. When the electrolyte was purged with nitrogen, there was no peak (red curve), but when purged with oxygen, there was the appearance of a current density peak (black curve). The onset potential was identified at the value of 0.89 V vs RHE and peak potential at 0.8 V vs RHE as shown in **Figure 4.13-b** (and **Figure 7.1-b** in Appendix). Notice that the cathodic current increases with increasing rotational speed, and for the sample NC-14-1000-20, the current density curves present slight slope between 0.2-0.6 V vs RHE. **[23]**, **[92]**- **[94]**
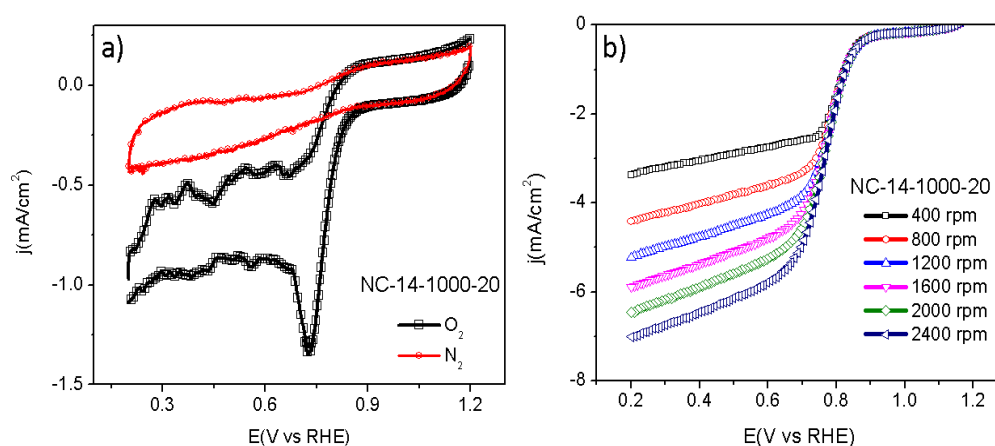
Figure 4.13-a) CV curves of NC-14-1000-20 and **b)** LSV curves of NC-14-1000-20.

Koutechy-Levichy (K-L) plot (j^{-1} vs. $\omega^{-1/2}$), derived from the LSV curves between the potential range of 0.2 to 0.5 V vs RHE at different rotating speeds shows the parallel fitting correlation, further suggesting the first order reaction kinetic with respect to oxygen concentration and potential dependent electron transfer rate (**Figure 4.14-a**). **[101]** The values of electron transfer numbers of the sample NC-14-1000-20, were calculated using two ways, via Koutecky-Levich and by current collected in disk and ring. Koutecky-Levich curves are shown in **Figure 4.14-b**. The average electron transfer number values were calculated according to the potentials 3.13 (0.2 V vs RHE), 3(0.3 V vs RHE), 3 (0.4 V vs RHE), 2.95 (0.5 V vs RHE). Further, ORR activity was tested by rotating ring disk electrode, as can be seen the suppressed ring current indicates good ORR at 1600 rpm (**Figure 4.15-a**). However, by using the currents collected at the disk and ring; the values of peroxide production showed about 28% (**Figure 4.15-b**) and the electron transfer number values of 2.95 (0.2V), 2. 9V (0.3V), 2.8(0.4V), 2.82 (0.5V) and 2.81V (0.6V) (**Figure 4.15-c**).
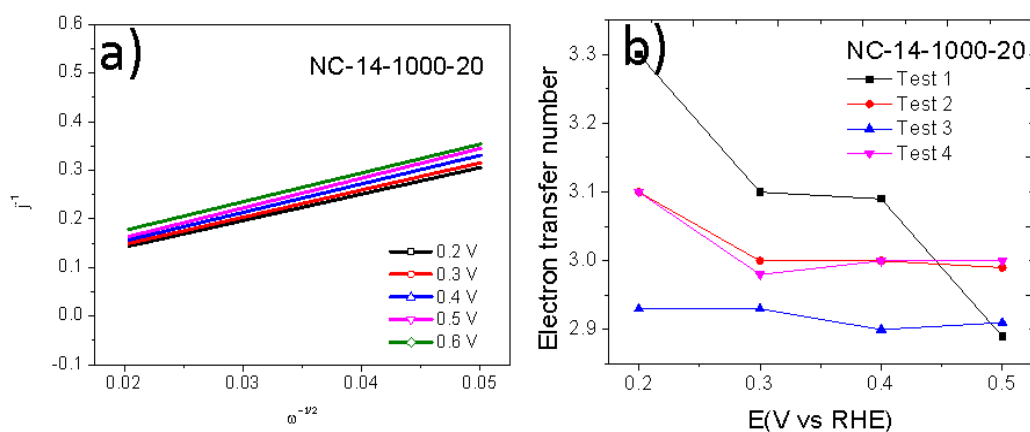
Figure 4.14-a) Koutecky-Levich plot of NC-14-1000-20 and **b)** corresponding electron transfer number values of NC-14-1000-20.
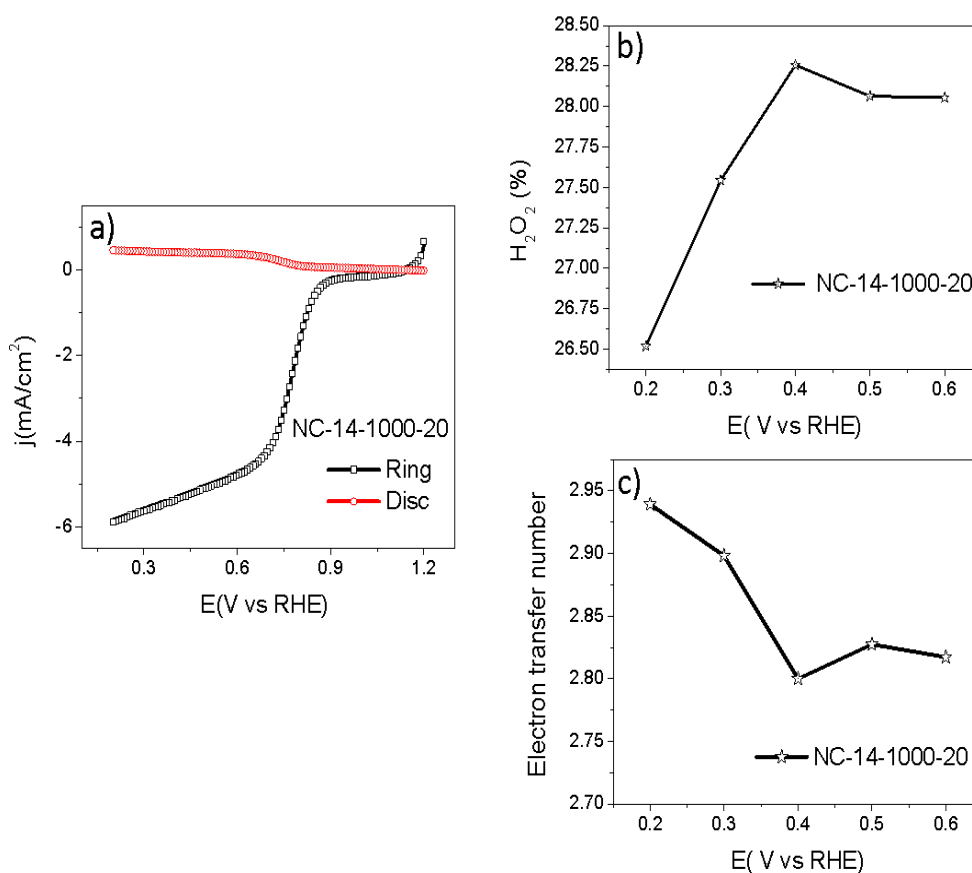
Figure 4.15-a) LSV at ring disk electrode for NC-14-1000-20, **b)** Plot for Peroxide production, and **c)** corresponding electron transfer number.

Figure 4.16-a shows the comparative LSV curves of NC-14-900-20, NC-14-1000-20, and commercial Pt/C (20 wt%) at rotating speed of 1600 rpm. The NC-14-900-20 exhibits better catalytic activity in terms of high onset potential (0.90 V vs RHE) and high half-wave potential (0.84 V vs RHE) which outcompetes that of the counterpart NC-14-1000-20 (0.89 V vs RHE and 0.79 V vs RHE). The obtained onset potential (0.90 V vs RHE) for NC-14-900-20 is appreciable compared with that of the benchmark Pt/C (0.99 V vs RHE). Notably, the negligible performance of pristine Si_3N_4 nanospheres indicates that the catalytic ORR performances of NC-14-900-20 and NC-14-1000-20 are originating only from the nitrogen doped carbon. Although the simplistic comparison between NC-14-900-20 and NC-14-1000-20 is not ideal. One can point out that the enhanced ORR activity in NC-14-900 seems to be related to the higher content of nitrogen,

the amount of pyridinic-N active sites and even due to presence of different nitrogen species as identified in the XPS survey.
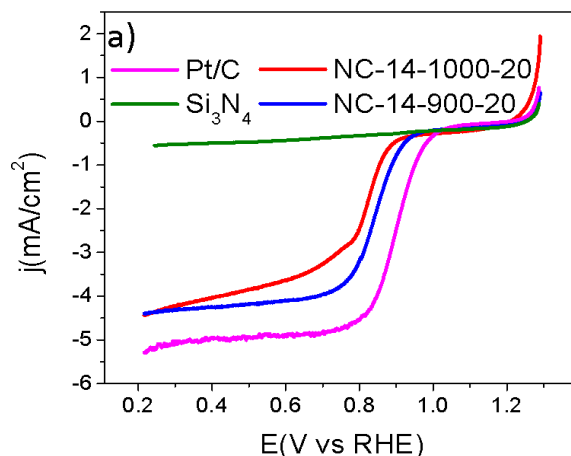
Figure 4.16-a) Comparison of the LSV curves at 1600 rpm of Pt/C, Si_3N_4, NC-14-900-20 and NC-14-1000-20.

Temperatures of 900℃ and 1000℃ can be considered optimal temperatures for converting PANI into nitrogen doped carbon. The resulting nitrogen doped carbon produced electrocatalytic ORR activity showing onset potential of 0.90 V vs RHE and 0.89V vs RHE for NC-14-900-20 and NC-14-1000-20, respectively. The values of electron transfer number near to ~ 3.4 and low peroxide production ~ 20% for the NC-14-900-20, signalize the existence of mixed path tending towards the four-electron transfer pathway.

In terms of electrochemical characterizations, the deconvolution of N1s XPS spectra for NC-14-1000-20 (**Figure 4.5-b**) showed 79.5% pyridinic-N (397 eV) and 20.5% pyrrolic-N species but no presence of quaternary-N, in the case of of NC-14-900-20, it showed 70.4% pyridinic-N (398 eV), 29% pyrrolic-N (399 eV) and 0.6% quaternary-N (400 eV) (**Figure 4.6-b**). It has been shown in previous studies that the pyridinic-N was responsible for high catalytic onset potential for ORR via four-electron path. As pyridinic-N species contributes with a single electron pair in the plane of carbon lattice by weakening the O-O bond for oxygen reduction. Besides that, in order to correlate the content of nitrogen species with the catalytic performance, one must take into consideration that the

co-existence of pyridinic-N, pyrrolic-N and quaternary-N can also generate synergistic effect due to their different electronic configurations, consequently improving the catalytic performance of the catalyst material.

According to the physical and electrochemical characterizations, the enhanced catalytic performance of catalyst NC-14-900-20, overall can be assigned to the unique coral-like morphology, abundance of mesopores and high nitrogen doping, promoting high mass transport and accessibility of the active sites.

4.2 Physical and electrochemical characterizations of sulfur and nitrogen co-doped carbon coated silicon nitride nanospheres (Si_3N_4)

Sulfur and nitrogen co-doped carbon was characterized by TEM as shown in **Figure 4.17**. In the TEM images of sample SNC, a modified coral-like structure is present. Although there is resemblance of coral-like structure, certain regions of the sample show the superposition of carbon wrapping the nanometric Si_3N_4. This morphology observed in the sulfur-nitrogen doped carbon resulted from the process of polymerization of PANI followed by carbonization and its reutilization as core for the polymerization and carbonization of PEDOT, as described in the experimental part. Such unique morphological design and synergy of co-doping could be beneficial for increasing specific surface area and more active sites for the electrocatalysis.
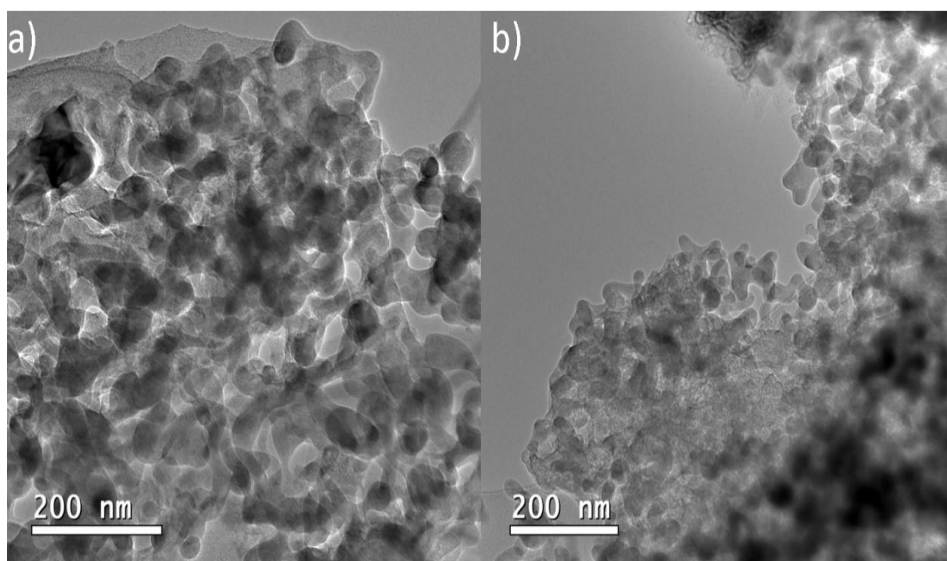
Figure 4.17-a,b) TEM images of sample SNC.

The corresponding energy dispersive X-ray spectroscopy (EDS) is shown in **Figure 4.18-a**. The elemental mapping reveals carbon, silicon, nitrogen, and oxygen homogeneously distributed. The broadcasted heteroatoms in the carbon network are important to create the electrocatalytic efficiency of the catalyst and in some works of literature considered responsible for the synergistic effect that further enhances ORR. **[38]-[42]**
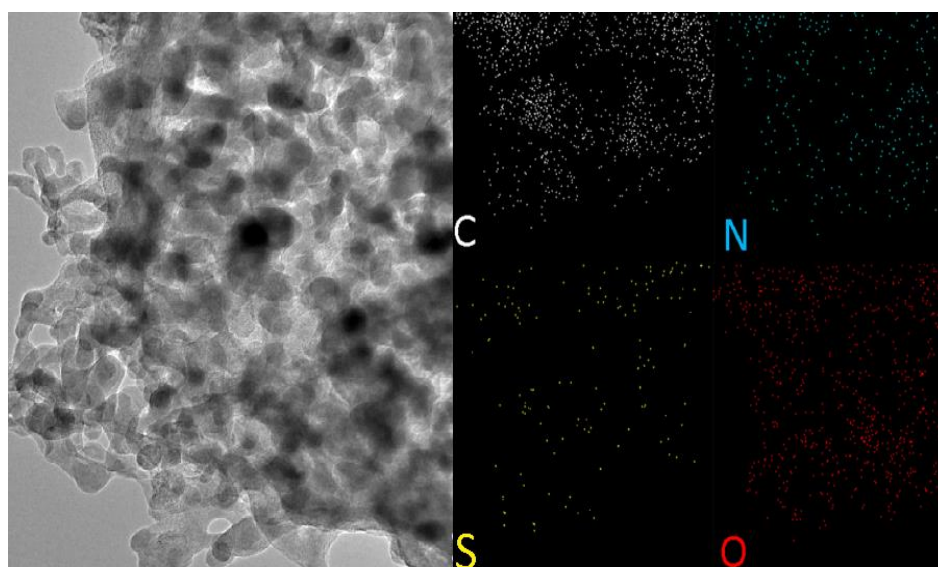
Figure 4.18-a) TEM image of sample SNC and **b)** corresponding EDS spectra for elements nitrogen, sulfur, carbon and oxygen.

Figure 4.19-a shows the XPS survey of sample SNC, with atomic percentage of 18.5% oxygen, 52% carbon ,13% nitrogen, 0.6%, sulfur and 15.9% silicon. Deconvolution of XPS spectra of C 1s (**Figure 4.19-b**) shows peaks assigned to C=C/C-O (288 eV) (9.8%), C-N (286.2 eV) (5.2%), and C=C/C-C (284.4 eV) (85%). **Figure 4.19-c** shows the XPS spectra of N 1s assigning the peaks for pyrrolic-nitrogen (58.3%) at 398.5 eV, pyridinic-nitrogen (33.5%) at 397 eV, and quaternary-nitrogen (8.2%) at 400eV. The XPS spectra of S 2p shows the presence of thiophenic sulfur S-C/S=C (**Figure 4.19-d**).
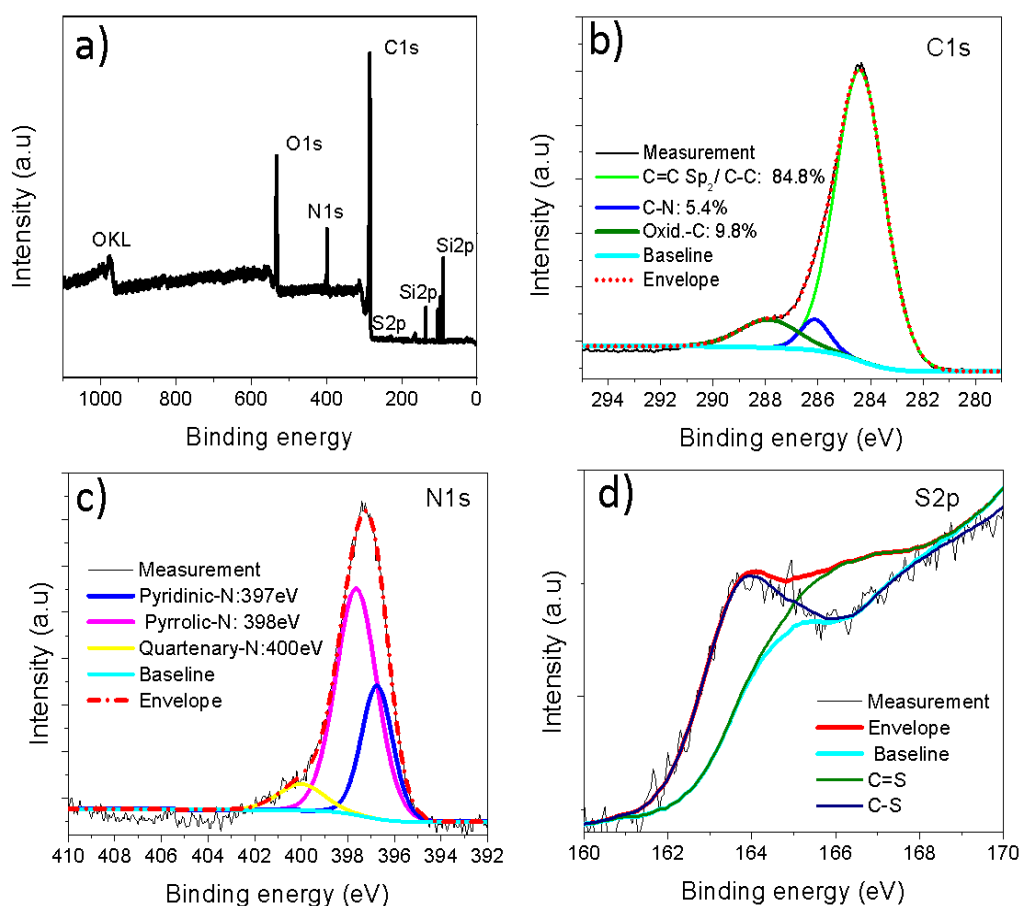
Figure 4.19-a) XPS survey spectra of SNC, **b)** XPS spectra of C 1s, **c)** XPS spectra of N 1s, **d)** XPS spectra of S 2p.

Figure 4.20-a presents the CV curves of SNC in oxygen and nitrogen saturated electrolyte, which shows the strong oxygen reduction cathodic peak at potential near 0.8 V vs RHE and onset potential at 0.9 V vs RHE. LSV curves are

represented in **Figure 4.20-b** (and **Figure 7.2-a** in Appendix). The LSV curves show the steady-state regime in which, each one of the current density curves reaches a stable value as the potential is swept. They also show increase in current density with higher rotating speed. Using the values of the current density and rotation speed, Koutecky-Levich plots were constructed (**Figure 4.21-a**) and the electron transfer number values calculated to the specific potentials as follow: as shown in **Figure 4.21-b**.
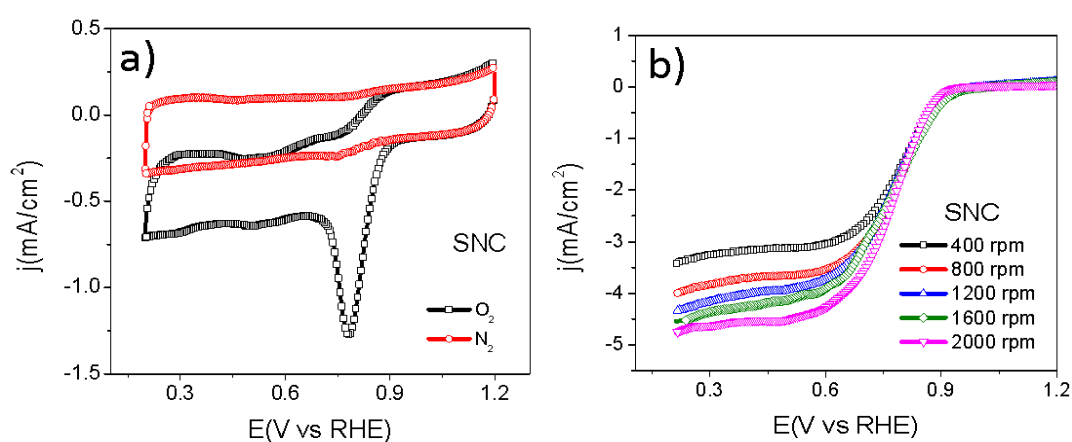
Figure 4.20- a) CV curves of SNC, and **b)** LSV curves of SNC.
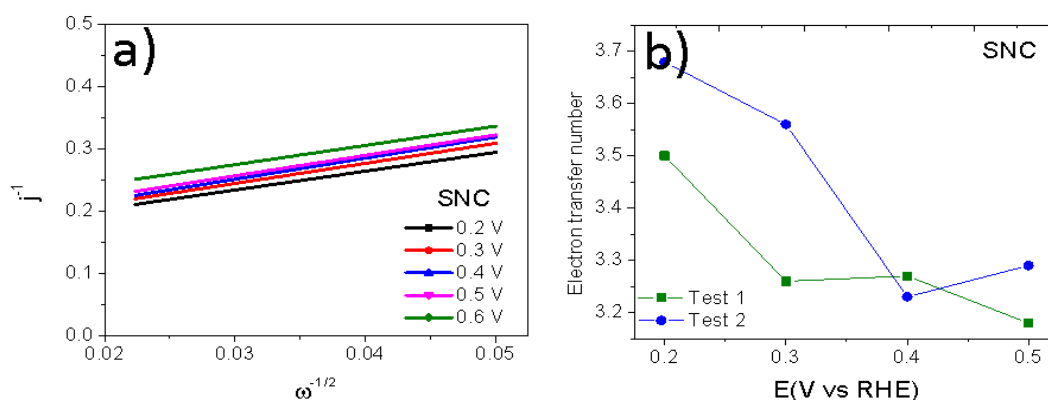
Figure 4.21-a) Koutecky-Levich plot, and **b)** corresponding electron transfer number.

      Figure 4.22-a shows a methanol crossover test of sample SNC. As can be seen, the SNC demonstrated good resistance toward methanol poisoning. The chronoamperometric operation was performed to test the stability of the

catalyst, as shown in **Figure 4.22-b**; the sample SNC shows stable current during 9 h of chronoamperometric operation, indicating good stability of the catalyst SNC in alkaline solution (0.1M KOH).
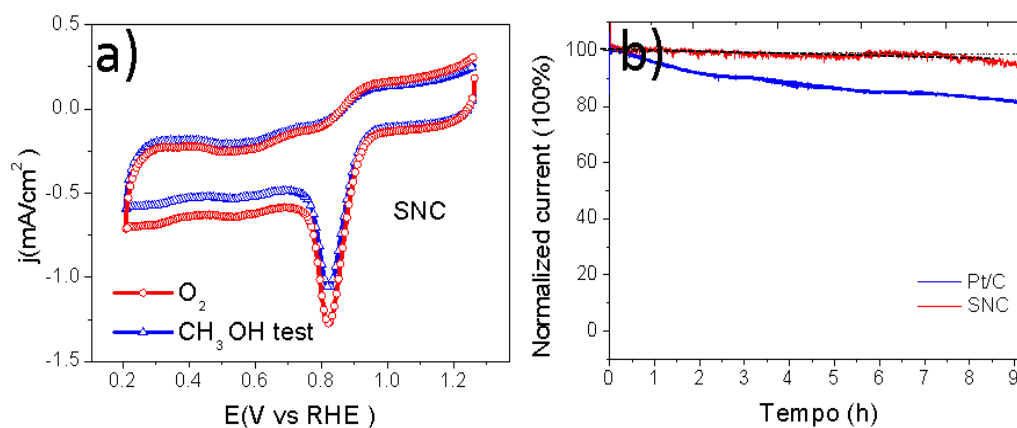
Figure 4.22-a) CV curves with and without methanol and **b)** Chronoamperometric test.

4.3 Physical and electrochemical characterizations of sulfur doped carbon coated silicon dioxide nanospheres (SiO$_2$, 200 nm)

Figure **4.23-a, b,** and **4.24-a** show the SEM images of the sulfur doped carbon coated silica particles. The successful coating of carbon can be observed all around the SiO$_2$ nanospheres.
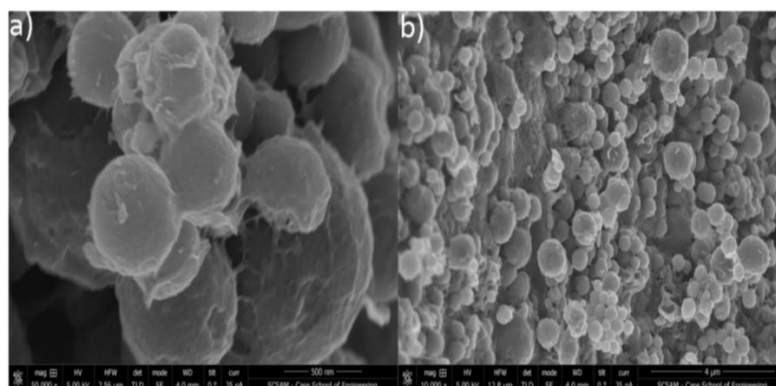
Figure 4.23-a, b) SEM images of SC-900 at different magnifications.

EDS analysis mapped the elements: carbon (44.5%), oxygen (35.2%), silicon (16 %), and sulfur (4.3 %) homogeneously distributed in the sample as seen in **Figure 4.24-a**.
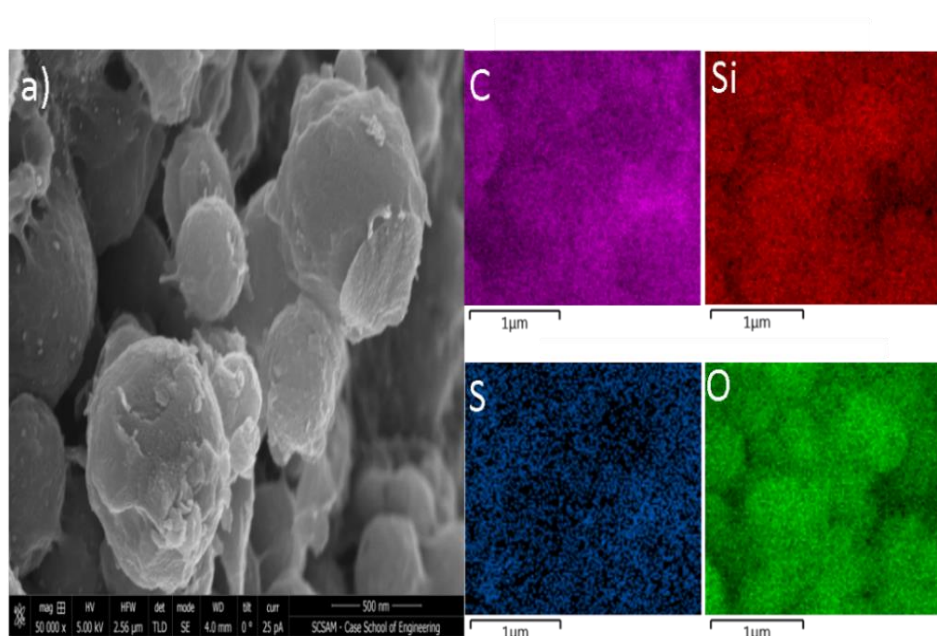
Figure 4.24- a) EDS of sample SC-900, identified 44.5 %Carbon, 35.2% Oxygen, 16 % Silicon and 4.3 % Sulfur.

Figure 4.25-a) shows XPS survey spectra of SC-900 with carbon (70.8%), sulfur (1.1%), silicon (8.6%), and oxygen:19.5%. The XPS spectra of C 1s (**Figure 4.25- d**) shows the presence of C=O bonds (285 eV) and C=C bonds (284 eV). The Deconvolution of the XPS spectra of S 2p in **Figure 4.25- c)**, identified presence of 32.4% of oxidized sulfur (167 eV), 34.6% of thiophenic sulfur with S=C bonds (163 eV), and 33% of thiophenic sulfur with S-C bonds (164 eV). Thus being 67.6% of sulfur content present in the sample in the thiophenic-like.
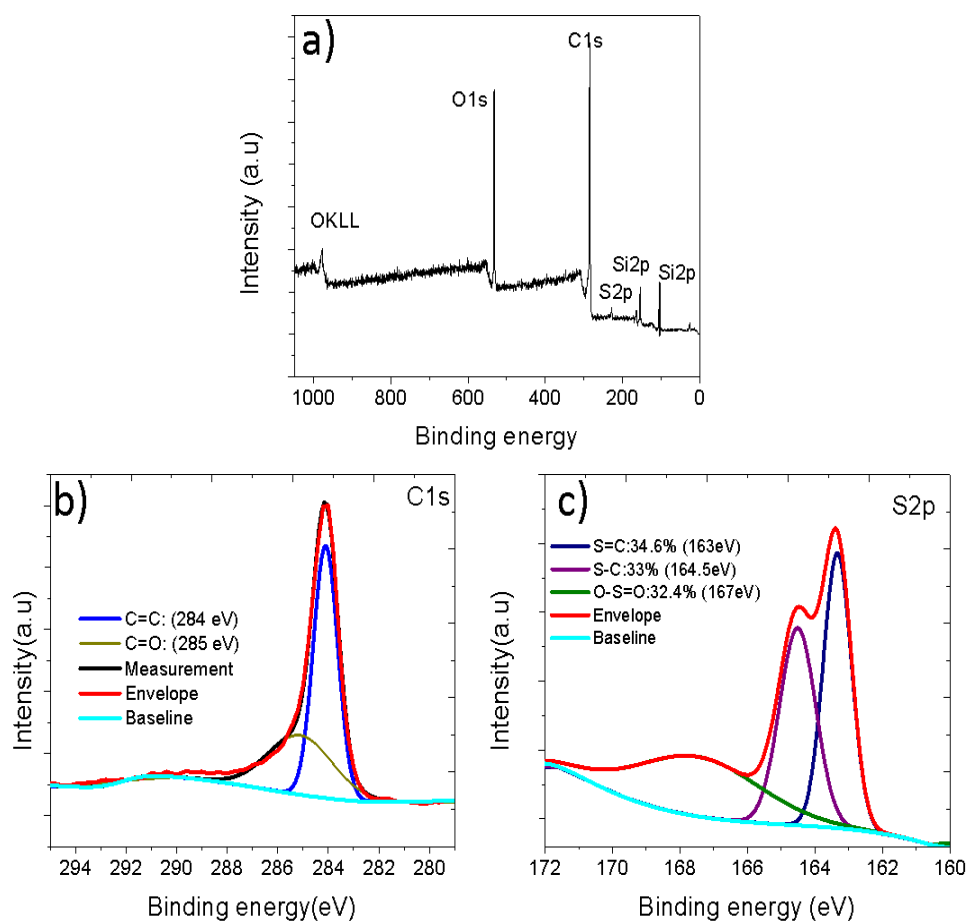
Figure 4.25-a) XPS survey spectra of SC-900, **b)** XPS-HR spectra of C 1s, and **c)** XPS-HR spectra of S 2p.

XRD analysis (**Figure 4.26-a**) shows two peaks; the peak at 23° represents presence of crystallinity and the peak at 42°represents presence of Sp^2carbon; which means that the polymer was fully carbonized. Raman spectra shows two bands, G-band (1358 cm^{-1}) and D- band (1592 cm^{-1}). The bands intensity ratio I$_D$/I$_G$: 0.91 is indicative of mostly graphitic carbon with low disorder (**Figure 4.26-b**).
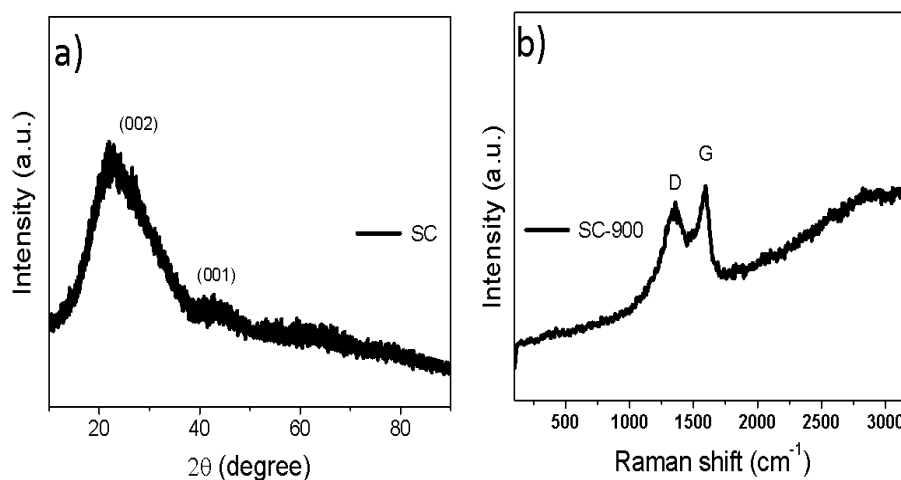
Figure 4.26-a) XRD pattern of SC-900, and **b)** Raman spectra of SC-900.

The CV curves of SC-900 were tested in oxygen and nitrogen saturated 0.1 M KOH electrolyte. A reduction peak can be observed in the black curve, which represents when the CV measurement was performed in oxygen saturated electrolyte, assigning activity of the catalyst SC-900 (**Figure 4.27-a)**. LSV curves of SC-900 (**Figure 4.27-b)** show an onset potential near 0.8 V vs RHE at different rotational speeds. Koutecky-Levich plot (**Figure 4.28-a**) and electron transfer number values in relation to each potential are shown in **Figure 4.28-b**. The average electron transfer number value was 2.6.
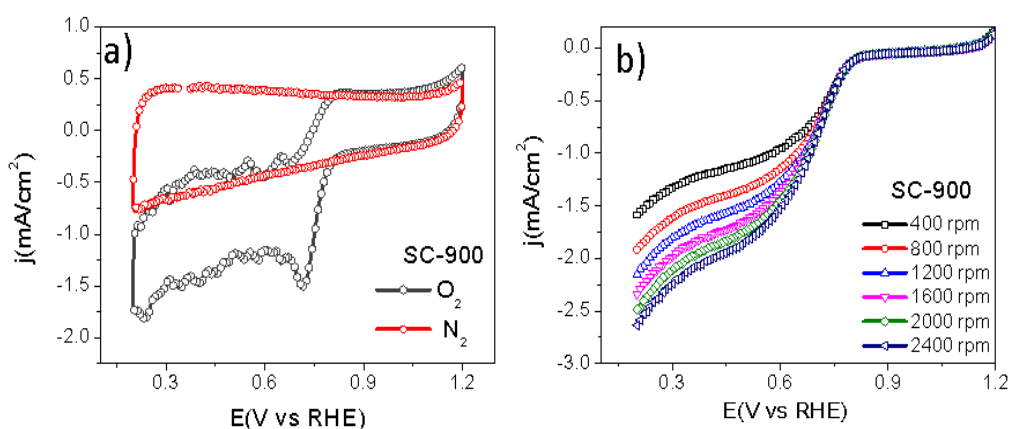
Figure 4.27-a) CV curves of SC-900, and **b)** LSV curves of SC-900.
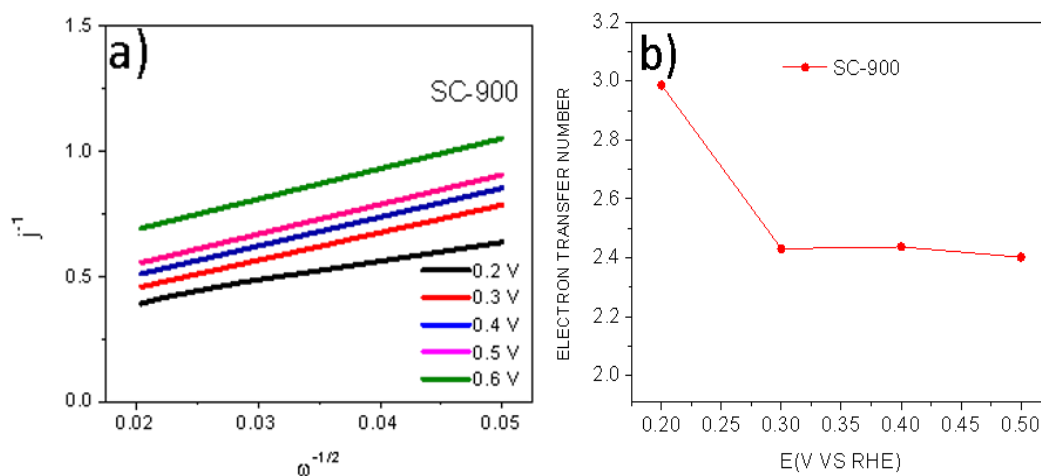
Figure 4.28-a) Kouteck-Levich plot of SC-900, and **b)** electron transfer number values of SC -900.

Figure 4.29-a shows the CV curves comparison of samples SC-800, SC-900 and SC-1000 and shows the oxygen reduction peak and an onset potential ~ 0.80 V vs RHE in oxygen saturated 0.1M KOH. **Figure 4.29- b** shows the electron number values for the respective samples SC-800, SC-900 and SC-1000.
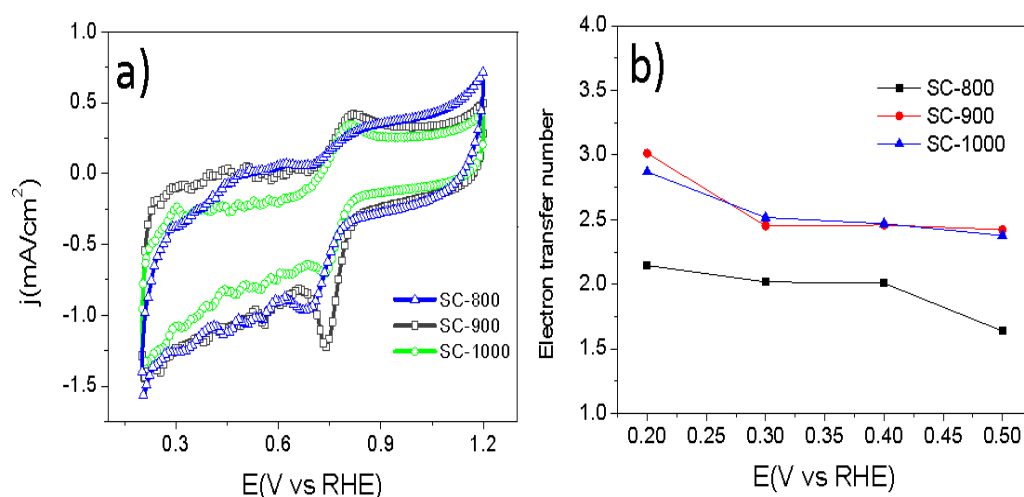
Figure 4.29-a) CV curves of SC-800, SC-900, and SC-1000, and **b)** electron transfer number values of SC-800, SC-900 and SC-1000.

4.4 Physical and electrochemical characterizations of nitrogen and sulfur co-doped carbon coated silicon dioxide nanospheres

TEM images of the sample NSC-900 (**Figure 4.30-a, b, c, d**) revealed the carbon coating around the silicon dioxide core particles, derived from PEDOT and PANI after carbonization. **Figure 4.30-a**, reveals the carbon layer formed around a single silica core particle, while **Figure 4.30-b, c, d**) shows carbon with fibrous-like morphology coated over the silica cores (**Figure 4.30-a, b, c, d**).
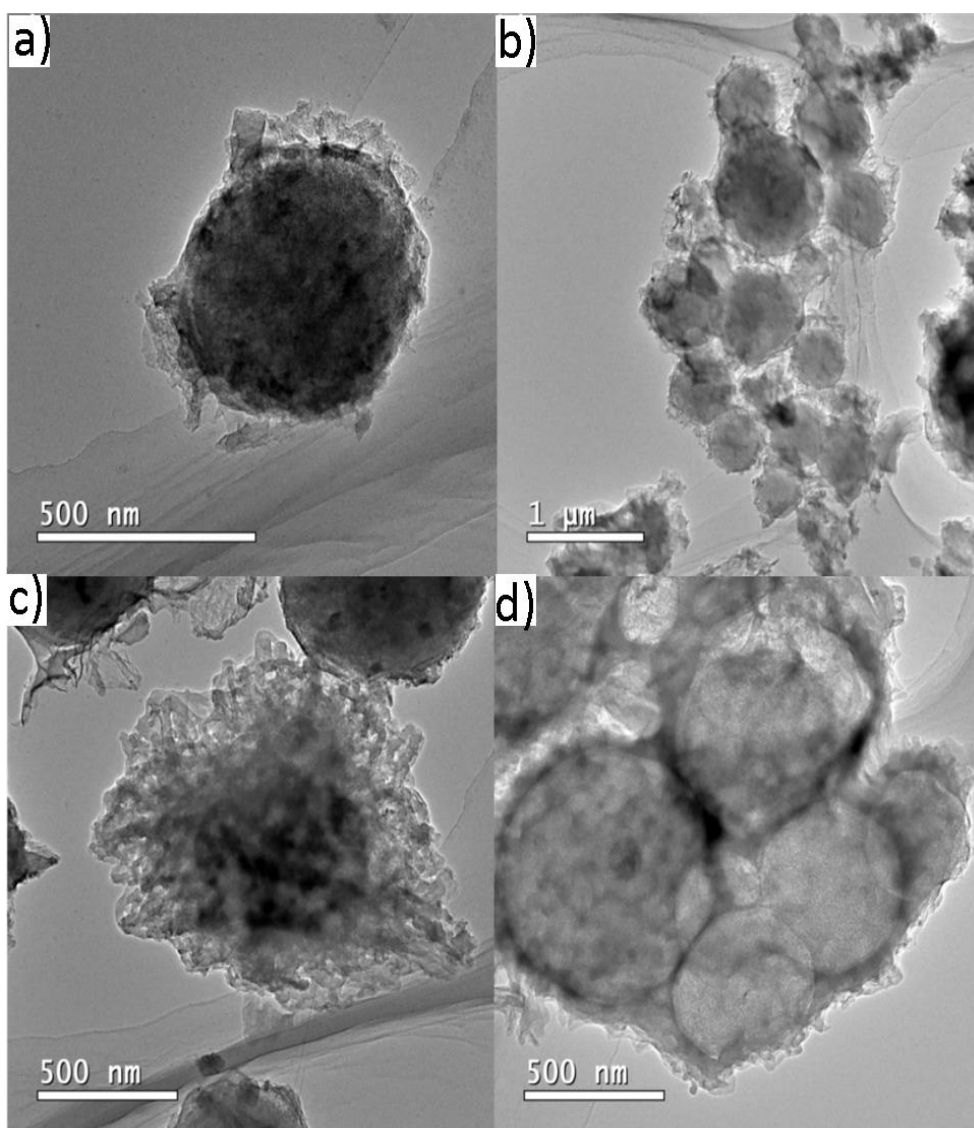
Figure 4.30-a-d) TEM images of NSC-900.

Figure 4.31- a) shows the SEM image of nitrogen and sulfur co-doped carbon coated silica with respective mapping. Mapping revealed the distribution of the elements carbon(pink), nitrogen(yellow), oxygen(green), silicon (red) and sulfur (blue), and the respective EDS identified the contents of 73.5% carbon, 3.3% nitrogen, 13.4%oxygen, 6.8% silicon and 3%sulfur.
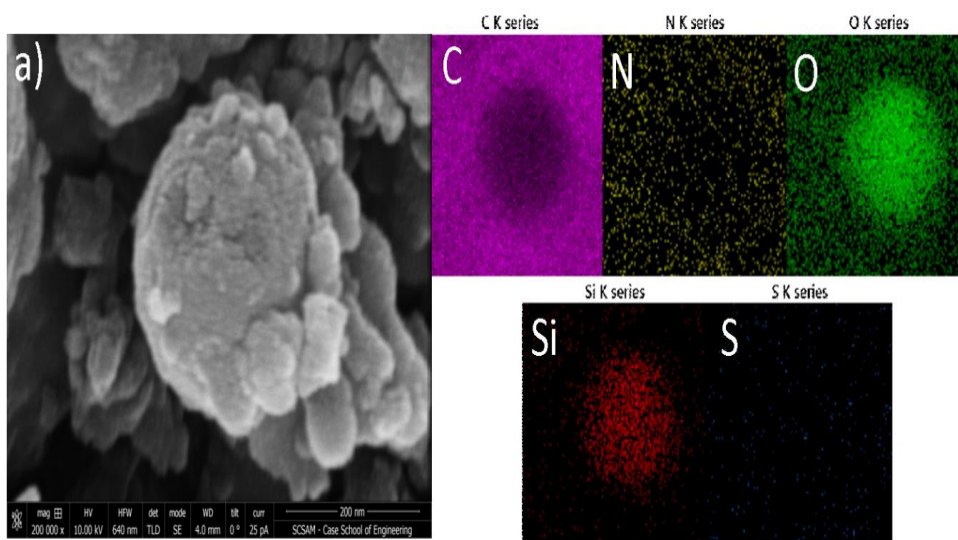
Figure 4.31- a, b) SEM image of nitrogen and sulfur co-doped carbon coated silica particles. Mapping shows the elements C, N, O, Si, S, and O.

XPS survey of sample NSC-900 in **Figure 4.32-a)** identified contents of 3% nitrogen, 1% sulfur, 12.9% oxygen, 10.6% silicon and 71.5% carbon, which corroborates with the information from EDS analysis. **Figure 4.32- b)** shows the C1s spectra, presenting C=O (285 eV) and C=C (284). The XPS spectra of N 1s (**Figure 4.32-b**) shows the presence of pyridinic-nitrogen (15%) at 397 eV, pyrrolic-nitrogen (9%) at 398.1 eV, quaternary-nitrogen (64%) at 401.3 eV and oxidized-nitrogen (12%) at 406 eV. The presence of oxygen is common in carbon-based materials because carbon is susceptible to oxygen absorption, even at low temperature, as previously discussed, and the presence of nitrogen and sulfur elements indicates the co-doping of the carbon. **[92]**
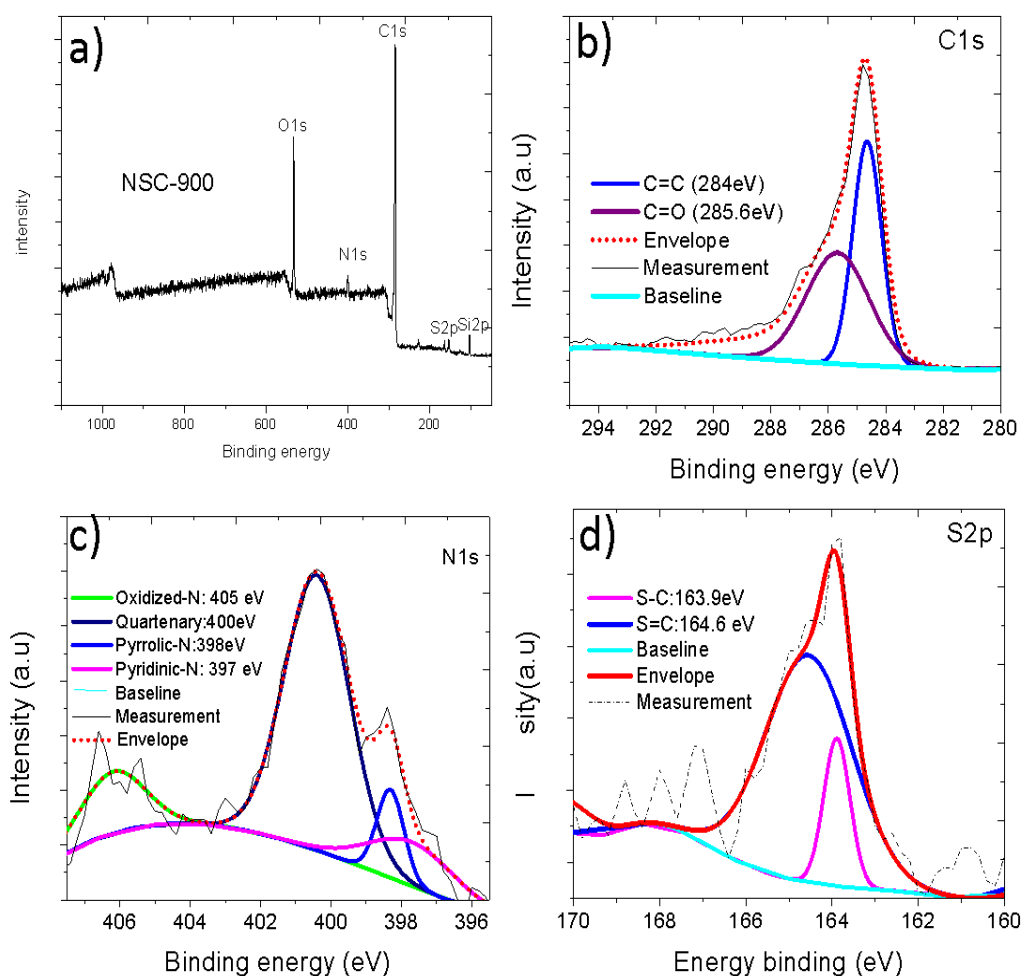
Figure 4.32-a) XPS survey of sample NSC-900, **b)** XPS spectra of C1s, **c)** XPS spectra of N1s spectra, and **d)** XPS spectra of S2p.

TEM images of the sample NSC-HF shows fibrous-like morphology of carbon (NSC-HF), and there is no presence of the silica core particles anymore (**Figure 4.33-a, b, c, d)**. These images reveal that after the etching treatment, there was complete removal of the silica cores. The fibrous-like or nest-like morphology of the co-doped carbon catalyst is considered ideal because it facilitates the access and contact of the electrolyte with the catalytic sites at the surface of material.
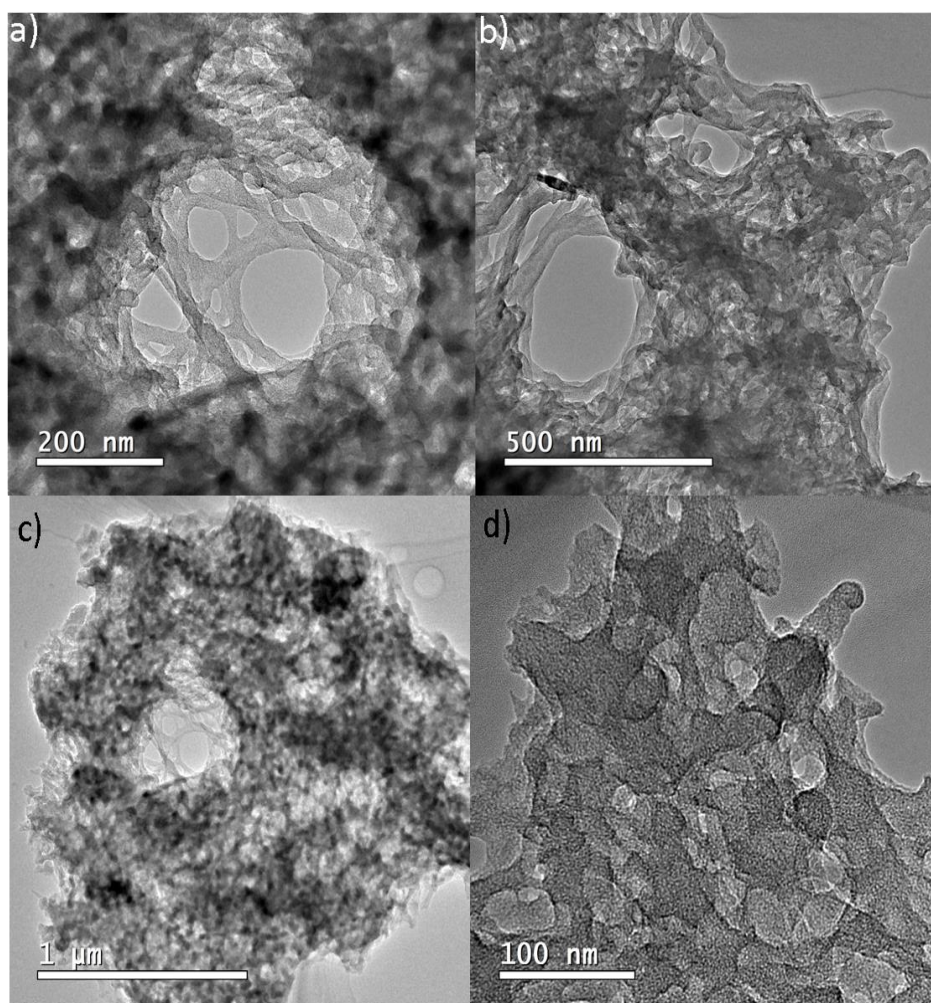
Figure 4.33-a, b, c, d) TEM images of NSC-HF.

XPS survey spectra of NSC-HF (**Figure 4.34- a**) confirms the presence of nitrogen (4%), sulfur (1.2%), oxygen (6.1%), and carbon (88.7%). That means that the nitrogen and sulfur contents are preserved after the hydrofluoric acid washing treatment, and there is removal of the silicon content, as expected. **Figure 4.34-c)** shows the N1s spectra with 21% pyrrolic-nitrogen (398 eV), 15.2% pyridinic-nitrogen (397 eV) and 63.8% quaternary-nitrogen (400 eV). The nitrogen species found are quaternary-N, pyrrolic-N and pyridinic-N, in agreement with the types found in the sample before the acid treatment for removal of the cores.

The XPS spectra of S 2p can be deconvoluted into 16% C-S bonds (163.2eV), 62% C=S bonds (164.8eV) and oxide of sulfur 22%(168eV) (**Figure

4.34-c). **[38],[97]** The XPS spectra of C 1s (**Figure 4.34-d**) can be deconvoluted for C=C bonds at 284.4 eV, and C-N/C=O bonds at 285 eV. **[64]**, **[94]**-**[96]**
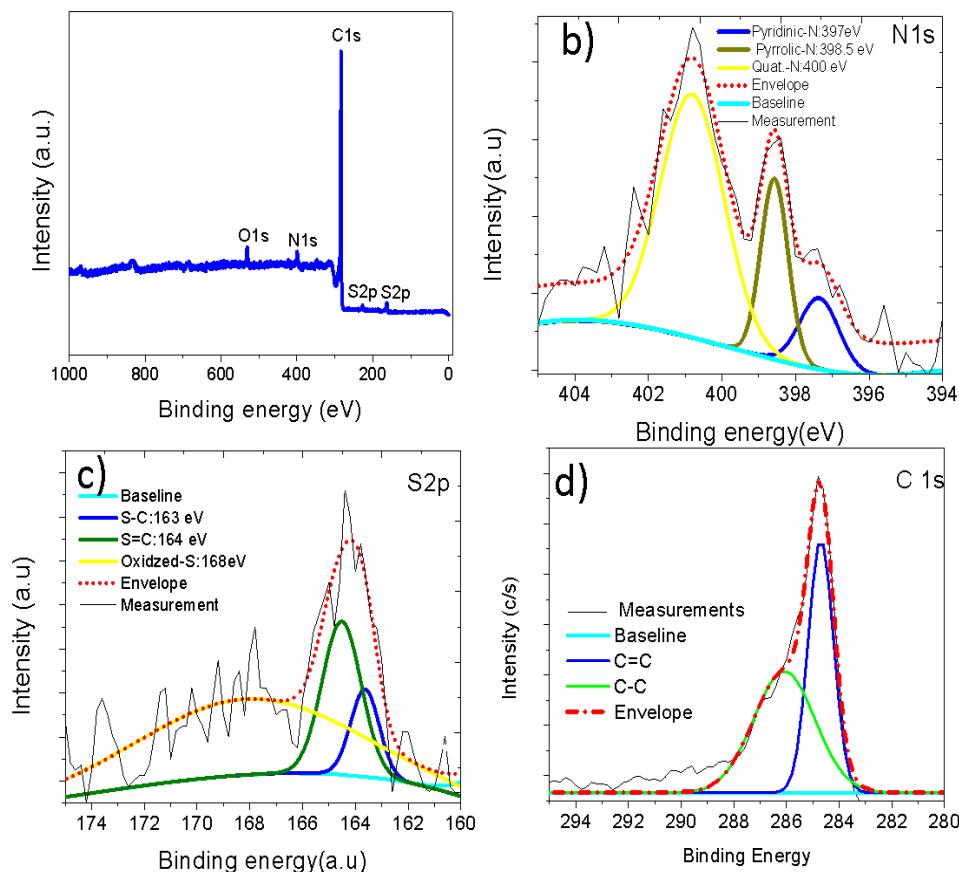
Figure 4.34-a) XPS survey of sample NSC-HF, **b)** XPS spectra of N1s, **c)** XPS spectra of S2p, and **d)** XPS spectra of C1s.

XRD pattern of sample NSC-HF shows a peak at 24^0 indicating the dominant presence of amorphous carbon phase, and a peak at 44^0 suggesting partial formation of crystalline graphitic-like phase (**Figure 4.35-a**). Raman spectra showed two peaks referring to the graphitic carbon / G-band (1588 cm^{-1}) and disordered carbon. D-band (1341 cm^{-1}). Intensity ratio I_D/I_G =0.92 indicates high graphitization and low defects, and the intensity ratio I_{2D}/I_G indicates presence of multilayered carbon (**Figure 4.35-b**). Surface area of sample NSC-HF was found 341 m^2/g (**Figure 4.35-c**) and mesopores with diameters ranging from 1.7 to 50 nm (**Figure 4.35-d**).
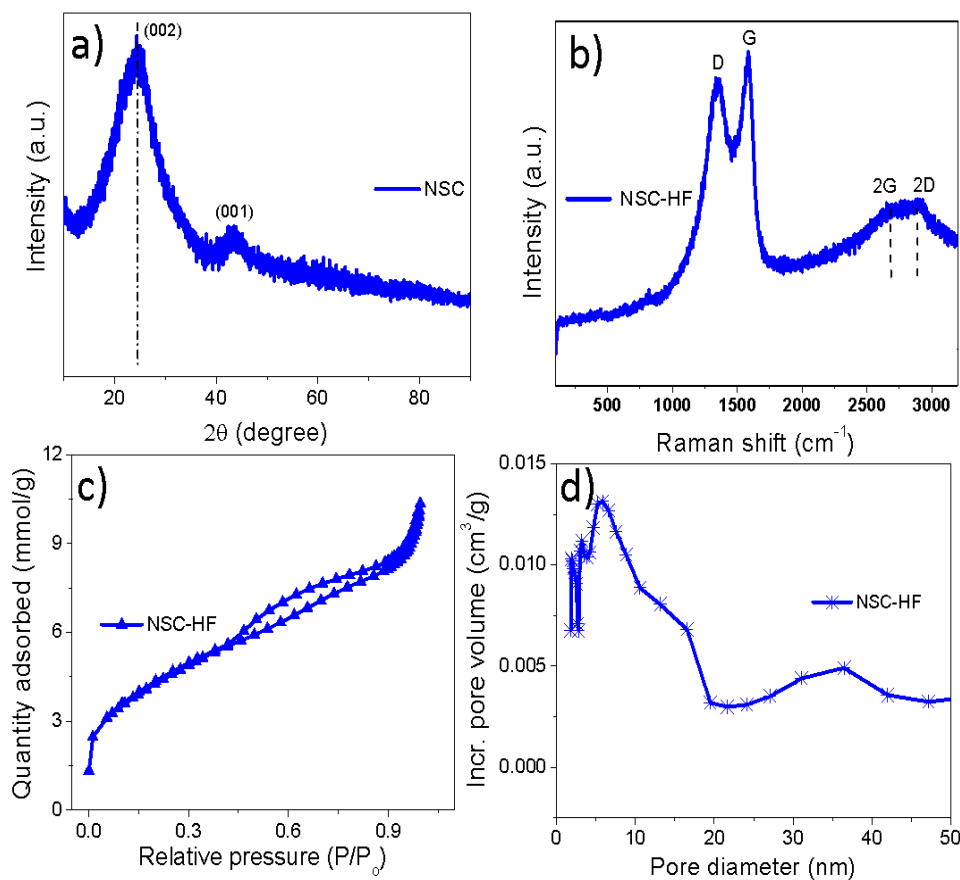
Figure 4.35-a) XRD survey, **b)** Raman spectra, **c)** Adsorption/desorption isotherm curve and **d)** porosity of the sample NSC-HF.

Figure 4.36-a shows the CV curves of the sample NSC-900. The black curve with reduction peak was obtained when the CV measurement was performed in oxygen saturated 0.1 M KOH electrolyte. There is no peak in the current density when the electrolyte was only purged with nitrogen (red curve).

Onset potential of NSC-900 was found at 0.9 V vs RHE. **Figure 4.36-b** (and **Figure 7.3-a** in Appendix) show the LSV curves with onset potential of 0.90 V vs RHE at different rotational speeds. The increase of rotation speeds causes an increase in current density. The LSV curves show a flat plateau between the potential values of 0.2-0.6 V vs RHE, which signalizes a diffusion-controlled oxygen reduction in alkaline solution (0.1M KOH). **[92]-[94]**
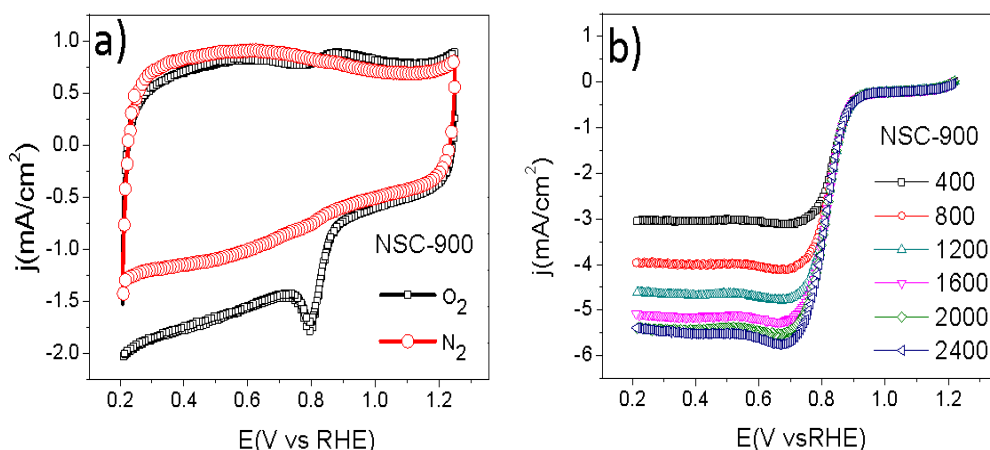
Figure 4.36- a) CV curves of NSC-900 and **b)** LSV curves of the NSC-900.

Koutecky-Levich plot (**Figure 4.37-a**) shows the linear relation between values of j^{-1} and $\omega^{-1/2}$. The average value of electron transfer number was calculated near 3.52 (0.2 V vs RHE), 3.5(0.3 V vs RHE),3.51(0.4 V vs RHE), and 3.47 (0.5 V vs RHE) (**Figure 4.37-b**).
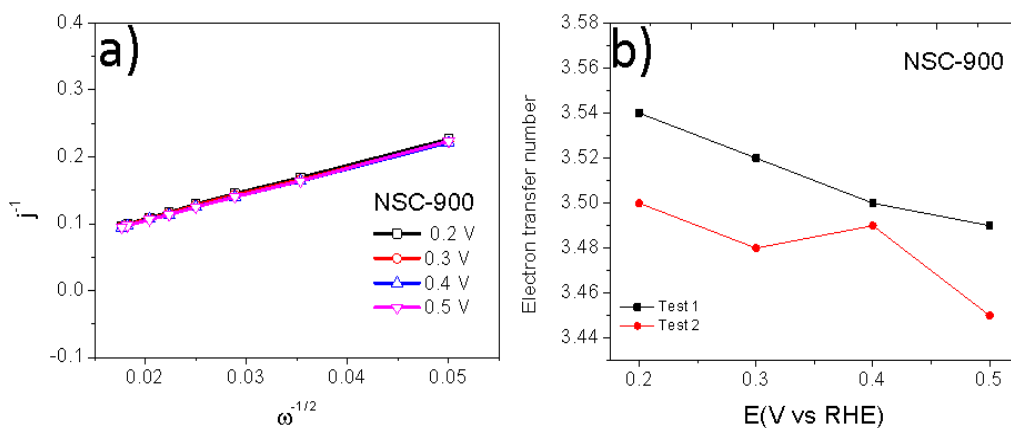
Figure 4.37- a) Koutecky-Levich plot of NSC-900 and **b)** electron transfer number of NSC-900.

Sample NSC-900 (**Figure 4.38-a**) also shows good resistance towards methanol poisoning, and does not show significant loss in onset potential after the addition of methanol. Chronoamperometric test was performed during 10 h (**Figure 4.38-b**).
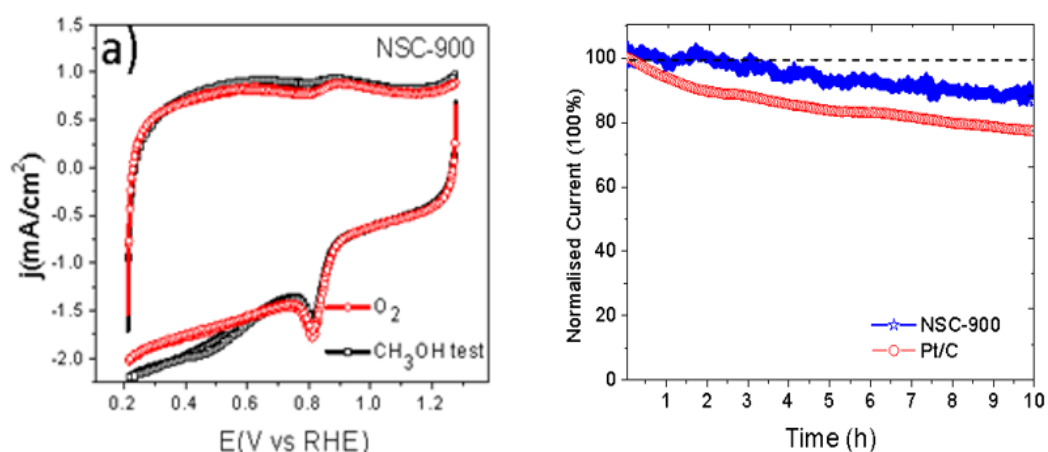
Figure 4.38-a) Methanol cross over test of NSC-900 and **b)** Chronoamperometric test of NSC-900.

CV curve of sample NSC-HF (**Figure 4.39-a)** shows that the onset potential reached 0.94 V vs. RHE, when electrolyte was saturated with oxygen, which outperforms the unetched sample NSC-900 (0.90V vs. RHE). The half-wave potentials of NSC-HF and Pt/C were measured to be near 0.81 and near 0.84 V vs. RHE, respectively. As can be noticed from all of the aforementioned electrocatalytic measurements, the NSC-HF demonstrates the highest ORR activity among all the likewise prepared samples.

This result supports the previously reported work where co-doped carbon exhibits better ORR electrocatalysis with more positive shift in onset potential compared to the single heteroatom doped carbons.**[93]-[96]** The enhanced ORR performance of NSC-HF can be explained due to the synergistic effect between the dopants that promotes better catalytic activity and optimal morphological features acquired with etching of silica cores, increasing surface area and exposing more active sites. The increase in the cathodic current was observed with increasing rotational speeds, which suggests a diffusion-controlled oxygen reduction in 0.1 M KOH electrolyte (**Figure 4.39-b** and **Figure 7.3-b** in Appendix). **[55][98]**
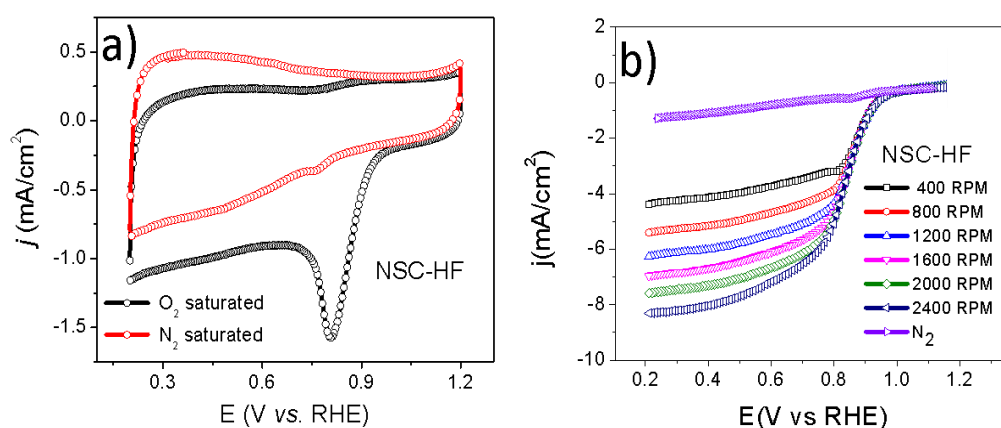
Figure 4.39-a) CV curves of NSC-HF and **b)** LSV curves of NSC-HF

Figure 4.40-a shows the corresponding Koutechy-Levich plot (j^{-1} vs. $\omega^{-1/2}$), which was derived from the LSV curves between the potential range of 0.2 to 0.6 V vs RHE at different rotating speeds. Koutecky-Levich plot (**Figure 4.40-a**) displayed almost linear relation between the current density (j^{-1}) and rotating scan rates ($\omega^{-1/2}$). The electron transfer number values were calculated to the respective potentials (**Figure 4.40-b**). The values collected from four tests shown in **Figure 4.40-b** were used to calculated average value for each potential, 3.95 (0.2 V vs RHE), 3.9 (0.3 V vs RHE), 3.93 (0.4 V vs RHE), and 3.81(0.5 V vs RHE), indicating a tendency towards four electron pathway for ORR catalysis.**[93]**
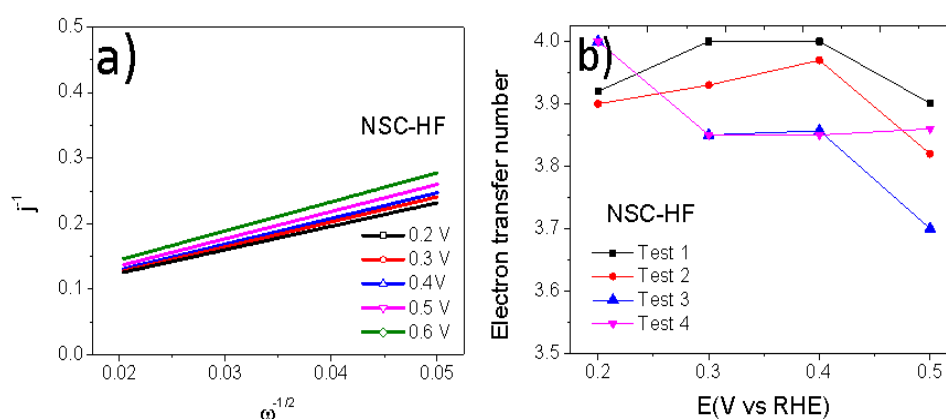
Figure 4.40-a) Koutecky-Levich plot of NSC-HF and **b)** corresponding electron transfer number values.

Current collected at the disk and ring were used to calculate the amount of H_2O_2 generation and electron transfer number values. The peroxide was calculated to be lower than10% for the sample NSC-HF. The low amount of H_2O_2 generation by catalyst NSC-HF is attributed to its high ORR activity with four electron transfer processes. (**Figure 4.41-a,b,c**).

The average electron transfer number measured from a rotating ring-disk electrode (~ 3.8) for NSC-HF was also calculated. The variation in values of electron transfer number, calculated from rotating ring-disk collected currents and Koutecky-Levich plot was also seen in earlier reported works (**Figure 4.41-c**). **[99]-[102]**
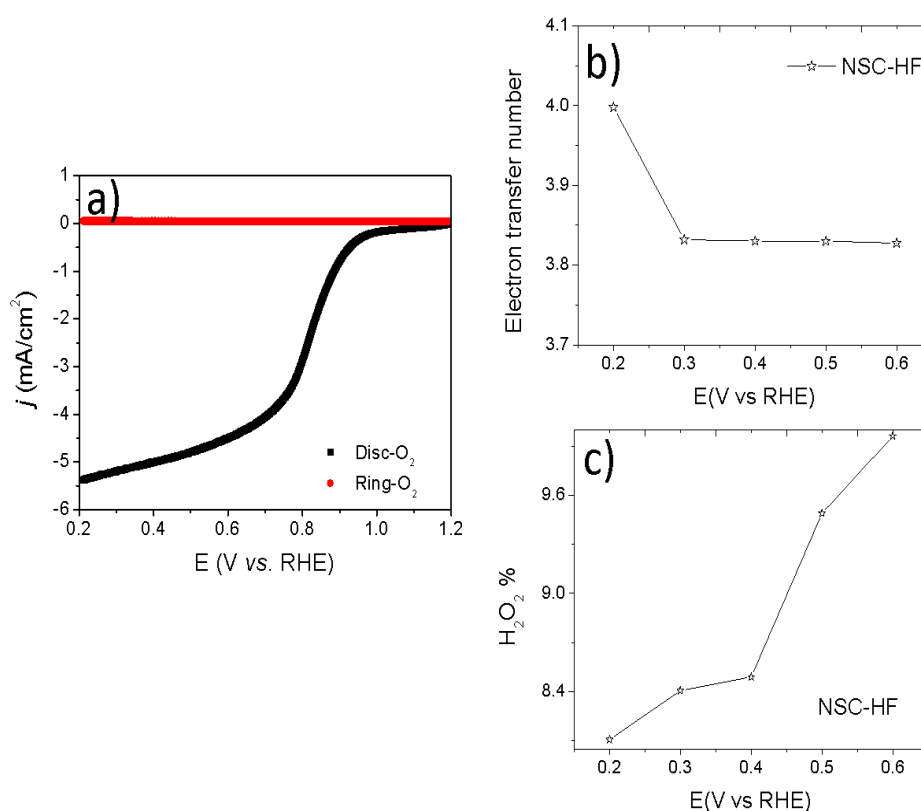
Figure 4.41-a) Linear sweep voltammetry with current collected at ring and disk of NSC-HF, **b)** electron transfer number, and **c)** peroxide production.

Further, the catalyst NSC-HF was subjected to methanol crossover effect analysis, as can be seen in **Figure 4.42-a**. The catalyst showed almost no attenuation in ORR performance, as onset potential and half-wave potential are almost the same, suggesting that the NSC-HF is resistive to the methanol poisoning effect. Long term stability of catalyst material is of great importance for ORR catalysis. The stability test of catalyst NSC-HF and benchmark Pt/C was examined by chronoamperometric current-time (i-t) measurement in oxygen saturated 0.1 M KOH aqueous solution.

The catalyst NSC-HF showed good stability with very little attenuation of 9% for 11 hours, whereas, the Pt/C suffers from a significant loss in current of ~ 20%, during chronoamperometric operation (**Figure 4.42-b**).

The stability of NSC-HF may be due to higher degree of graphitization and higher surface area, on the other side the agglomeration of Pt nanoparticles and faster loss of electrochemical surface area may cause the inferior stability of Pt/C. **[102], [103]**
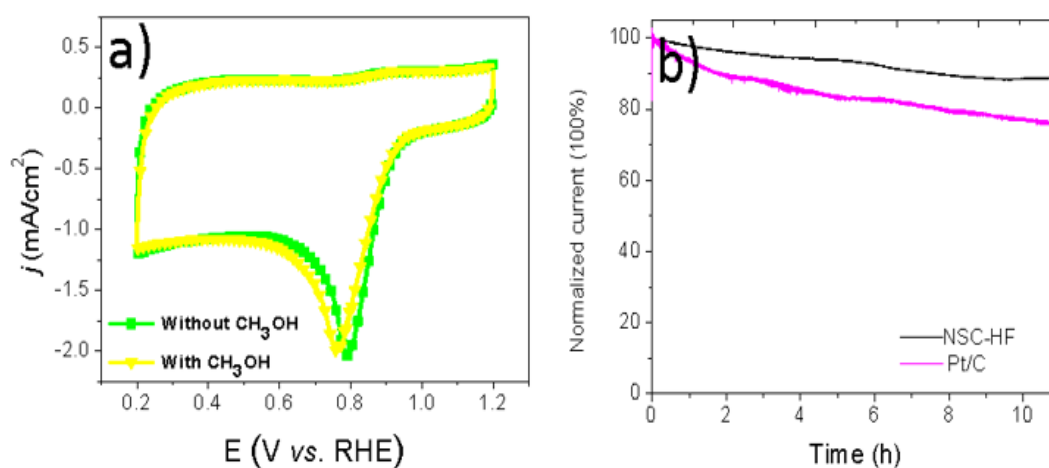
Figure 4.42- a) Methanol crossover test for NSC-HF and **b)** Stability tests for Pt/C and NSC-HF.

4.5 Physical and electrochemical characterizations of nitrogen doped carbon coated silicon dioxide particles and etched nitrogen doped carbon

The SEM image in **Figure 4.43-a** shows the external carbon coating produced after carbonization of PANI coated onto silicon dioxide particles. There are carbon spikes all over the surface. Other SEM image of the same sample revealed a smooth texture of carbon coating onto silicon dioxide particles (**Figure 4.43-b**). The corresponding elemental mapping (**Figure 4.43-a)** identified the presence of nitrogen (6%), silicon (4.3%), oxygen (14.3%) and carbon (75.4%). The elemental mapping of the sample presented in (**Figure 4.43-b**) identified atomic percentages of nitrogen (5.7%), silicon (3%), oxygen (23.2%) and carbon (68.1%). The identification of these elements confirms the successful coating of nitrogen doped carbon onto the silicon dioxide core particles. Sample NC-900 was treated with hydrofluoric acid for removal of silicon dioxide particles. TEM images of sample NC-HF revealed the remaining carbon cups/or shells after etching of silica cores (**Figure 4.44-a, b**).
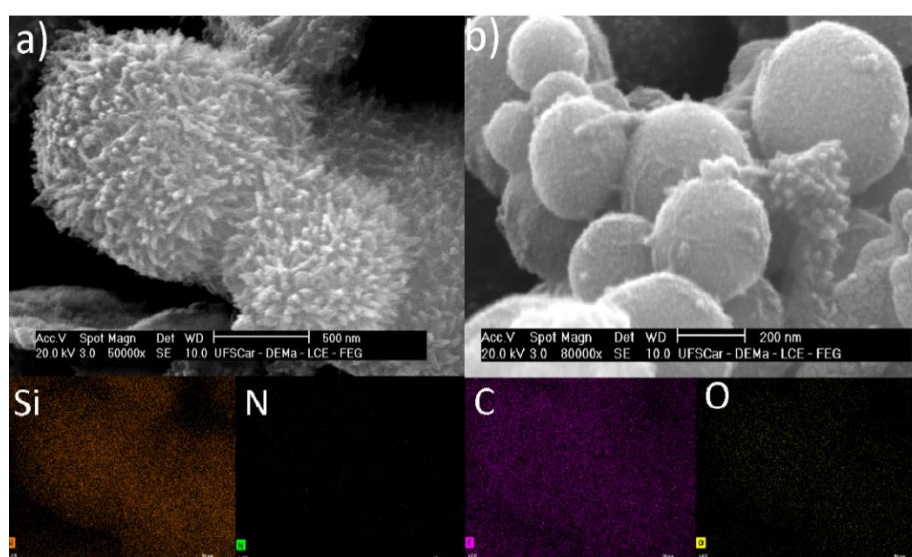
Figure 4.43-a, b) SEM images of NC-900. (In the bottom: element mapping showing the presence of nitrogen, oxygen, carbon, and silicon
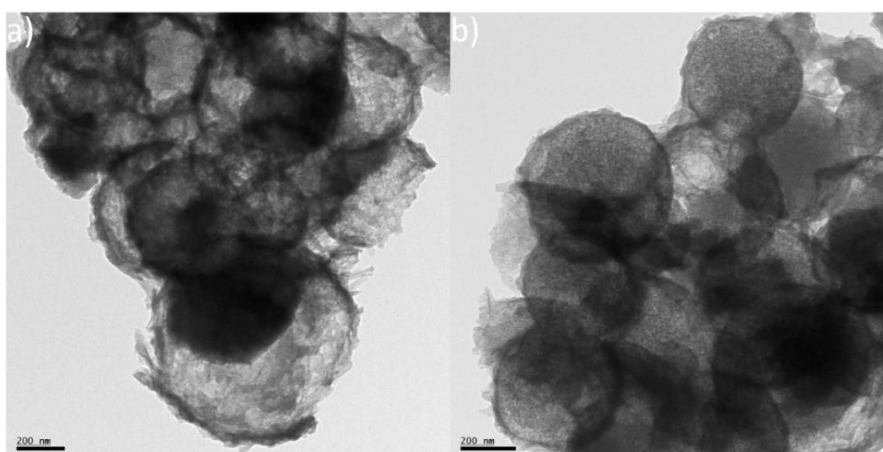
Figure 4.44- a, b) TEM images of NC-HF showing carbon cups.

XRD survey identified a large peak at 22.9° and a less intense peak at and 42.2°, which confirm the successful conversion of PANI into graphitic carbon material with 002 and 001 planes (**Figure 4.45- a**).**[103]** Raman analysis shows the D band at 1365.6 cm^{-1} and G band at 1580 cm^{-1}, attesting to the presence of disordered or amorphous carbon and graphitic carbon. The intensity ratio I_D/I_G was calculated 0.92. (**Figure 4.45- b**). The material was classified as mesoporous with a surface area of 390 m^2/g (**Figure 4.45- c,d**).
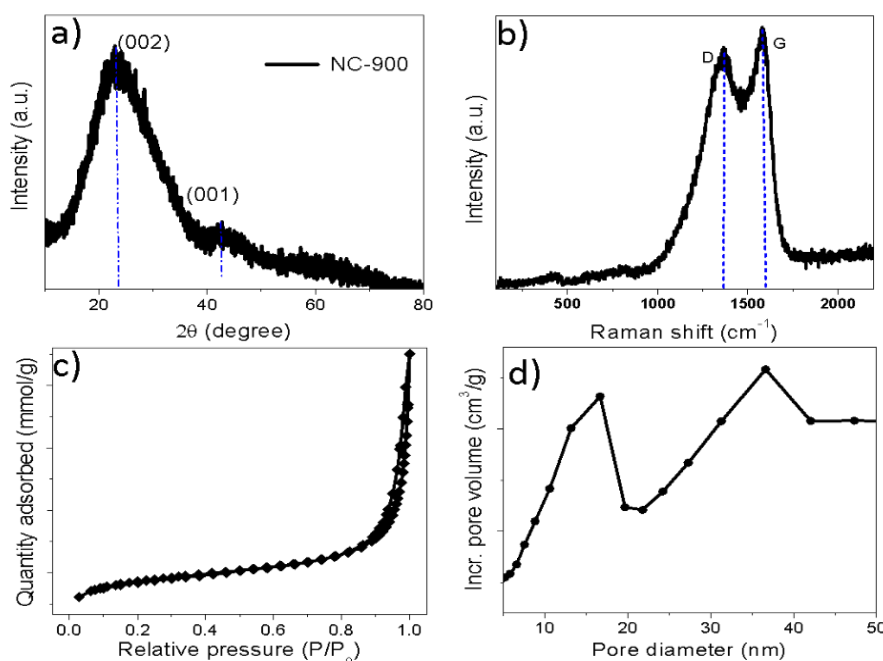
Figure 4.45- a) XRD pattern shows the peak at 22.9° and 42.2°, **b)** Raman shows G-band and D-band, **c)** BET surface area and **d)** pores diameters.

Elements were identified in XPS survey of sample NC-900 (**Figure 4.46**) as nitrogen (6.2%), carbon (86.7%), oxygen (6%) and silicon (1.1%). **Figure 4.46-b)** shows the C1s spectra with C=C (284.5 eV) and C=O (285 eV) bonds. Deconvolution of the XPS N1s spectra shows the presence of quaternary-nitrogen (72%) at 400.8 eV, pyrrolic-nitrogen (23%) at 398 eV, and oxidized-nitrogen (5%) at 405 eV, interesting there was no presence of pyridinic-N.
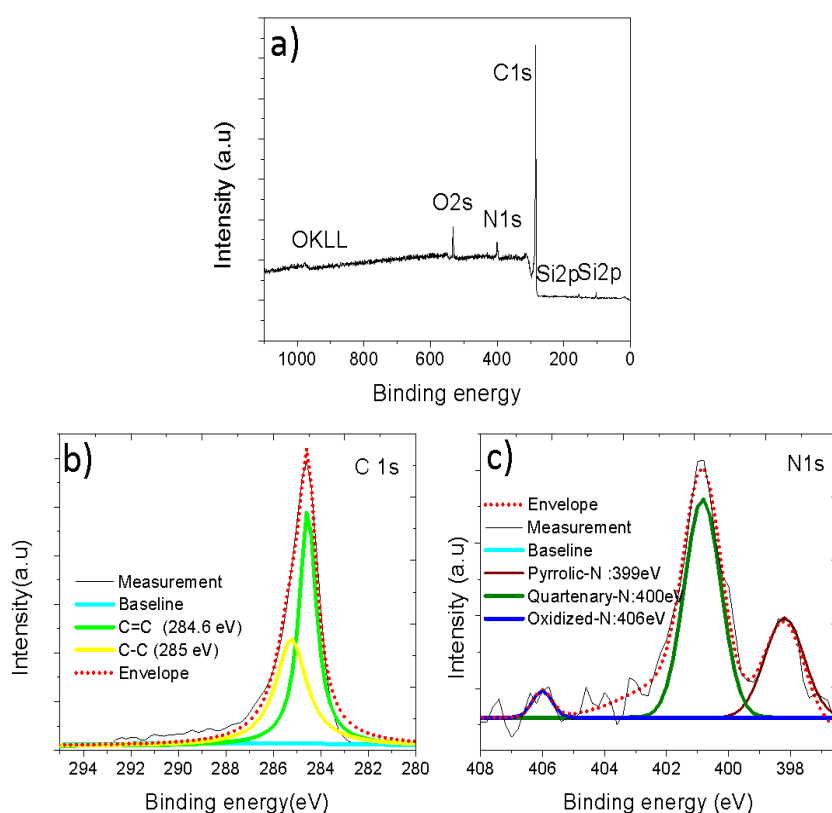
Figure 4.46- a) XPS survey spectra of NC-900, **b)** XPS of C1s, and **c)** XPS of N1s spectra.

CV curve of the sample NC-900 shows oxygen reduction peak at 0.76 V vs RHE in oxygen saturated 0.1 M KOH electrolyte, onset potential at 0.89 V vs RHE and half-wave potential at 0.8V vs RHE (**Figure 4.47-a**).

The LSV curves show the onset potential value near 0.88-0.89 V vs RHE and half-wave potential 0.79 V vs RHE (**Figure 4.47-b** and **Figure 7.2-b** in Appendix). Koutecky -Levich plots of NC-900 is shown in **Figure 4.48-a**. The

electron transfer number values were calculated to each one of the respective potentials and average values found 3.1(0.2 V vs RHE), 3 (0.3 V vs RHE), 3(0.4 V vs RHE) and 3 (0.5 V vs RHE) (**Figure 4.48-b**). Methanol crossover test shows that the sample NC-900 does not decrease performance when methanol was added to the electrolyte **(Figure 4.49-a)**. The chronoamperometry test showed a good stability during 10 h compared with Pt/C catalyst (**Figure 4.49-b**).
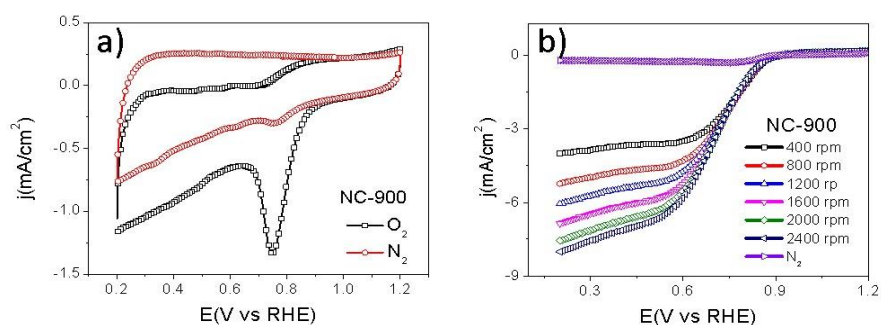
Figure 4.47-a) CV curves of NC-900, and **b)** LSV curves of NC-900.
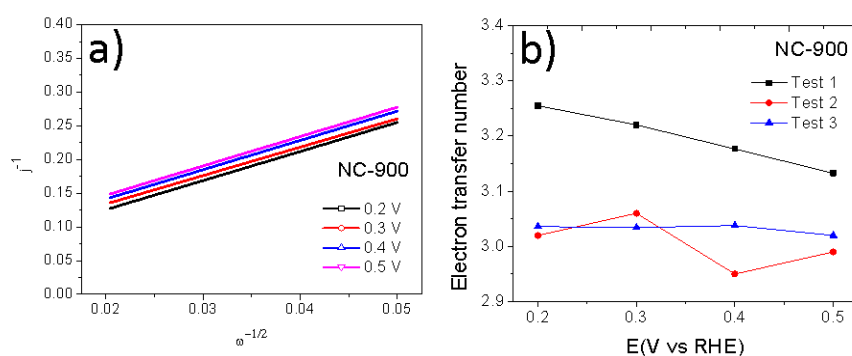
Figure 4.48-a) Koutecky-Levich plot and **b)** Electron transfer number values.
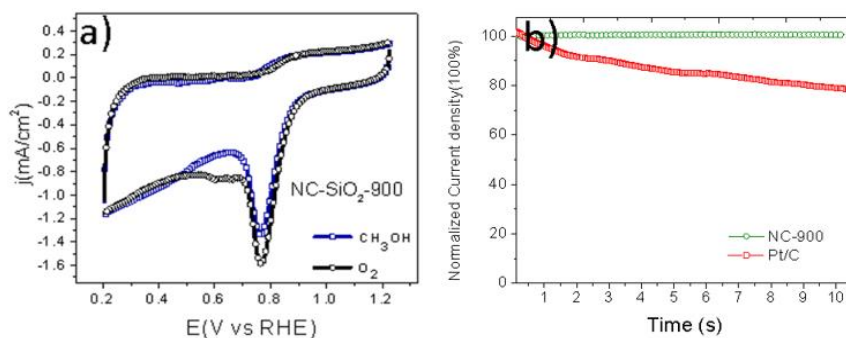
Figure 4.49-a) Methanol cross-over test and **b)** stability test of NC-900.

4.6 Physical and electrochemical characterizations of nitrogen and sulfur co-doped carbon samples

The X-ray diffraction pattern as shown in **Figure 4.50-a**, was used to characterize the graphitic structure of the materials. The samples NSC-HF, NC-HF, and SC-Hf showed two peaks, representing (002) and (001) diffraction plans of graphitic carbon.**[103]**,**[104]** Notably, the diffraction peak at 24.8° for NSC-HF attains a slightly higher degree than those of NC-HF (24.3°) and SC-HF (24.1°), suggesting high π-conjugated system in NSC-HF. **[105]** Moreover, both peaks at 24.8° and 43.2° were also found to be slightly sharper than those of NC-HF and SC-HF, implying a more crystalline feature of the NSC-HF. Raman spectra (**Figure 4.50-b**) shows two bands located at1334 cm^{-1} and 1586 cm^{-1} correspond to the D (structural defects) and G (graphitic order) bands and intensity ratio of D and G peak (I_D/I_G) characterizes the structural disorder of the materials, as it is known that higher the ratio, higher the structural disorder of the material. **[106]**, **[107].** The intensity ratio I_D/I_G was measured to be 0.92, 0.93, and 0.9 for NSC-HF, NC-HF, and SC-HF, respectively. The broader peaks of NSC-HF at 2651 and 2930 cm^{-1} signify the harmonics of 2D and 2G Raman bands, whose intensities reduced for NC-HF and SC-HF, further suggesting the high proportion of graphitic structure of NSC-HF compared to others. The graphitization is essential for enhancing the electrical conductivity of the carbonaceous material, which contributes to the ORR activity of carbon materials **[108]-[110]**.
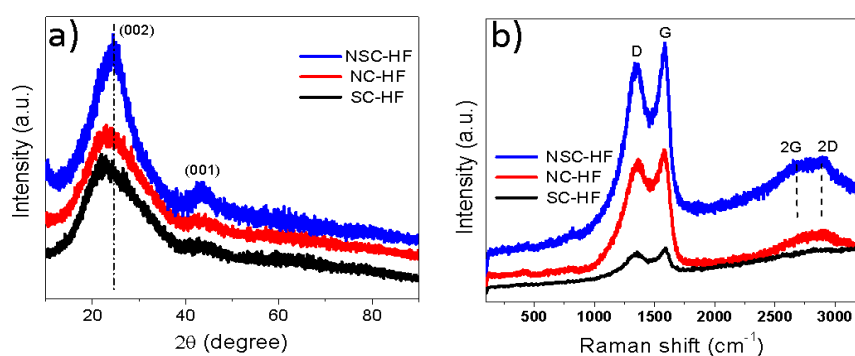
Figure 4.50-a) XRD surveys and **b)** Raman spectra of NC-HF, SC-HF and NSC-HF**.**

Brunauer-Emmett-Teller (BET) specific surface areas were 341, 397, and 180 m²/g for NSC-HF, NC-HF, and SC-HF, respectively. The physisorption isotherm found IV type and shows a clear hysteresis loop, indicating that the samples NSC-HF and NC-HF are mainly composed of mesopores (**Figure 4.51-a**).**[77]**

The corresponding pore size distribution plot derived from the N_2 desorption isotherm, confirms the main mesopores in the NSC-HF and NC-HF with diameters ranging from 1.7 to 50 nm (**Figure 4.51-b**). While, SC-HF shows a constricted and narrow down curve, indicating much narrower pore size distribution. The large surface area and abundant mesopores of sample NSC-HF and NC-HF are viable in accumulating high ion/electron transport for catalysis.
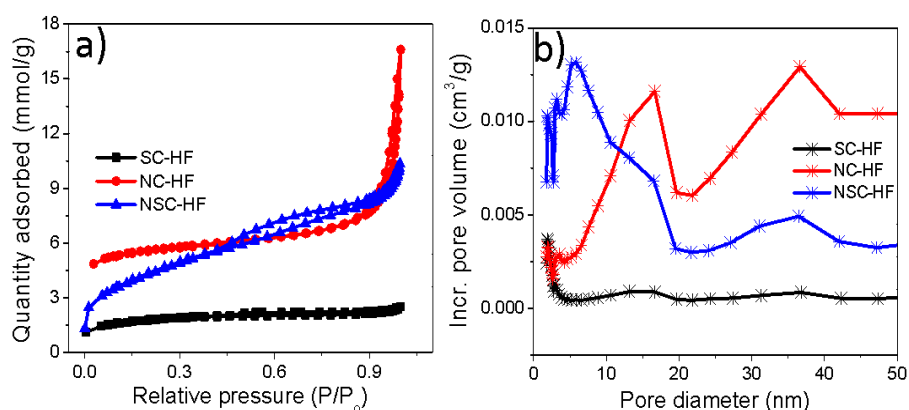
Figure 4.51- a) Nitrogen adsorption-desorption curves (BET) for the NSC-HF and **b)** Pore size distribution curves.

CV curves of the samples NC-900 and NC-HF, SC-900 and SC-HF are shown in **Figure 4.52-a, b**. The samples showed onset potential near to the same values, highlighting that the silicon dioxide particles are inert towards oxygen reduction reaction and do not contribute to enhancing catalytic activity of the doped carbons, however morphological changes are attributed to the process of removal of silica core particles, which may reflect in the catalytic activity.
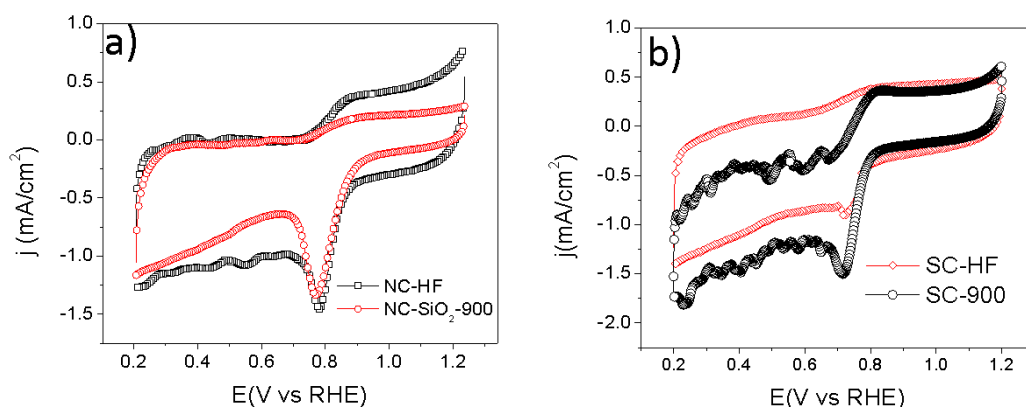
Figure 4.52-a) CV curves of NC-HF and NC-900, and **b)** CV curves of SC-900 and SC-HF.

Figure 4.53-a, b show the CV curves and LSV curves for all etched samples NSC-HF, SC-HF, NC-HF and compared with commercial Pt/C (20 wt.%). It is obvious that the Pt/C catalyst showed the best performance with the most positive onset potential of 1 V vs RHE and half-wave potential of 0.96 V vs RHE. However, the catalyst NSC-HF shows very close performance to the Pt/C by approaching onset potential of about 0.94 V vs RHE, following NC-HF (0.88 V vs RHE) and SC-HF (0.79 V vs RHE). The obtained onset potential value 0.94 V vs RHE is quite impressive compared to the many reported carbon-based ORR electrocatalysts.
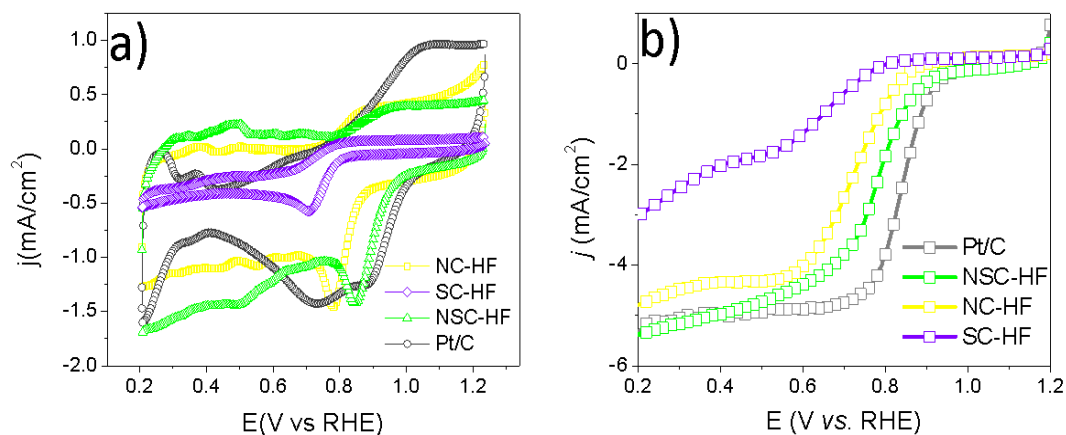
Figure 4.53-a) CV curves and **b)** LSV curves for Pt-based carbon, NSC-HF, NC-HF, and SC-HF.

4.7 Physical and electrochemical characterizations of sulfur and nitrogen co-doped carbon

SEM images (**Figure 4.54-a, b**) of sample SNC-SiO$_2$-900 show the carbon coated silicon dioxide particles. The carbon coating formed pellets with spherical morphology. EDS analysis identified the nitrogen, sulfur, oxygen, carbon and silicon elements, therefore confirming the homogeneously distributed sulfur and nitrogen dopants into the carbon lattice. Atomic percentages were identified as nitrogen (4.35%), sulfur (1.49%), carbon (64.35%), oxygen (24.18%), and silicon (5.62%) (**Figure 4.54-b**).
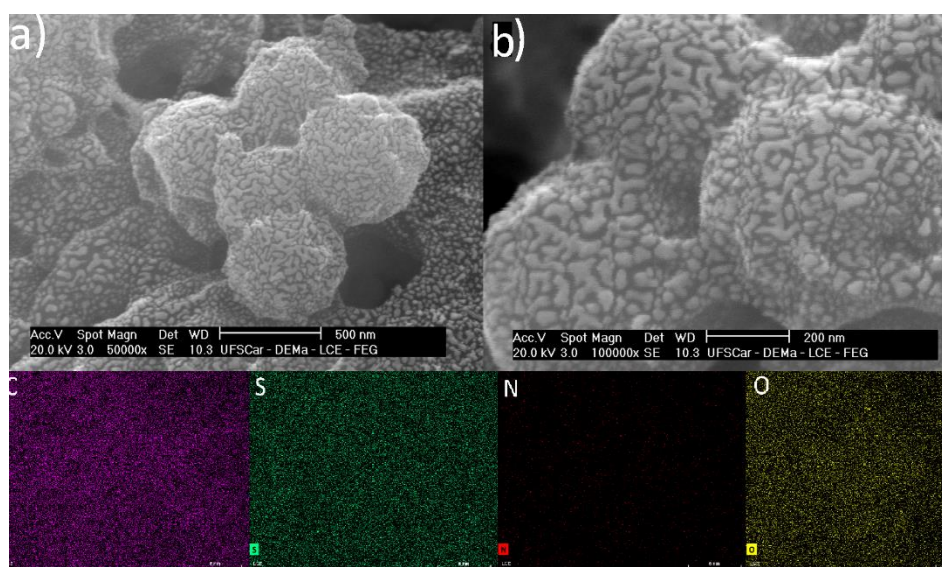
Figure 4.54-a, b) SEM images of SNC-SiO$_2$-900. Bottom of figure: mapping showing the presence of nitrogen, oxygen, carbon, and silicon.

Further, TEM images confirmed the fine coating of co-doped carbon layers onto the silicon dioxide core particles, with few nanometers thickness of carbon layers (**Figure 4.55-a, b, c, d**). It is possible to observe in **Figure 4.55-c**, that two of the silica particle cores were united together by the carbon layers.

Apparently, there is no clear phase separation between sulfur doped carbon and nitrogen doped carbon, instead the carbon layers merge, and by the mapping we identified simultaneous presence of both dopants, which signals co-doping of resulting carbon layers.
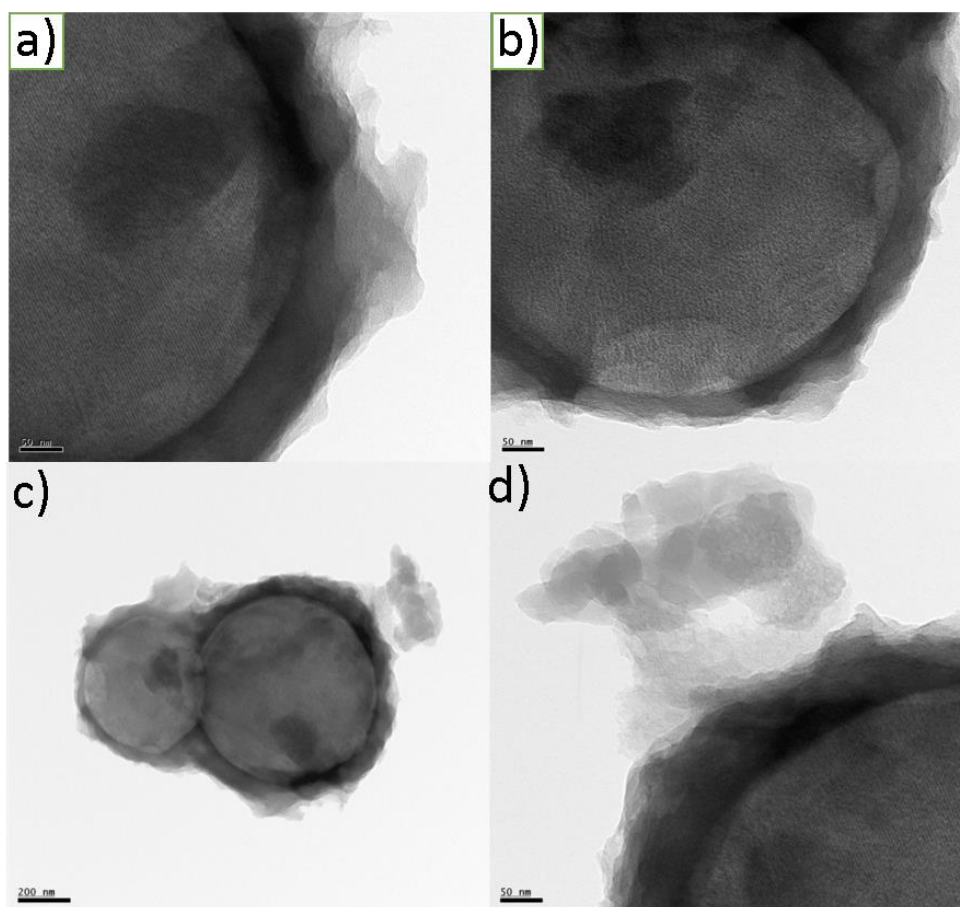
Figure 4.55-a, b, c, d) TEM images of SNC-SiO$_2$-900 shows the sulfur and nitrogen co-doped carbon layer coated over the silica core particles.

Figure 4.56-a, shows the XPS survey spectra of SNC-SiO$_2$-900, which identified 4.2% nitrogen, 58% carbon, 26% oxygen, 8.4% silicon and 3.4% sulfur The O1s XPS spectra shows two peaks corresponding to oxygen bound with carbon (531 eV) and surface adsorbed oxygen (532.5 eV) (**Figure 4.56-b**). In the XPS spectra of N 1s, were assigned 15% pyridinic-nitrogen, 11% pyrrolic and 74% quaternary-nitrogen (**Figure 4.56-d**). **[111]**-**[113]** In the XPS spectra of S 2p, the thiophene-like S-C is assigned to 164.2 eV and S=C to 165.3 eV, and the sulfone-like groups (-C-SO$_x$-) to 168.4 eV and 169.5 eV (**Figure 4.56-c**). The XPS spectra of C 1s shows three peaks, assigning 38.78% C=C (284.4 eV), 40% C=O/C-N/C-S (286.8 eV), and 21.22% C-O/C=O (292.3 eV) **Figure 4.56-e. [114]**-**[115]**
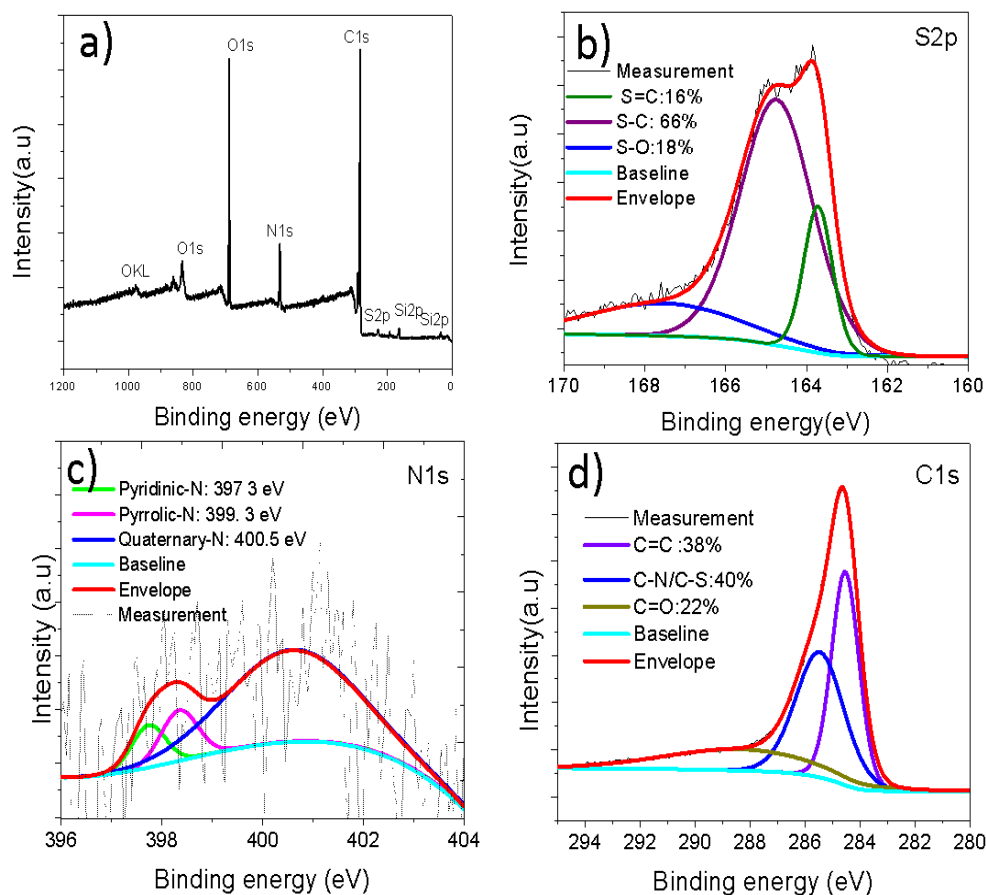
Figure 4.56 - a) XPS survey of SNC-SiO₂-900, **b)** XPS spectra of C 1s, **c)** XPS spectra of O 1s, **d)** XPS spectra of N 1s, and **e)** XPS spectra of S 2p of SNC-SiO₂-900.

CV and LSV curves of sample SNC-SiO₂-900 (**Figure 4.57-a, b**) present onset potential of 0.89V vs RHE and half-wave potential at 0.81 V vs RHE. **Figure 4.57-b** shows the LSV curves reaching higher current density with higher rotation speed (supplementary curve in **Figure 7.4-a** in Appendix). **Figure 4.58-a, b** show the corresponding Koutecky-Levich plot and electron transfer number values obtained at different potentials.
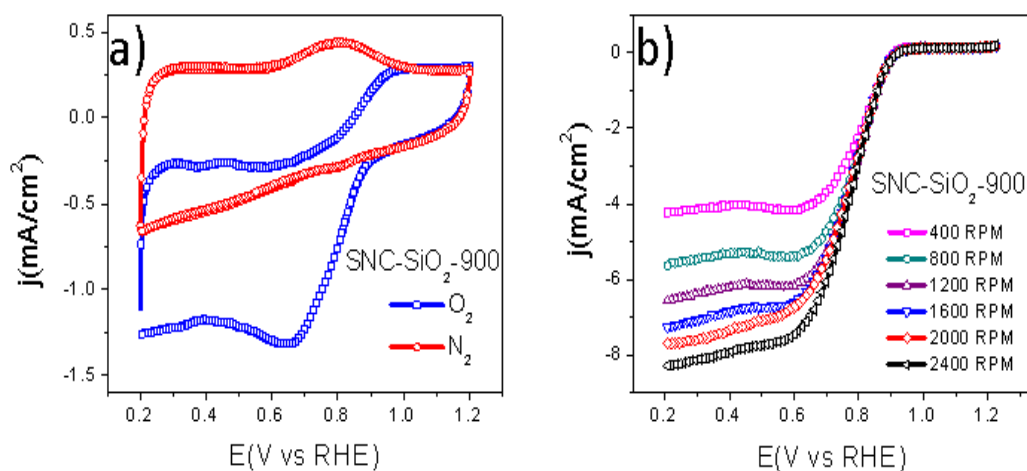
Figure 4.57-a) CV of SNC-SiO₂-900, and **b)** LSV of SNC-SiO₂-900.
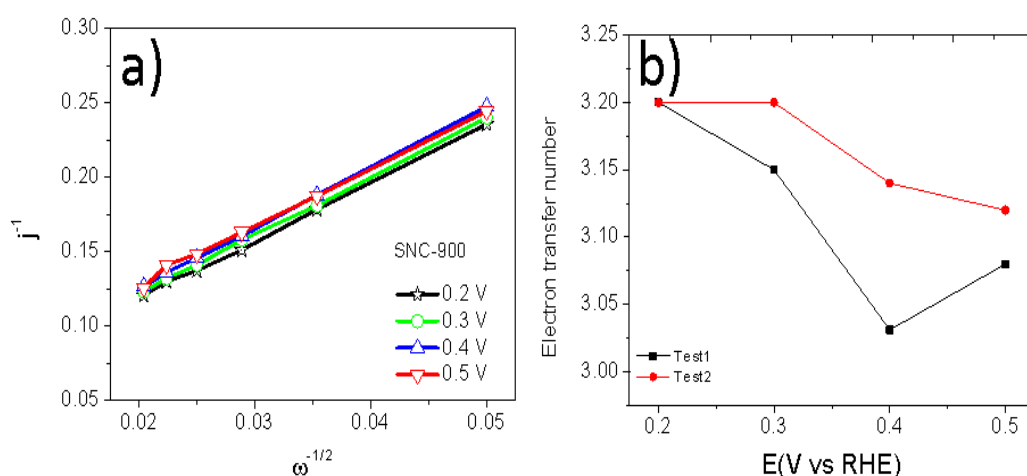
Figure 4.58-a) Koutecky-Levich plot of SNC-SiO₂-900, and **b)** corresponding electron transfer of SNC-SiO₂-900.

In the next step, SNC-SiO₂-900 was treated with hydrofluoric acid for removal of the silica ore particles, resulting in the sample SNC-HF.

TEM images of the sample SNC-HF showed that after the treatment with hydrofluoric acid for removal of silica core particles, the sample was constituted by the fragments of carbon material (**Figure 4.59-a,b**,**4.60-a,b**).
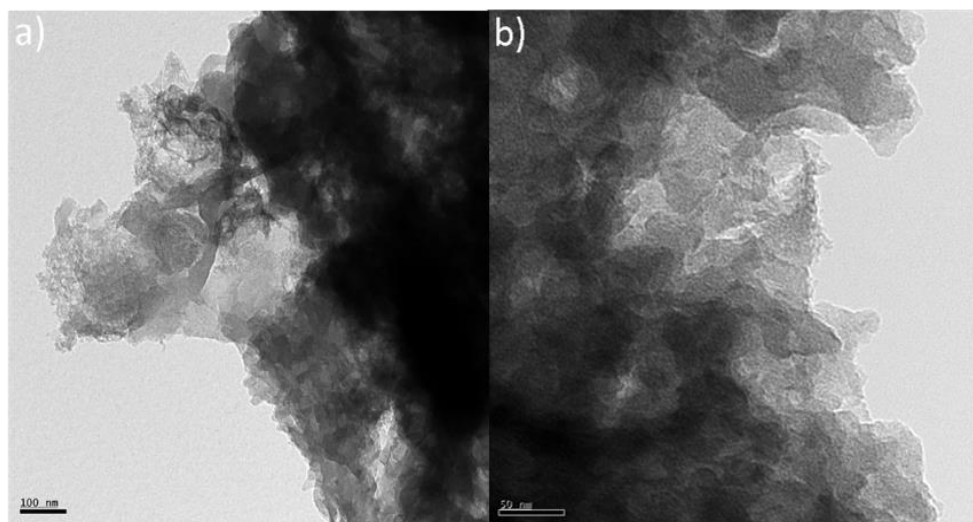
Figure 4.59-a,b) TEM images of SNC-HF.
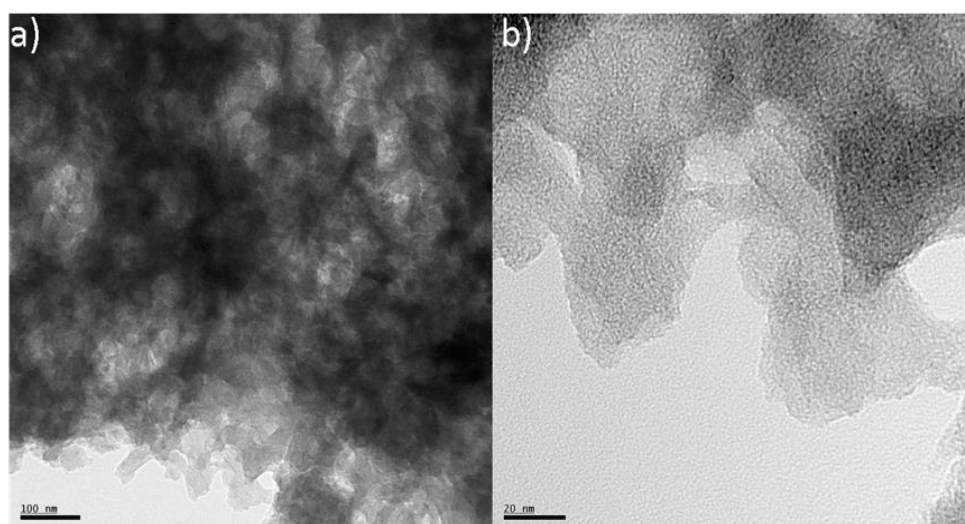
Figure 4.60-a,b) TEM images of SNC-HF.

XPS analysis of sample SNC-HF as shown in **Figure 4.61-a** identified the presence of 87% carbon, 6.1% oxygen, 2.9% nitrogen, and 4 % sulfur. The O1s XPS spectra (**Figure 4.61-b**) showed two peaks corresponding to oxygen bound with carbon (531.1 eV) and surface adsorbed oxygen (533 eV). **Figure 4.61-c** shows the XPS S2p spectra of sulfur species doped into carbon lattice as thiophenic-like C-S/C=S (63%) and oxidized-sulfur (37%). The atomic percentage of the nitrogen species were 11.8% pyrrolic, 68.5% quaternary and 19.7% oxidized (**Figure 4.61-d**). The XPS spectra of C 1s shows three peaks,

assigning 48.2% C=C (283.9 eV), 38.8% C-N/C-S (285 eV), and 13% C-O/C=O (291.8 eV) (**Figure 4.61-e**).
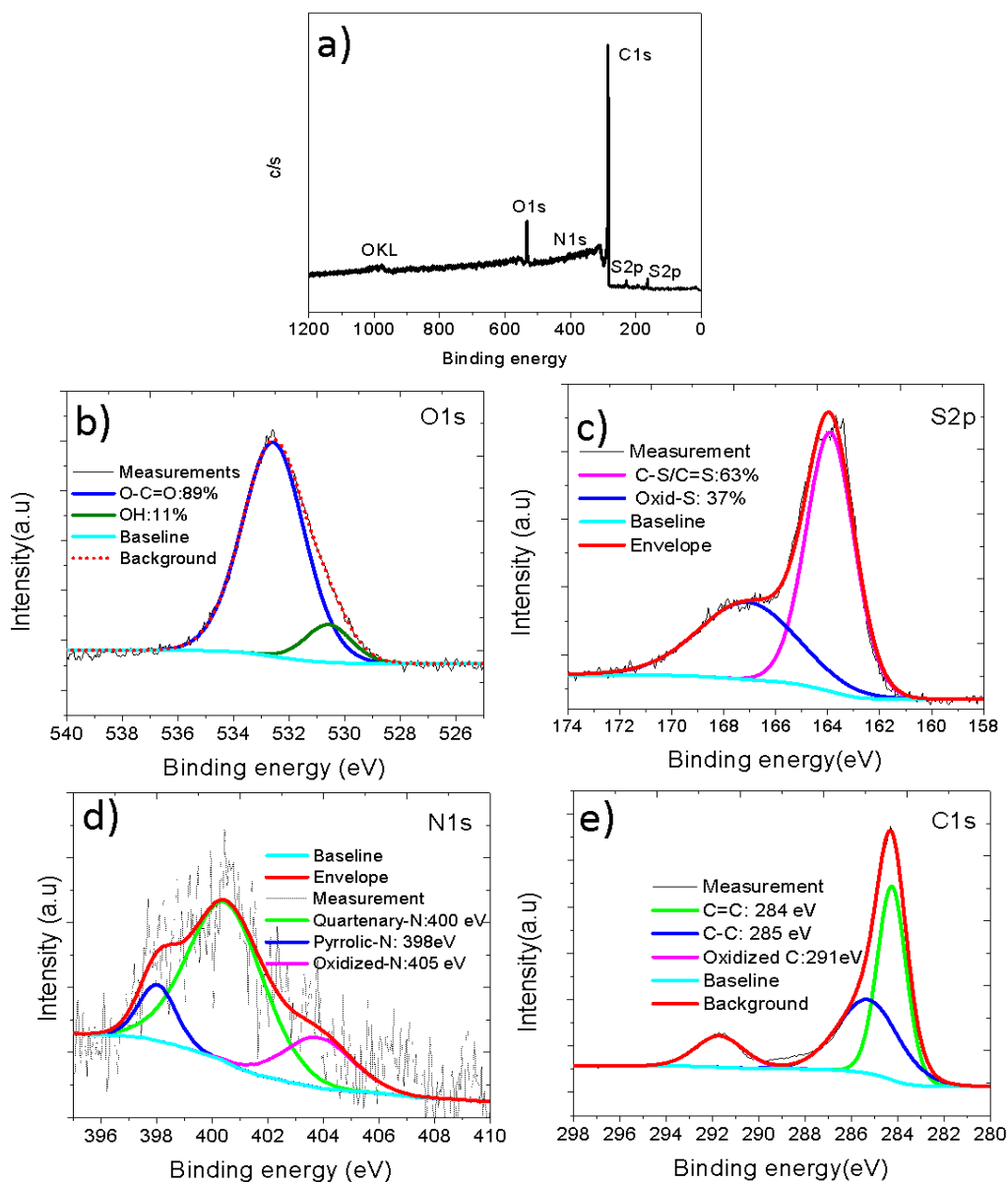
Figure 4.61-a) XPS survey of SNC-HF, **b)** XPS spectra of C 1s, **c)** XPS spectra of O 1s, **d)** XPS spectra of N 1s, and **e)** XPS spectra of S 2p.

CV curves of sample SNC-HF (**Figure 4.62-a**) showed onset potential value near 0.91-0.92 V vs RHE. LSV curves (**Figure 4.62-a** and **Figure 7.4 -b** in Appendix) show that the current density curves reach higher values as the rotational speed is increased.

Figure 4.63- a, b show the corresponding Koutecky-Levich plot and electron transfer number values calculated to each potential. The electron transfer number values were calculated with base on the three tests as 3.48(0.2 V vs RHE), 3.46(0.3 V vs RHE),3.45 (0.4 V vs RHE), and 3.42(0.5 V vs RHE). **Figure 4.64-a** shows good methanol crossover effect of sample SNC-HF. The chronoamperometric test of sample SNC-HF is presented in **Figure 4.64-b** indicating good stability.
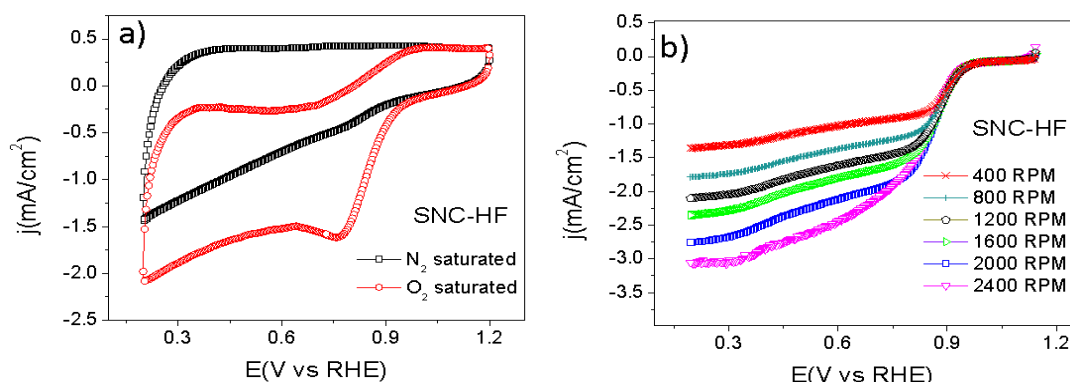
Figure 4.62-a) CV curves of SNC-HF, and **b)** LSV curves of SNC-HF.
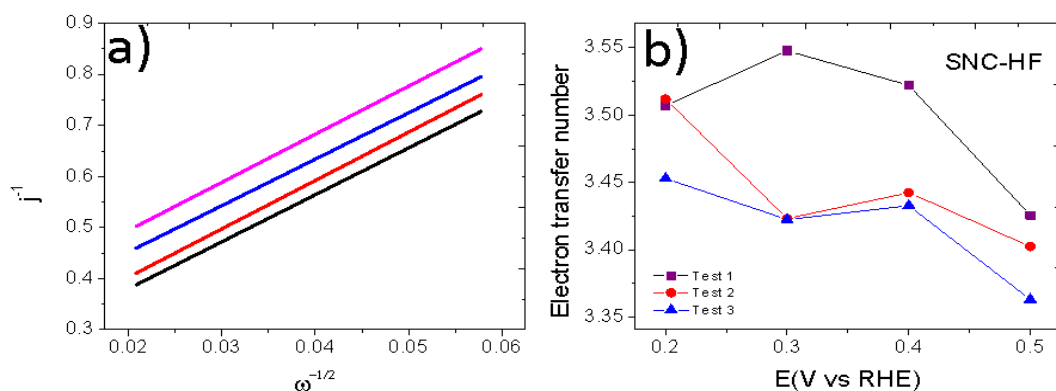
Figure 4.63-a) Koutecky-Levich plot of SNC-HF, and **b)** corresponding electron transfer number of samples SNC-HF.
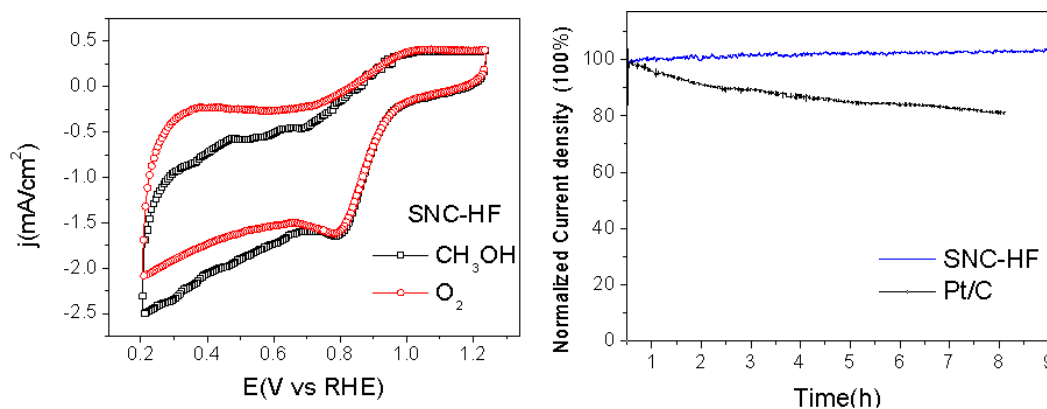
Figure 4.64-a) Methanol crossover of SNC-HF, and **b)** Stability test of SNC-HF.

Samples SNC-HF and NSC-HF were prepared from the same polymer precursors (PANI and PEDOT) in alternated ways, which explain why the samples activity is different. The sample NSC-HF performs slightly better in terms of onset potential (0.94 V vs RHE) and half wave potential (0.87V vs RHE) than the sample SNC-HF (onset potential: 0.92 V vs RHE and half-wave potential: 0.84 V vs RHE). This indicates that the external layer of nitrogen doped carbon (produced by carbonization of PANI) shows better catalytic properties than the external layer of sulfur doped carbon (produced by carbonization of PEDOT). The synergistic factor of co-doping and structure resulting from the etching treatment can also be considered for the high ORR performance of sulfur and nitrogen doped carbon NSC-HF.

4.8 Physical and electrochemical characterizations sulfur doped carbon coated silicon dioxide nanoparticles

SEM images of sample SC-SiO$_2$-PTH-900 (**Figure 4.65-a**) presents the sulfur doped carbon coated onto silicon dioxide particles, and the mapping shows the elemental composition. The carbon layer coated silicon dioxide particles showed average diameters between 250 - 500nm. The elemental mapping showed that sulfur-doped carbon coated silicon dioxide particles were successfully prepared, as can be observed in the homogeneous distribution of carbon and sulfur doping. The atomic content was identified as follows, carbon

(49.82%), oxygen (37.72%), silicon (12.21%), and sulfur (0.25%) (**Figure**s **4.65-b**).
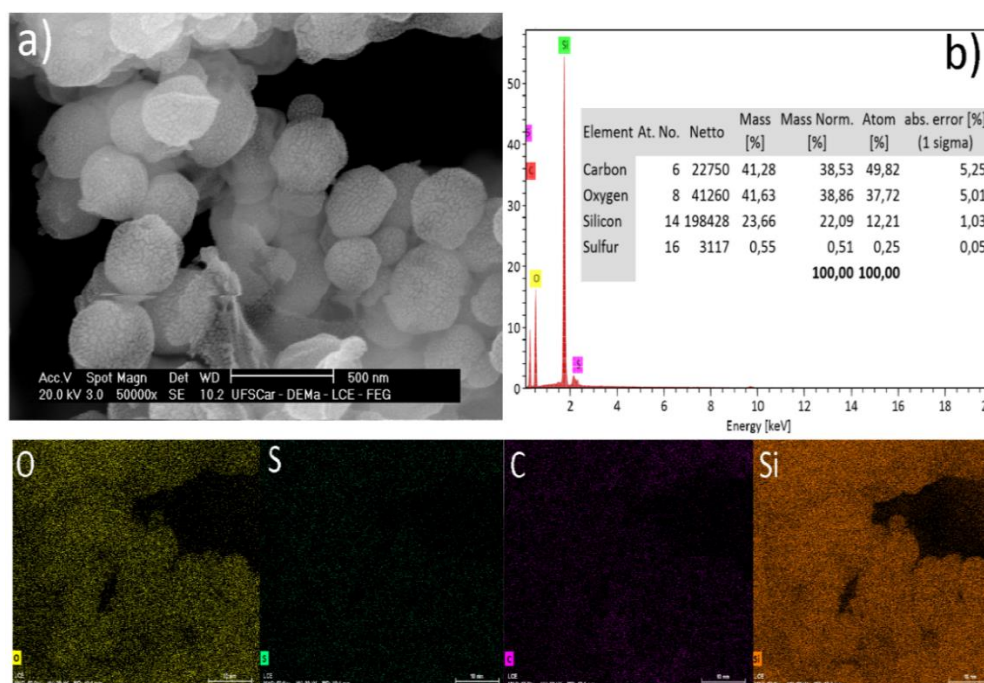
Figure 4.65-a) SEM image of SC-SiO$_2$-PTH-900, and **b)** corresponding mapping of O, S, C and Si

Electrochemical tests were performed in alkaline solution (0.1 M KOH), purged successively with nitrogen and oxygen. CV curve of the sample SC-SiO$_2$-PTH-900 (**Figure 4.66-a**) shows cathodic peak for the oxygen reduction at 0.75 V vs RHE and current density near to 0.6 mA/cm^2. **Figure 4.66-b** shows the LSV curves with onset potential of ~ 0.79 V vs RHE. The Koutecky-Levich plot is presented in **Figure 4.67-a**. The electron transfer number values to each potential were calculated 2.3 (0.2V), 2.27 (0.3V), 2.26 (0.4V), 2.18 (0.5V), and 2.1 (0.6V) (**Figure 4.67-b**). The relatively low electron transfer number indicating two electron pathways for ORR for the SC-SiO$_2$-PTH-900.

Methanol cross over test for the SC-SiO$_2$-PTH-900, as shown in **Figure 4.68-a** shows slightly reduced performance in terms of current density, this might be due to the methanol molecules blocking the active sites of SC-SiO$_2$-PTH-900.

Electrochemical properties of sulfur doped carbon prepared from two different precursor sources such as PTH and PEDOT were also investigated. As shown in **Figure 4.68-b,** the CV curves for the SC-900 (prepared from PEDOT coated silicon dioxide particles) exhibited better ORR performance by achieving higher current density value in the CV ($1.5 mA.cm^2$) and more positive of onset potential value (0.8V vs RHE) than that of the sulfur doped carbon prepared from the carbonization of PTH (0.78V vs RHE and current density value of 0.6 $mA.cm^2$).

This might be because the contents of sulfur in the carbon material prepared from PEDOT were 3.8%, much higher than the carbon material prepared from PTH (0.25%). In addition, the sulfur doped carbon material prepared from PEDOT had a surface area of 180 m^2/g, while sulfur doped carbon prepared from PTH was 56 m^2/g.
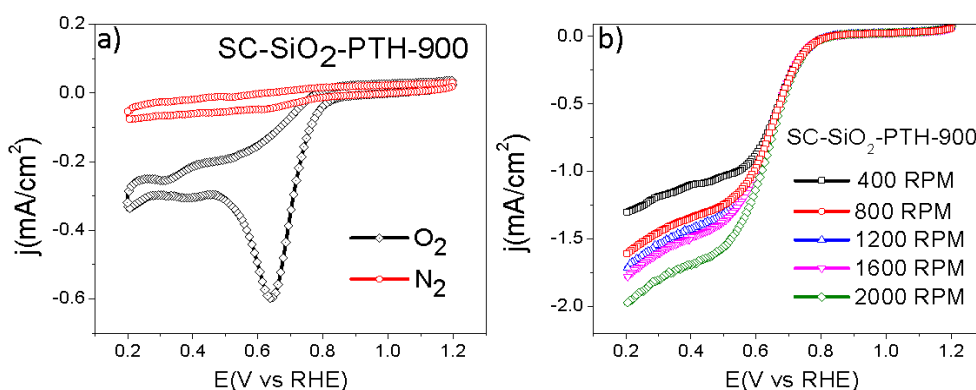
Figure 4.66-a) CV curves and **b)** LSV curves of SC- SiO_2 -PTH-900.
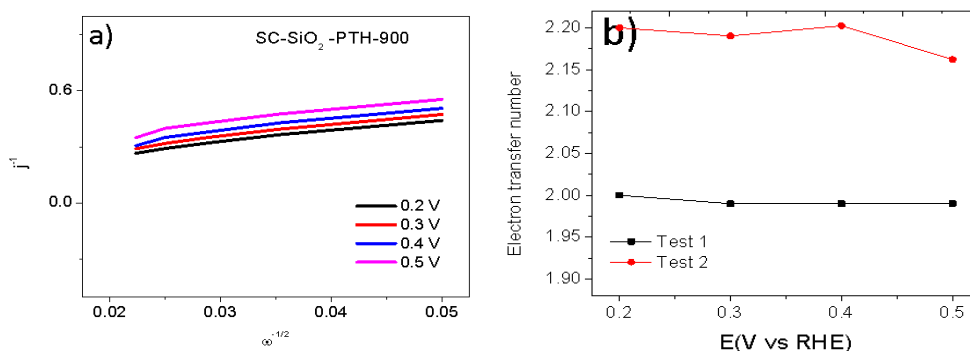
Figure 4.67-a) Koutecky-Levich curves of SC-SiO_2-PTH-900, and **b)** electron transfer number values of SC-SiO_2-PTH-900.
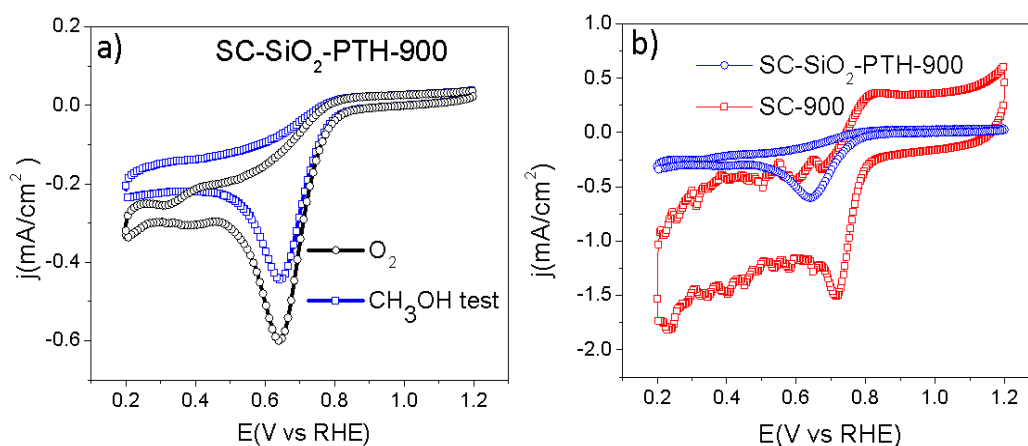
Figure 4.68-a) Resistance to methanol poisoning test of SC-SiO$_2$-PTH-900, **b)** CV curves comparison of sulfur doped carbon derived from PTH (SC-SiO$_2$-PTH-900) and PEDOT (SC-900).

4.9 Physical and electrochemical characterizations of nitrogen and sulfur co-doped carbon

SEM image of **Figure 4.69-a** shows that the sample NSC-PANI-PTH-SiO$_2$-900 demonstrated spike-like structures all over the external surface of the carbon sphere. The corresponding EDS analysis showed the homogeneous distribution of elements oxygen, silicon, carbon, nitrogen and sulfur elements. The atomic percentages were identified: 82.38% carbon, 8.54% oxygen, 0.49% silicon, 8.5% nitrogen, and 0.06% sulfur, respectively (**Figure 4.69-b**). The small percentage of sulfur might be explained by the loss of sulfur content during carbonization of polythiophene.
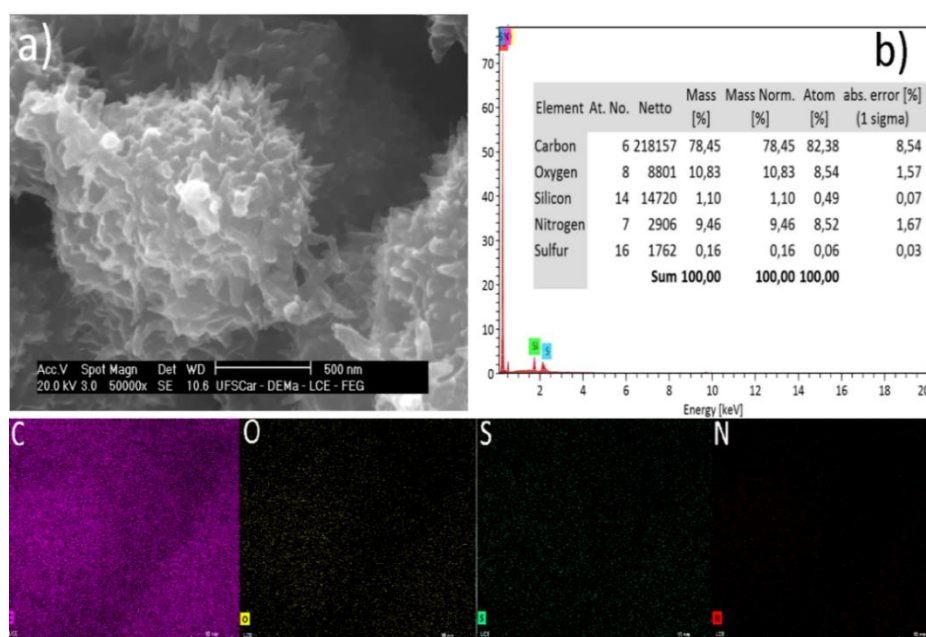
Figure 4.69-a) SEM of NSC-PANI-PTH-SiO₂-900, **b)** Corresponding elemental composition of NSC-PANI-PTH-SiO₂-900 and mapping showing the presence of the dopant elements (bottom).

TEM images (**Figures 4.70-a,b**) of etched sample NSC(PANI-PTH-HF), showed the agglomerated pieces of carbon. The hydrofluoric acid treatment completely removed the silicon dioxide particles, while destroying the structure. Furthermore, it is also important to note that there is no visible phase boundary from two different sources of carbon (PANI and PTH). XPS analysis of the etched sample revealed sulfur and nitrogen presence (**Figure 4.71-a**).
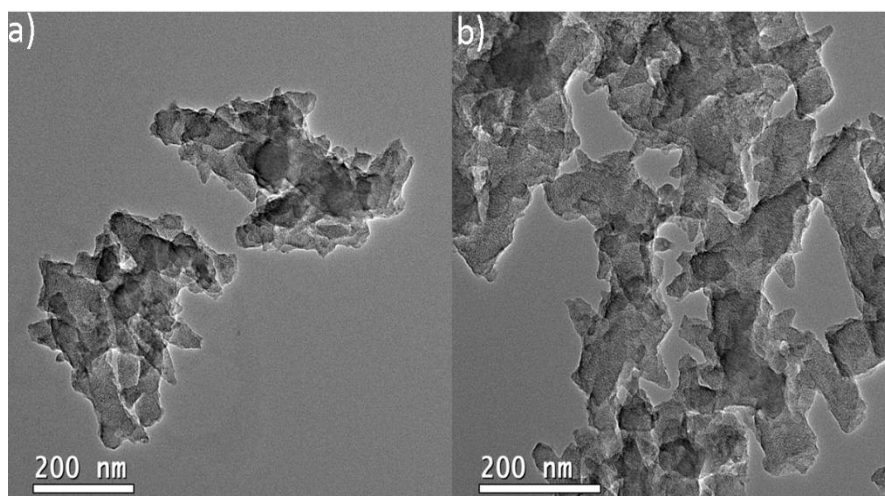
Figure 4.70-a, b) TEM images of NSC (PANI-PTH-HF).

Figure 4.71-a shows the XPS survey spectra of NSC (PANI-PTH-HF) containing nitrogen (2,6%), sulfur (0.9%), oxygen (16.9%) and carbon (79.6%). In the XPS spectra of C 1s, it was found C=C/C-C (57.87%), C-N/C-S (31.60%), and -C=O, (10.53%) (**Figure 4.71-b**). XPS spectra of N 1s (**Figure 4.71-c**) can be deconvoluted for quaternary-nitrogen (51.49%), pyrrolic-nitrogen (24.93%), and oxidized-nitrogen (23.58%). The XPS spectra of S 2p shows sulfide bridges (C=S, 43.78%), (C-S, 27.17%), and oxidized species (O=S, 29.05%) (**Figure 4.71-d**).

Figure 4.72-a presents XRD diffraction pattern with typical peaks at 24° and 45° of carbon materials. In **Figure 4.72-b**, Raman spectra shows D band and G band. The intensity ratio I_D/I_G of 1.1 of the sample NSC (PANI-PTH-HF) represents highly disordered carbon. Measurements of surface area and porosity using BET were performed for the samples NSC, NSC-PANI-PTH-SiO$_2$-900 and NSC-PANI-PTH-SiO$_2$-100.

The measured surface areas were 379 m^2/g for the sample NSC (PANI-PTH-HF), 221 m^2/g for NSC-PANI-PTH-SiO$_2$-900 and 203 m^2/g for NSC-PANI-PTH-SiO$_2$-1000 (**Figure 4.73-a**). The fact that the etched sample presented the larger surface area, highlights the positive effect of removal of silicon dioxide particles, which can facilitate larger exposure of active sites for catalysis. The catalysts also show the rich mesoporosity, which is essential for mass transport (**Figure 4.73-b**).
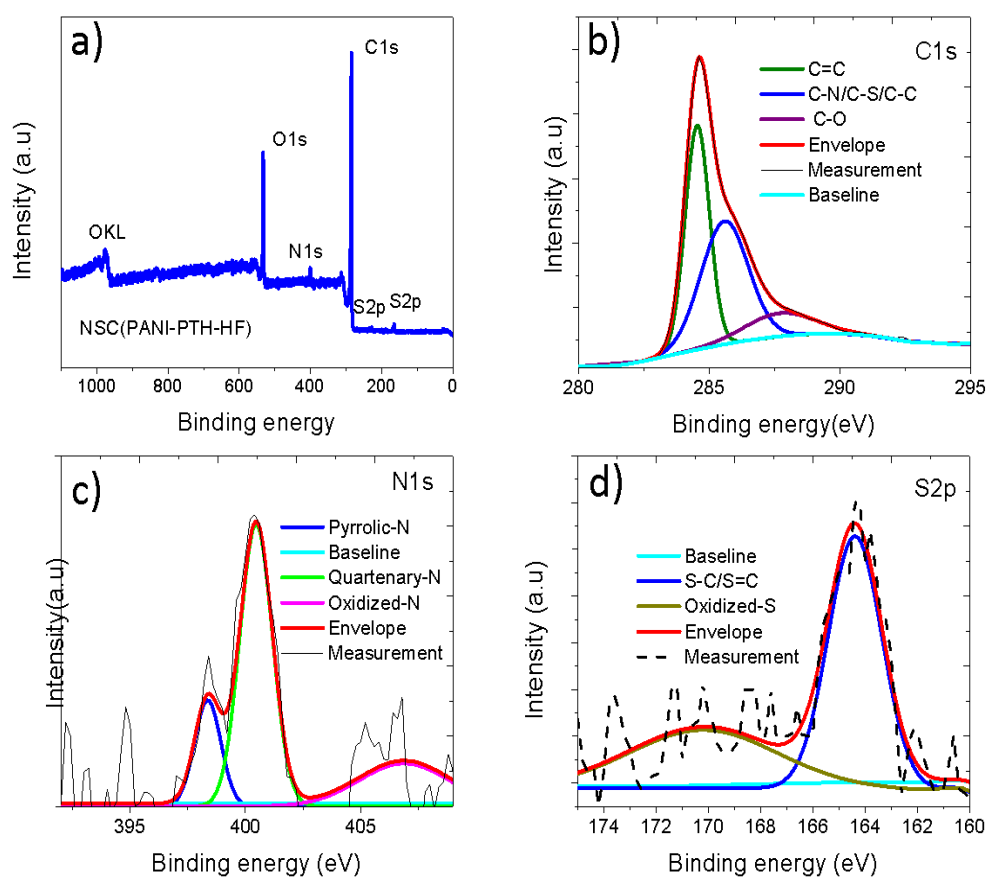
Figure 4.71-a) XPS Composition of NSC(PANI-PTH-HF), b) XPS spectra of C1s, XPS spectra of N1s, and XPS spectra of S2p.
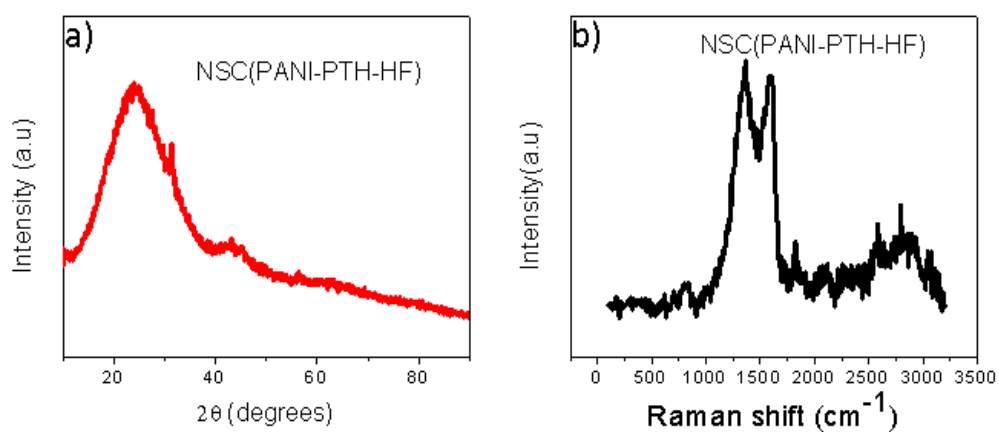
Figure 4.72-a) X-ray pattern of NSC(PANI-PTH-HF), and **b)** Raman characterization of NSC(PANI-PTH-SI).
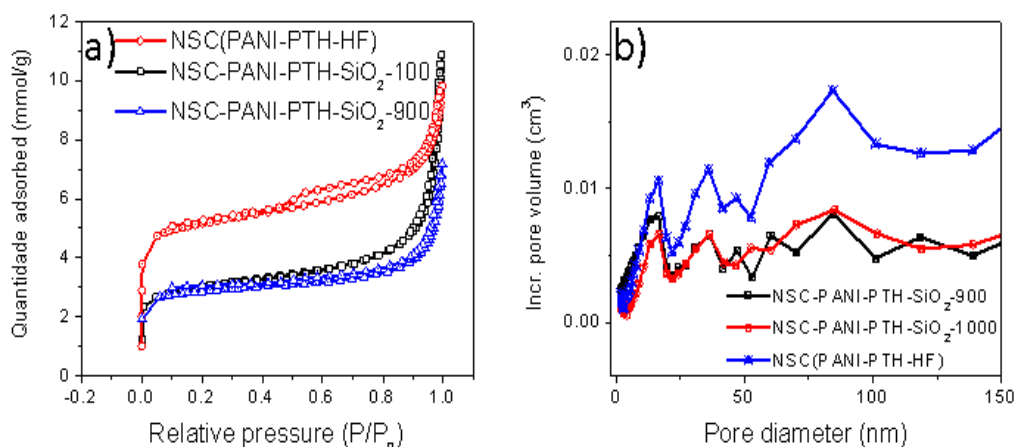
Figure 4.73-a) Nitrogen adsorption-desorption isotherm for NSC, NSC-PANI-PTH-SiO$_2$-900 and NSC-PANI-PTH-SiO$_2$-1000, **b)** Pore size distribution of NSC(PANI-PTH-HF), NSC-PANI-PTH-SiO$_2$-900 and NSC-PANI-PTH-SiO$_2$-1000.

CV and LSV curves of the sample NSC-PANI-PTH-SiO$_2$-900 shows oxygen reduction peak at 0.75 V vs RHE at 1.2 mA/cm^2 and onset potential at 0.87 V vs RHE (**Figure 4.74-a, b**). **Figure 4.75-a** shows the Koutecky-Levich plot with linear curves at different potentials. The electron transfer number values are plotted in relation to the potential values (**Figure 4.75-b**) and vary between 2.9 (0.2V vs RHE) and 2.5(0.5 V vs RHE).

Resistance to methanol poisoning test was performed by the addition of methanol in the alkaline solution, as shown in the **Figure 4.76-a**. There was a little loss in performance noticed by reducing current density, and half wave potential. However, there was no obvious change of onset potential. The stability test (**Figure 4.76-b**) shows good stability, the catalyst kept 100% of the normalized current for 40000 seconds of chronoamperometric operation.
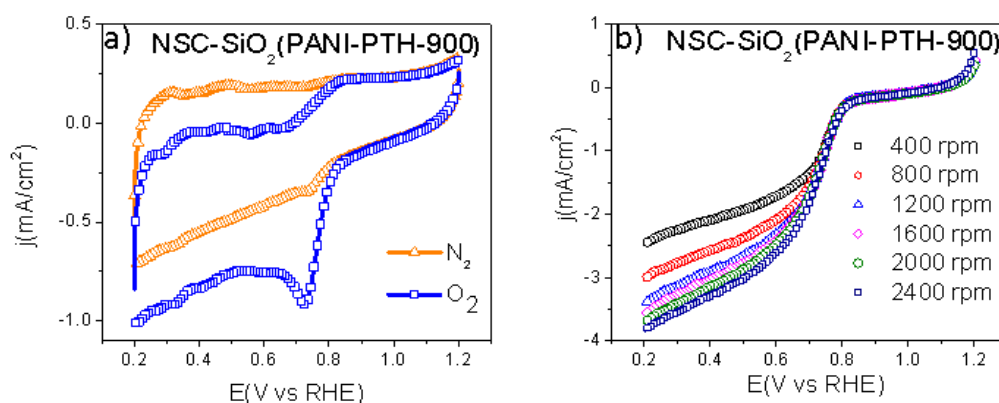
Figure 4.74-a) CV curves of NSC-SiO2(PANI-PTH-900), and **b)** LSV curves of NSC-SiO2 (PANI-PTH-900).
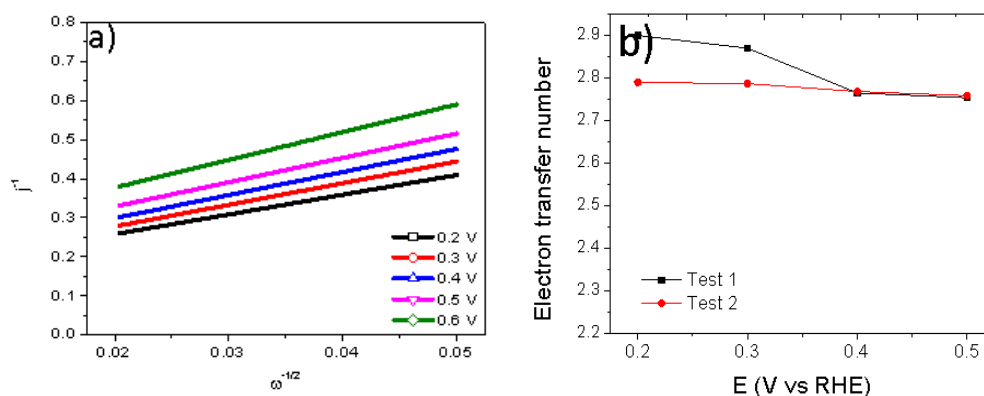
Figure 4.75-a) Koutecky-Levich plot of NSC (PANI-PTH), and **b)** corresponding electron transfer number values of NSC (PANI-PTH).
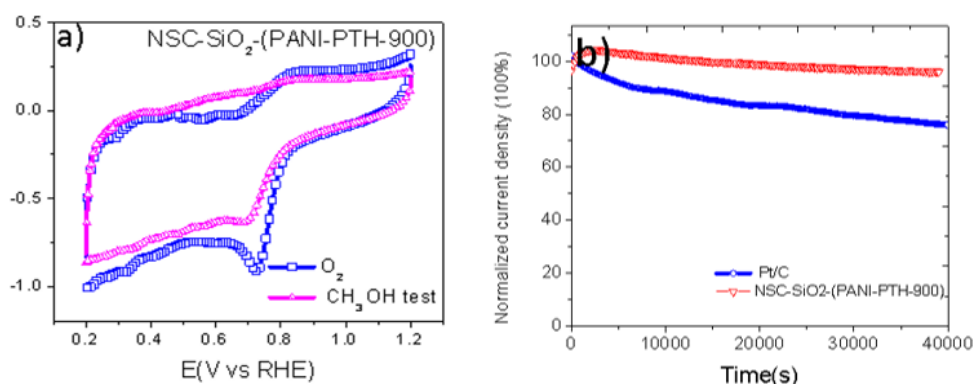
Figure 4.76-a) Methanol cross-over test of NSC-SiO2-(PANI-PTH-900), and **b)** Stability test.

Figure 4.77-a,b show the comparison of CV and LSV curves for samples SC-SiO$_2$-PTH-900 and NSC-SiO$_2$-(PANI-PTH-900), respectively. NSC-PANI-PTH-SiO$_2$-900 presented onset potential of 0.87 V vs RHE and current density of 1.55 mA/cm^2 much better than SC-SiO$_2$-PTH-900 (0.79 V vs RHE and current density of 0.6 mA/cm^2)

CV of the sample NSC-PANI-PTH-SiO$_2$-1000 in **Figure 4.78-a** shows onset potential value of ~ 0.87 V vs RHE, and peak potential of 1.36 mA/cm^2 at 0.72 V vs RHE. **Figure 4.78-b** shows the LSV with higher value of 4.3 mA/cm^2 at a rotating speed of 2400 rpm. **Figure 4.79-a** shows the Koutecky-Levich plot with linear curves at different potentials. The electron transfer number values are plotted in relation to the potential values (**Figure 4.79-b**) and average value found to be ~ 2.8. NSC-PANI-PTH-SiO$_2$-1000 also shows acceptable resistance toward methanol poisoning cross over effect, as shown in **Figure 4.80-a**. The stability test of sample NSC-PANI-PTH-SiO$_2$-1000 (**Figure 4.80-b**) shows the current loss of about 20% after 11hours.
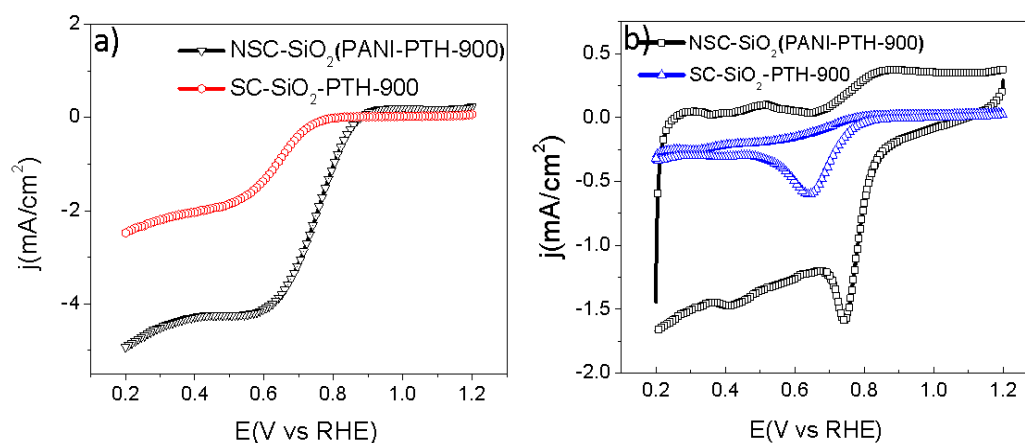
Figure 4.77-a) Comparison of CV of samples SC-SiO$_2$-PTH-900 and NSC-SiO$_2$-(PANI-PTH-900), and **b)** LSV of samples SC(PTH-900) and NSC-SiO2-(PANI-PTH-900).
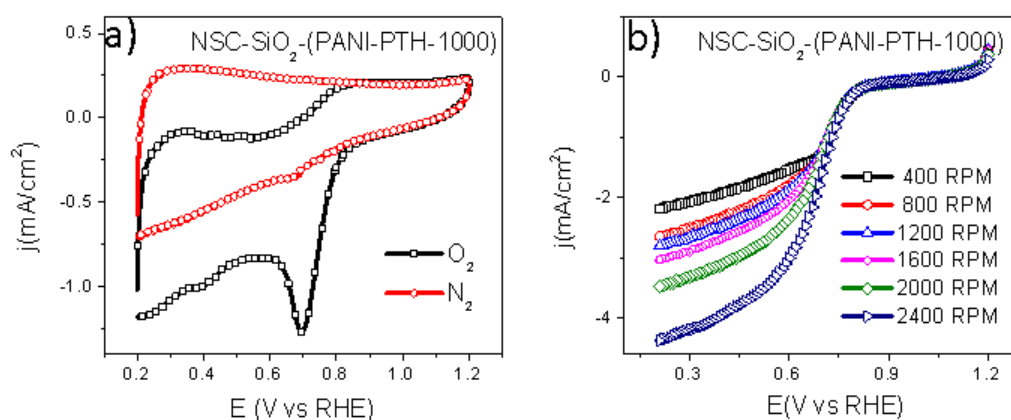
Figure 4.78-a) CV curves of NSC-SiO₂-(PANI-PTH-1000), and **b)** LSV curves.
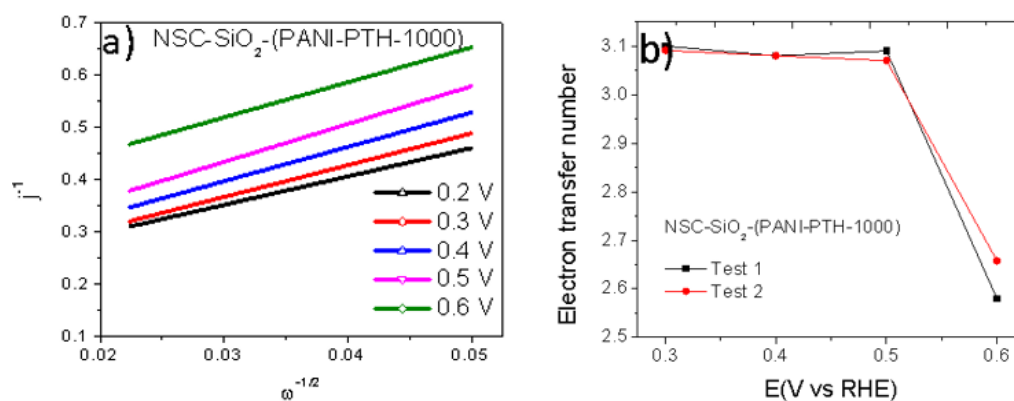
Figure 4.79-a) Koutecky-Levich plot of NSC-SiO₂-(PANI-PTH-1000), and **b)** corresponding electron transfer number values.
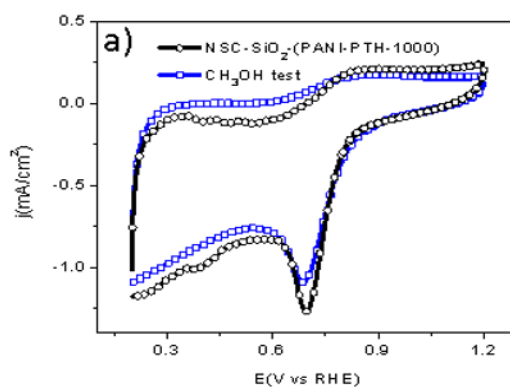
Figure 4.80-a) Resistance to methanol poisoning test shown in CV of NSC NSC-SiO₂-(PANI-PTH-1000).

The sample NSC (PANI-PTH-HF), obtained from the treatment with hydrofluoric acid, showed onset potential value of 0.90 V vs RHE with high current density of peak at 1.4 mA/cm^2 and half wave potential of 0. 8 V vs RHE (**Figure 4.81-a**).

LSV curves also presented high diffusion limited current density with linear plateau with highest current density value of current density of 5 mA/cm^2 at 2400 rpm, as shown in **Figure 4.81-b**. **Figure 4.82-a** shows the Koutecky-Levich plot, and the electron transfer number values with respect of the potential as shown in the **Figure 4.82-b**, the average electron transfer number value of 3.5, indicating a mixed electron transfer pathway for ORR electrocatalysis of etched sample NSC(PANI-PTH-HF). Such ORR performance can be associated with the exposure of active sites upon hydrofluoric acid treatment.

Figure 4.83-a shows the methanol poisoning effect on the catalyst. The NSC (PANI-PTH-HF) shows excellent methanol tolerance and no change in onset potential. Chronoamperometry test (**Figure 4.83-b**) displays loss in current after 30000 seconds of operation, indicating good stability of catalyst in alkaline solution.
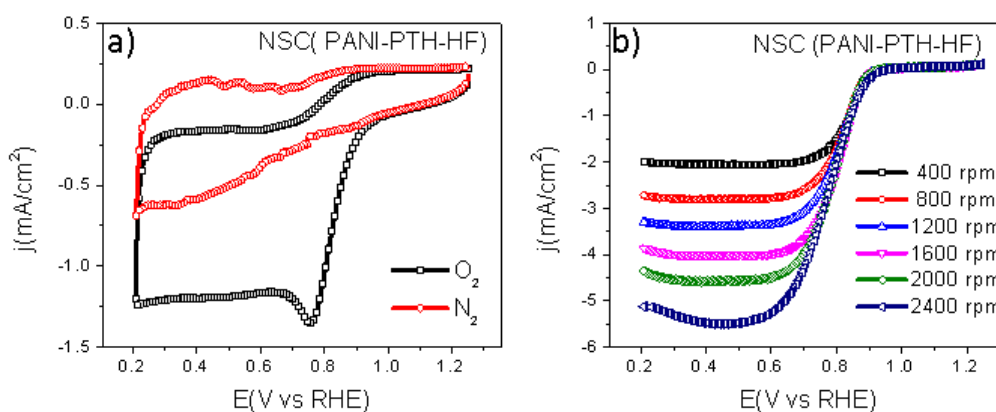
Figure 4.81-a) CV curves of the sample NSC(PANI-PTH-HF) shows onset potential value of 0.9 V vs RHE, and **b)** LSV curves of the sample NSC(PANI-PTH-HF).
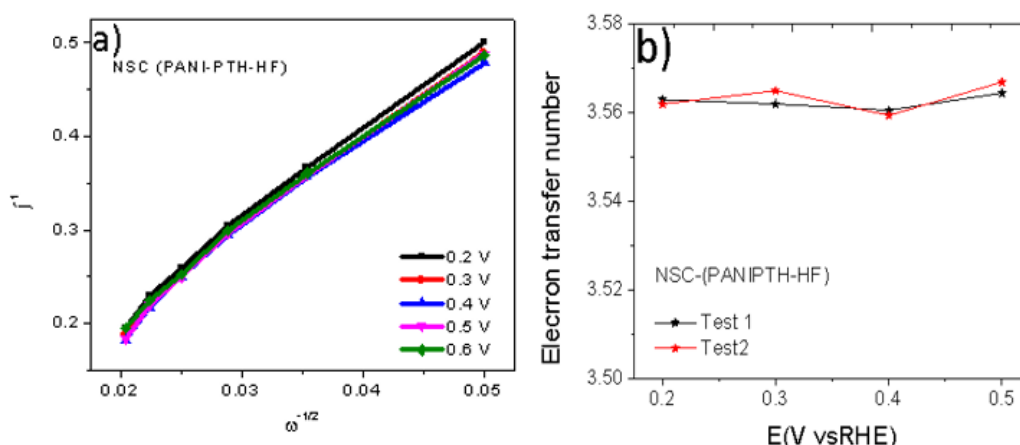
Figure 4.82-a) Koutecky-Levich plot using values of current density collected at the disc, and **b)** Average electron transfer number value 3.5.
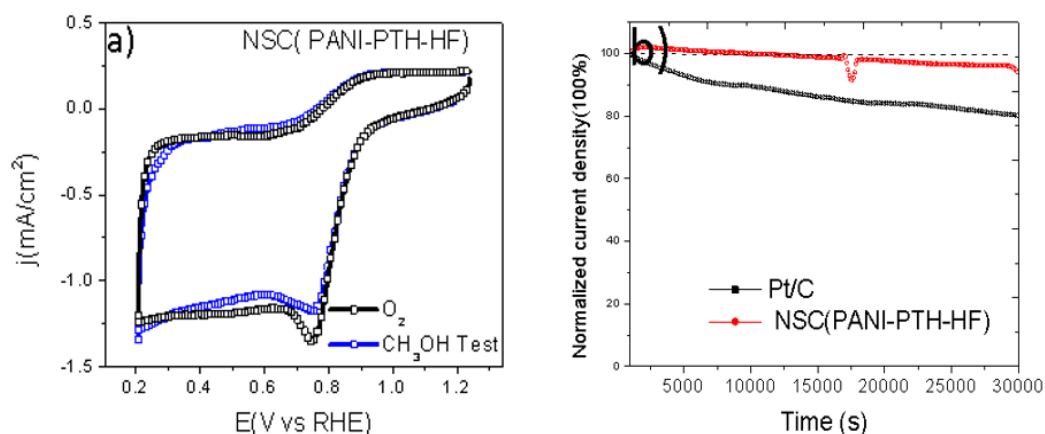
Figure 4.83-a) Resistance to methanol poisoning test of sample NSC (PANI-PTH-HF) and **b)** Stability test of the sample NSC (PANI-PTH-HF).

Further, a comparison test was made between NSC-SiO$_2$-(PANI-PTH-1000), NSC-SiO$_2$-(PANI-PTH-900), NSC(PANI-PTH-HF) and benchmark Pt/C (20 wt.%) (**Figure 4.84-a, b**).

Sample NSC(PANI-PTH-HF) showed better ORR performance with onset potential at 0.9V vs RHE and half-wave potential at 0.85 V vs RHE compared to the NSC-SiO$_2$-(PANI-PTH-1000) (onset potential at 0.88V vs RHE and half wave potential at 0.80 V vs RHE), and NSC-SiO$_2$-(PANI-PTH-900) (onset and half-wave potential values, 0.86V vs RHE, and 0.80V vs RHE) (**Figure 4.84-a**). This is a slight enhancement which may be attributed to the larger surface area and better exposure of active sites to the electrolyte. However, NSC(PANI-PTH-HF)

showed less positive onset potential than that of the benchmark Pt/C, which was expected (**Figure 4.84-b**).

It is worth to noting that, etched sample obtained from PANI and PTH precursors was not able to reach the same performance as the one produced from PANI and PEDOT precursors. This difference in ORR performance of sulfur and nitrogen co-doped carbons from different precursors combinations is due to the variation in the content of dopants, structure, defects, and degrees of graphitization in the respective samples. The synergy among heteroatom co-dopants and optimized morphology affects the final catalyst activity, and in this case, an optimum content of sulfur dopants was hard to achieve when using PTH as source of sulfur doped carbon.
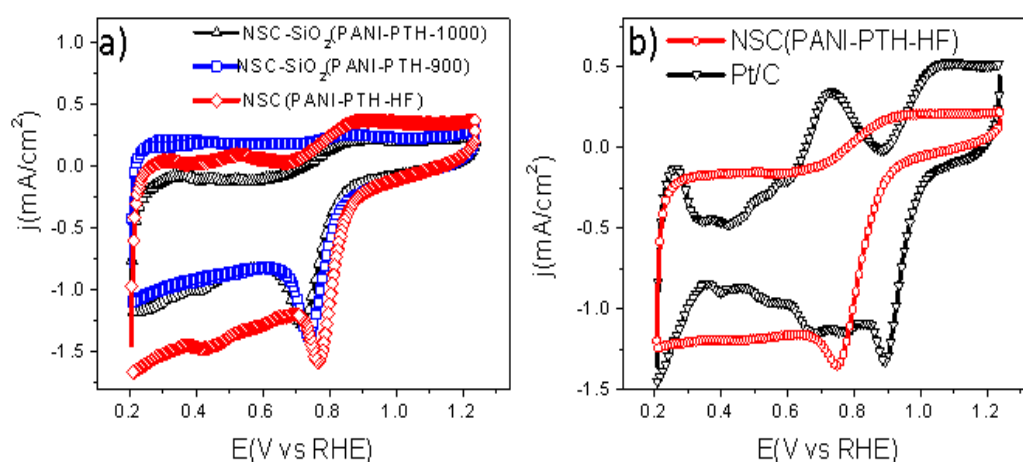
Figure 4.84-a) Comparison of CV curves of the samples NSC-SiO_2- (PANI-PTH-900), NSC-SiO_2- (PANI-PTH-1000) and NSC(PANI-PTH-HF), and **b)** Comparison of the CV curves of NSC(PANI-PTH-HF) and Pt/C based catalyst.

4.10 Physical characterizations of boron doped carbon

TEM images of boron doped carbon (BC-900) revealed spheres of near 500 nm of diameter (**Figure 4.85 a, b**). In the case of sample BC-1000, the TEM images identified arm-like structures and apparently some spheres were joined by a neck, probably due to the connection of two adjacent carbon spheres during carbonization at 1000°C. (**Figure 4.85 c, d**)
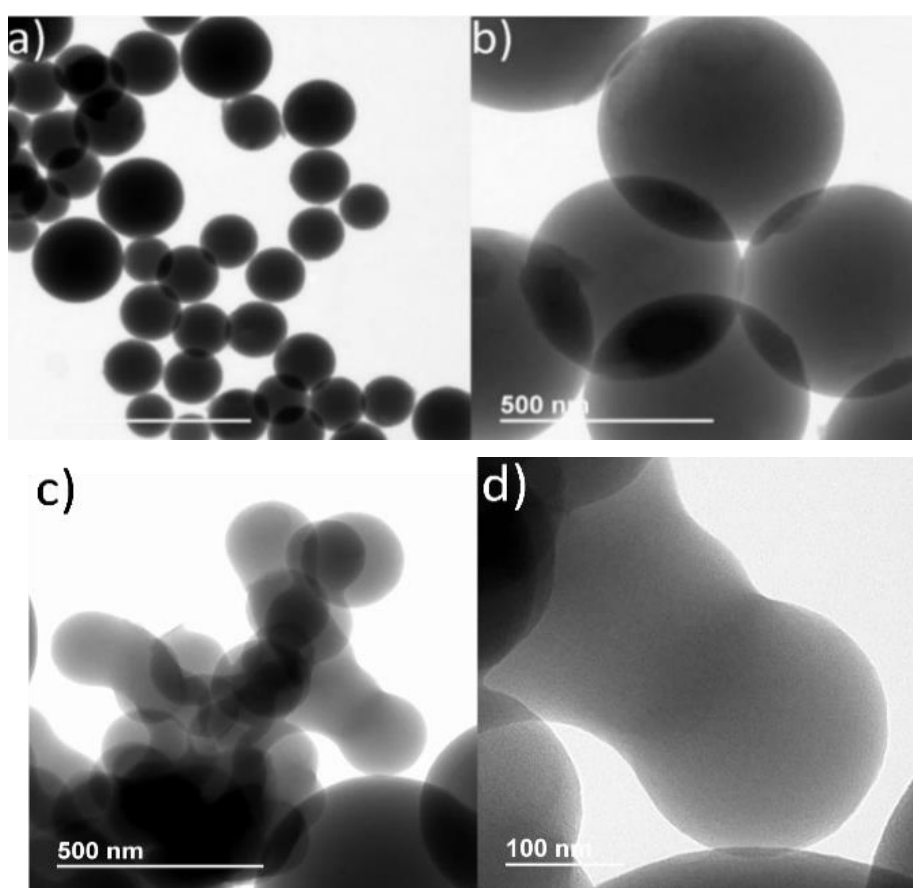
Figure 4.85-a, b) TEM images of boron doped carbon spheres (sample BC-900)and **c, d)** TEM images of boron doped carbon (sample BC-1000).

Figure 4.86-a shows the XPS survey of the sample BC-900. The elemental content was measured about 82% carbon, 14% oxygen, and 4% boron. **Figure 4.86-b** shows the deconvolution of B 1s for BC_2O at 193 eV, BCO_2 at

195.3 eV, and BC$_3$ at 192.3 eV **[28],[32],[33]** In the XPS spectra of O 1s, the peak at 531 eV was assigned to C=O/B-O and at peak 534.5 eV was assigned for O-H (**Figure 4.86-c) [32]**. In the XPS spectra of C 1s, the peak at 283.8 eV was assigned to B$_4$C, the peak at 285 eV represents to C=C/ C-C (**Figure 4.86-d) [32]**.

XPS survey of sample BC-1000 showed 85% carbon, 13% oxygen, and 2% boron (**Figure 4.87-a,b)** shows the XPS spectra of B 1s, where the peak at binding energy of 190 eV assigned to Sp^2 B-C(53.1%) and the peak at 194 eV to BCO$_2$ (46.9%) for sample BC-1000. XPS spectra of O 1s shows two peaks for C=O/B-O (532.7 eV) and O-H (531.9 eV) (**Figure 4.87-c**), and XPS spectra of C 1s showed the peaks at 284.6, 285.9, and 287.0 eV were assigned to B$_4$C, C=O/B-O, and C=O/ C-O, respectively (**Figure 4.87-b**).

Raman spectra was used to evaluate defect density of boron doped carbon materials (**Figure 4.88-a**). Two broad bands called D bands and G bands were identified at 1323 cm^{-1}, and 1595 cm^{-1} (BC-900) and at 1331 cm^{-1} and 1588 cm^{-1} (BC-1000), respectively. The G band is referred to ideal graphitic ordered sp^2 carbon, and the D band indicates defects. The ratio between intensity I$_D$ (disordered) and I$_G$ (ordered) bands is used to measure the degree of disorder in the boron doped material. **[32]** The ratio of I$_D$/I$_G$ of sample BC-900 was 1.34 and of sample BC-1000 was 1.27, respectively. This indicates that the sample BC-1000 has a lower ratio of I$_D$/I$_G$, suggesting the higher graphitic sp^2 carbon but lower defects. **[32]-[33]** In XRD diffraction pattern, (**Figure 4.88-b)**, there are two main peaks at 24° and 45° corresponding to 002 and 100 planes of graphitic carbon. The peak intensity at 24° is slightly higher for BC-1000, might be due to increased crystallinity of carbon. **[32], [34]**
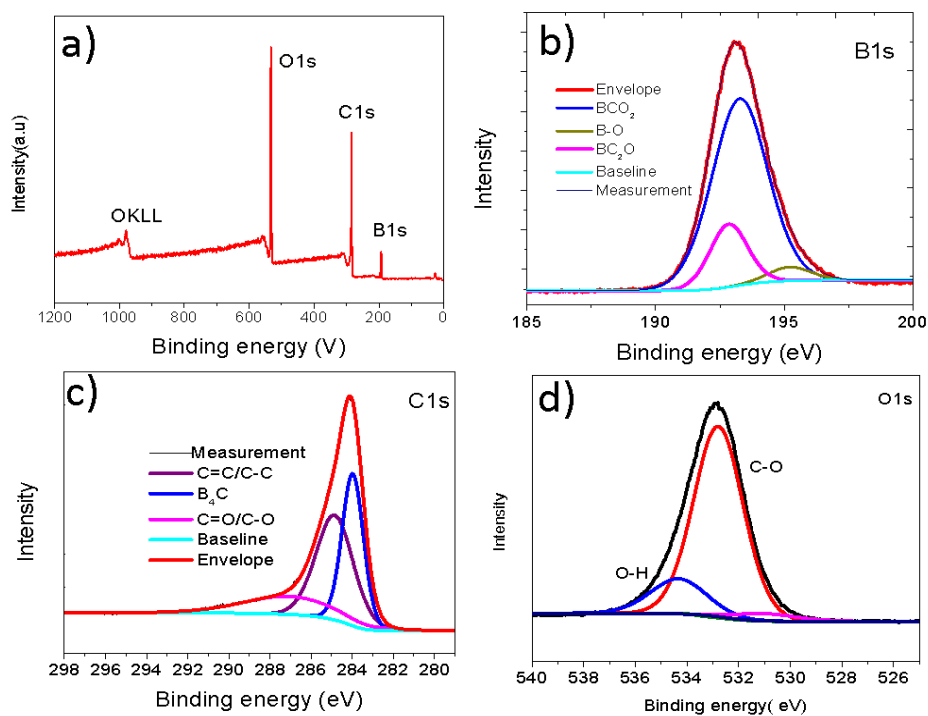
Figure 4.86-a) XPS survey of BC-900, **b)** XPS spectra of B 1s, **c)** XPS spectra of O 1s, and, **d)** XPS spectra of C 1s.
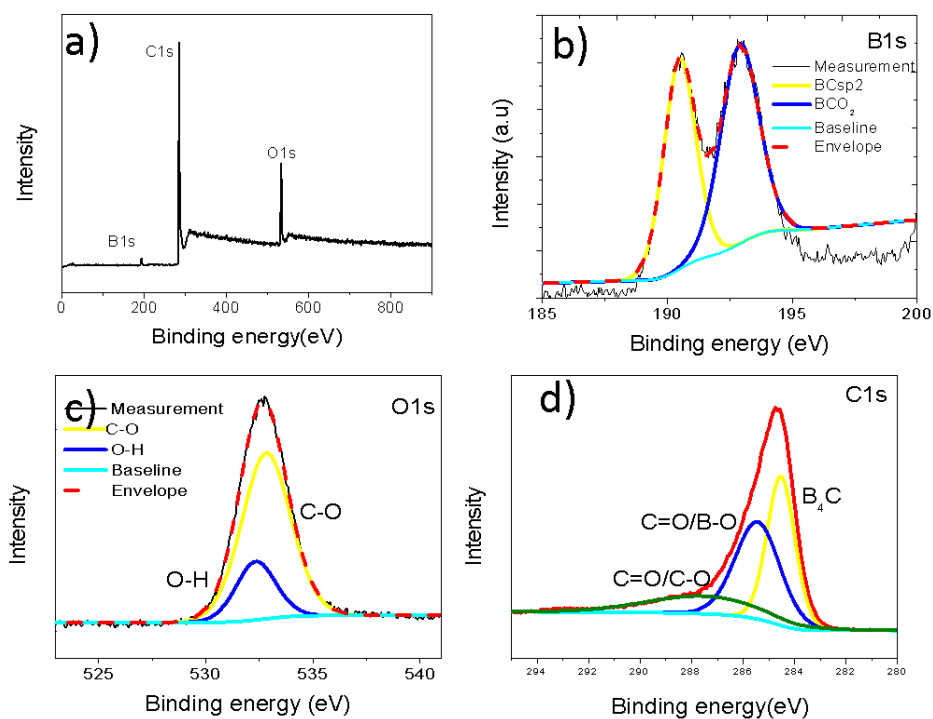
Figure 4.87-a) XPS survey of BC-1000, **b)** XPS spectra of B 1s, **c)** XPS spectra of O 1s, and, **d)** XPS spectra of C 1s.
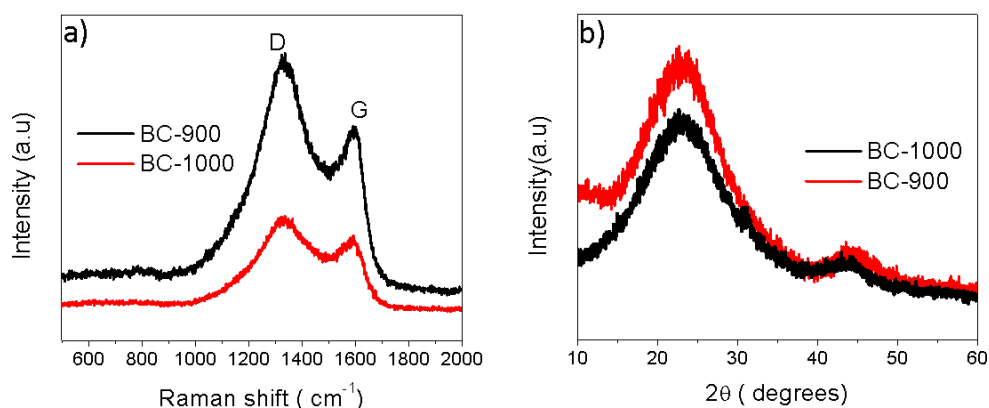
Figure 4.88-a) Raman spectra, **b)** XRD diffraction patterns for BC-900 and BC-1000.

CV curves of the sample BC-900 is presented in **Figure 4.89-a**, which shows onset potential at 0.78 V vs RHE and current density peak value of 1.2 mA/cm^2. In the LSV curves of the sample BC-900 (Figure **4.89-a)** the curves present increase in current density with the RPM. The electron transfer number values of sample BC-900, calculated via Koutecky-Levich plot (**Figure 4.90-a**) at different respective potentials are found between 2.45 (0.2V vs RHE) and 2.20 (0.5V vs RHE) (**Figure 4.90-b**). Ring and disk currents collected during LSV test of sample BC-900 are shown in (**Figure 4.91-a**), and corresponding average electron transfer number was calculated to be 2.6 (**Figure 4.91-b**). Peroxide production by the catalyst BC-900 was calculated at different potentials with average value of 52.3% (**Figure 4.91-c**), which is in conformity with the electron transfer number path near to 2 electrons, with production of intermediate peroxide compounds.
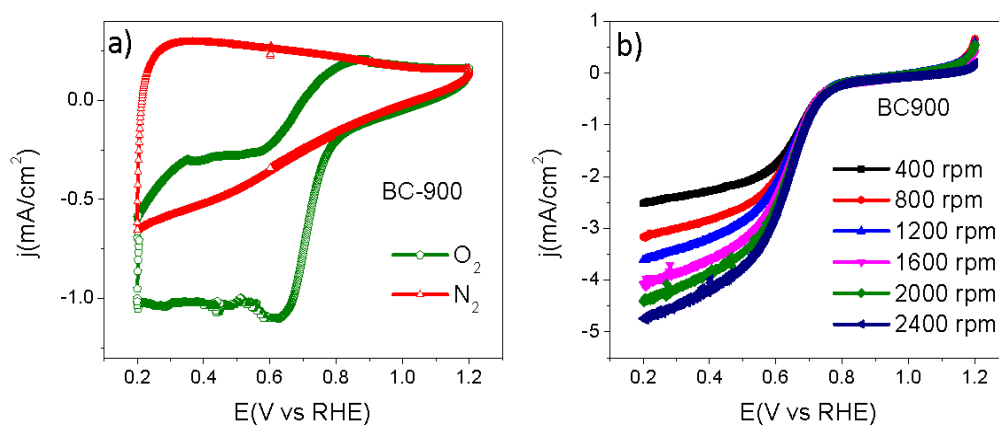
Figure 4.89-a) CV curves of BC-900 and **b)** LSV curves of BC-900.
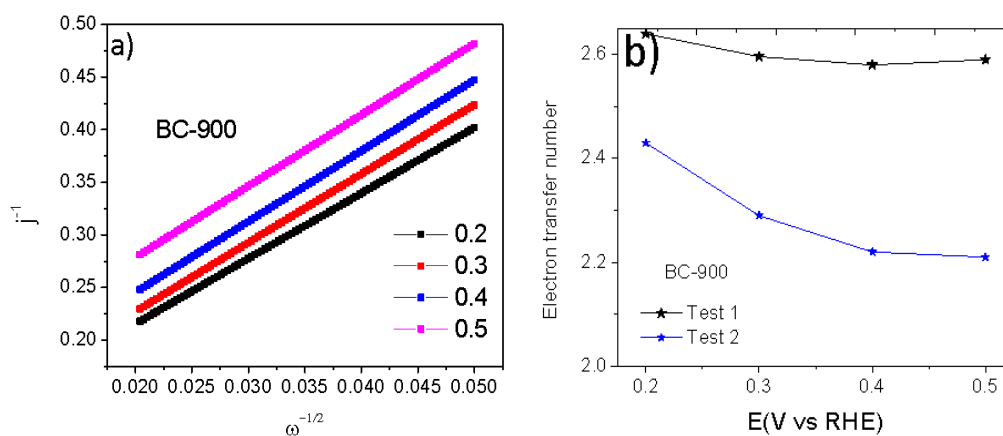
Figure 4.90-a) Koutecky-Levich of BC-900, **b)** Electron transfer number values of BC-900.
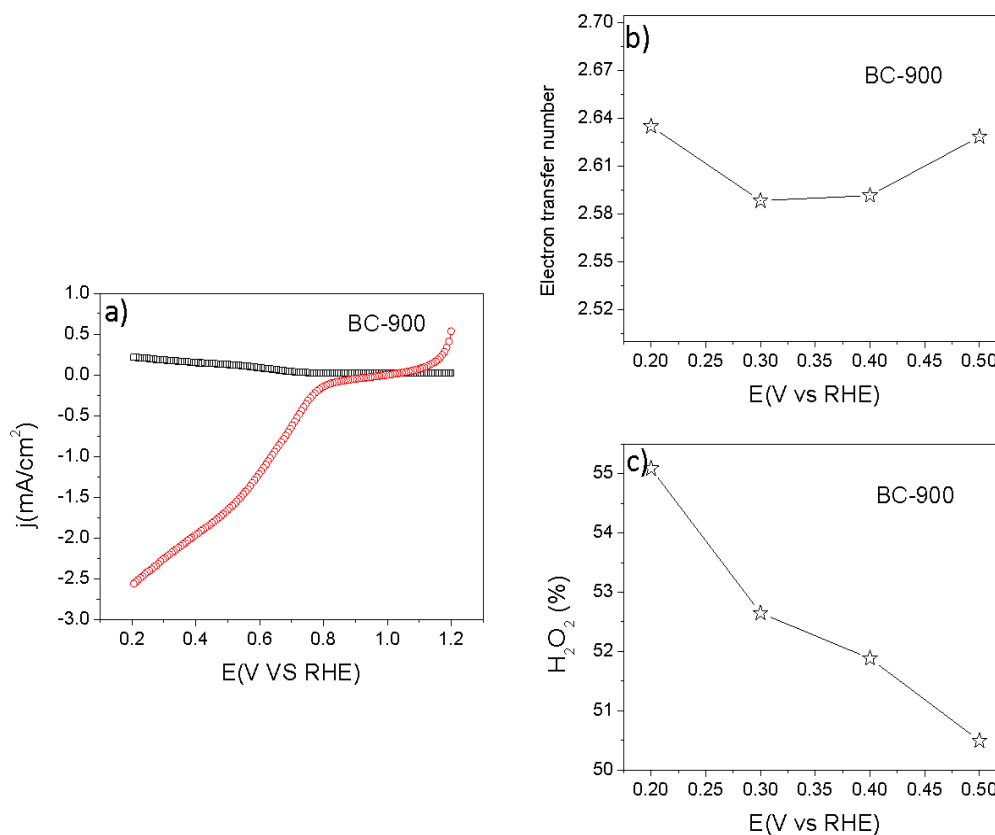
Figure 4.91-a) LSV curves collected at ring and disk of BC-900, **b)** Corresponding electron transfer number, and **c)** Peroxide production at different potentials.

In the case of sample BC-1000, the CV and LSV curves showed onset potential value of 0.77 V vs RHE (**Figure 4.92-a,b**). The electron transfer number values of sample BC-1000, calculated via Koutecky-Levich plot (**Figure 4.93-a**) according to the respective potentials were found to between 2.2 (0.2V vs RHE), and 1.98 (0.5V vs RHE) (**Figure 4.93-b**). The current collected at ring and disk electrode (**Figure 4.94-a**) were used for calculating the electron transfer number at respective potentials, the average electron transfer number was near 2 (**Figure 4.94-b**). The percentages of peroxide generation for sample BC-1000 were calculated, and found between 78% (0.2V vs RHE) and 66% (0.4V vs RHE), as shown in **Figure 4.94-c**.
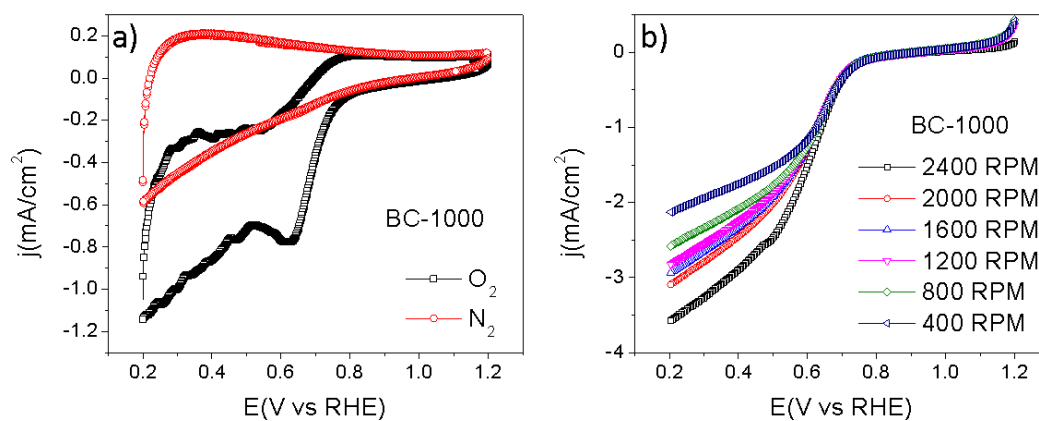
Figure 4.92-a) CV curves of BC-1000 and **b)** LSV curves of BC-1000.
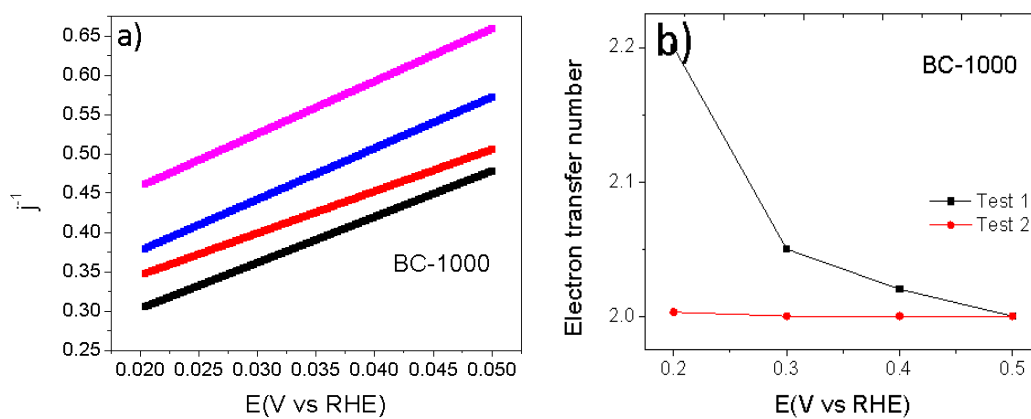
Figure 4.93-a) Kouteck-Levich plot of BC-1000 and **b)** corresponding electron transfer number valuesof BC-1000.
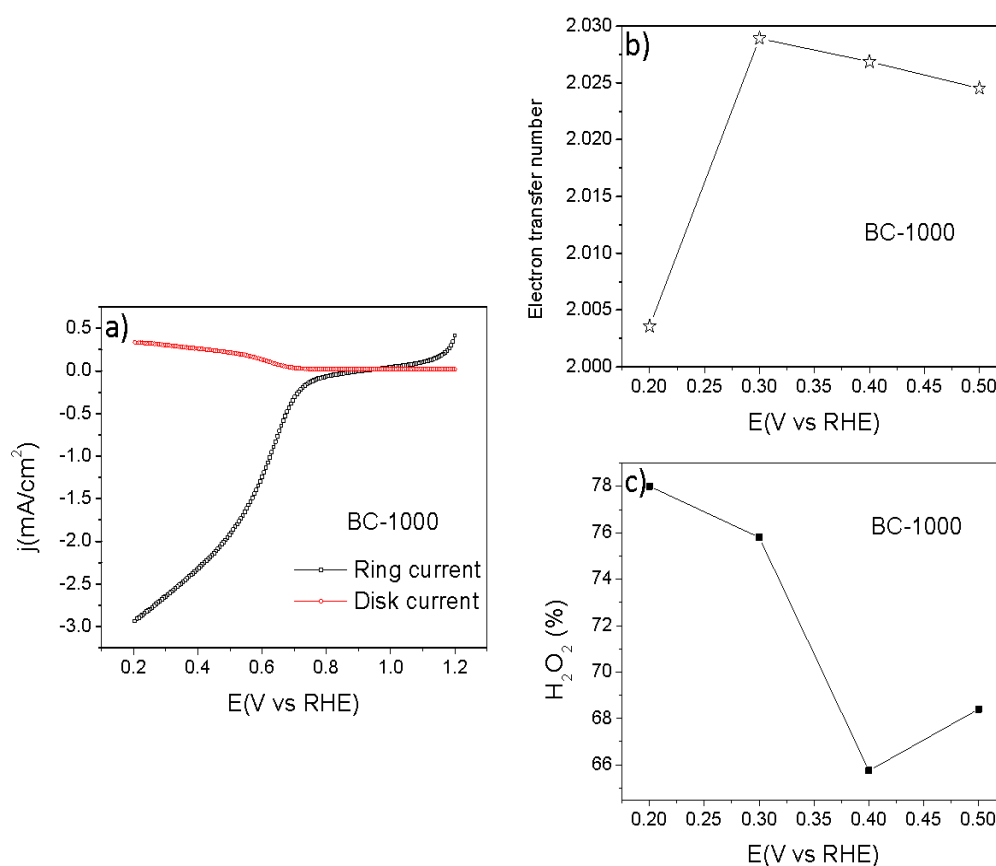
Figure 4.94-a) LSV curves of ring and disk at 1600 RPM, **b)** Corresponding electron transfer number, and **c)** Peroxide production percentage at different potentials.

4.11 Physical and electrochemical characterizations of boron and nitrogen co-doped carbon

The morphological structures of the as prepared samples NBC-900 and NBC-1000 (derived from polymerization and carbonization of PANI onto boron doped carbon spheres (BC-900)) were investigated by TEM analysis, as shown in **Figures 4.95-a, b.** TEM images revealed agglomerated layers of carbon. The cores made of 'boron doped carbon spheres' did not work as the silicon nitrides and silicon dioxide core particles. Instead of obtaining a well-defined structure, the nitrogen and boron doped carbon materials do not have a specific morphology. It is possible that during the preparation process of nitrogen and

boron doped carbon, the structure has collapsed and agglomerated (**Figures 4.95-a, b**).
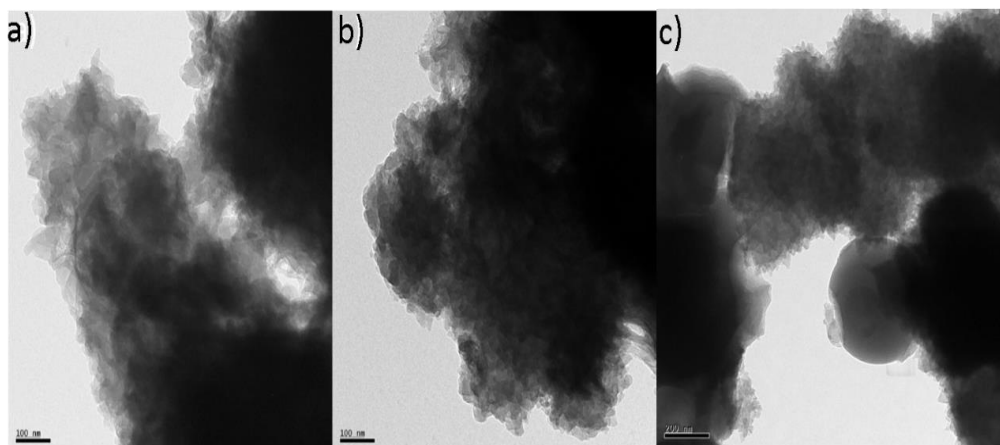
Figure 4.95-a, b) TEM images of NBC-900 and **c)** NBC-1000.

Figure 4.96-a shows the XPS survey of samples NBC-900. Sample NBC-900 presented the following contents of the elements, 82.2% carbon, 13% oxygen, 3% nitrogen, and 1.8% boron. In the XPS spectra of B 1s, the binding energies 189.0 eV, 190.2 eV, 191.4 eV, and 192.7 eV are ascribed to the B-C/BC_2O, BN/BC_2O, sp^2 C-B-N, and B-O. **[116]-[120]**

XPS spectra of B 1s of NBC-900 shows the peaks centered at 190.2 eV, 191.35 eV, and 193 eV which were ascribed to the B-C (40%), BN/BC_2O (31%), sp2C-B-N (19%) **Figure 4.96-b**. **[120]** N1s spectra of sample NBC-900 (**Figure 4.96-d**) showed peaks at 400 eV, 399 eV and 398 eV corresponding to 6% quaternary-nitrogen, 47% pyrrolic-nitrogen and 50% pyridinic-nitrogen.
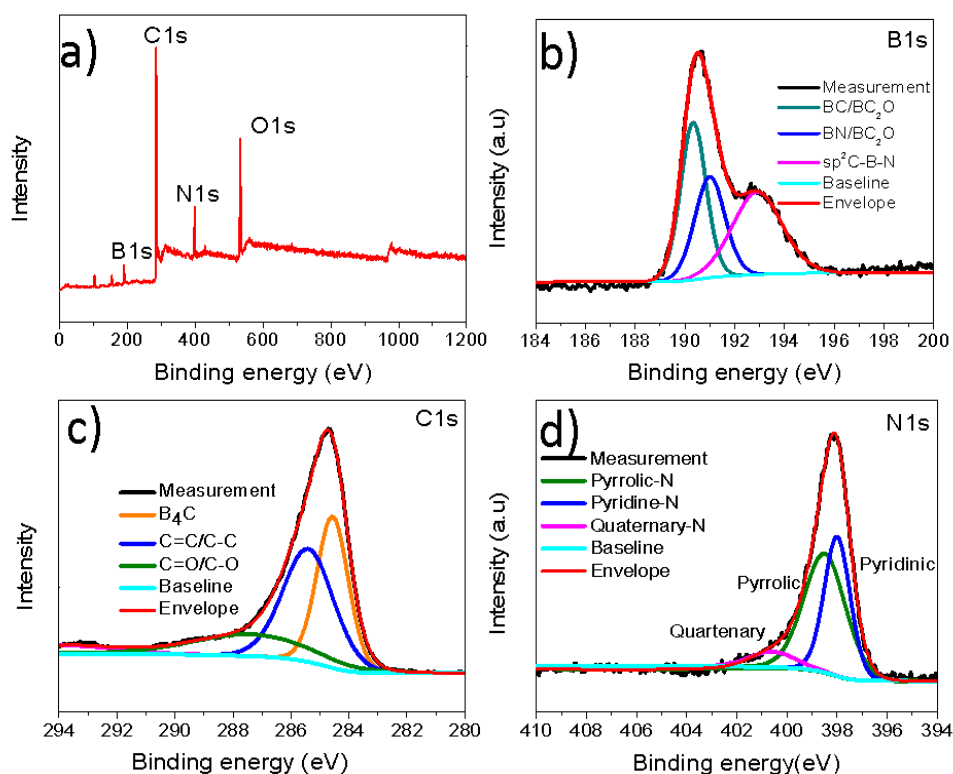
Figure 4.96-a) XPS survey of NBC-900, **b)** XPS spectra of B 1s, and **c)** XPS spectra of C1s and **d)** XPS spectra of N 1s.

The XPS survey of NBC-1000 (**Figure 4.97-a**) shows the presence of 0.8% boron, 2% nitrogen, 14% oxygen and 83.2% carbon are incorporated into the carbon lattice. In **Figure 4.97-b**, B1s spectrum of sample NBC-1000 presents the peaks BC/BC_2O at 191 eV, BN/BC_2O at 193 eV and BO/B_2O_3 at 195 eV. The percentage of species in the B1s spectra of sample NBC-1000 was calculated to be 18% of BC/BC_2O, 60% of BN/BC_2O, and 22% BO. The XPS spectra of N1s (**Figure 4.97-c**) assigned the binding energies of 398.5 eV to pyrrolic-N (41%), and 400 eV to quaternary-N (59%).
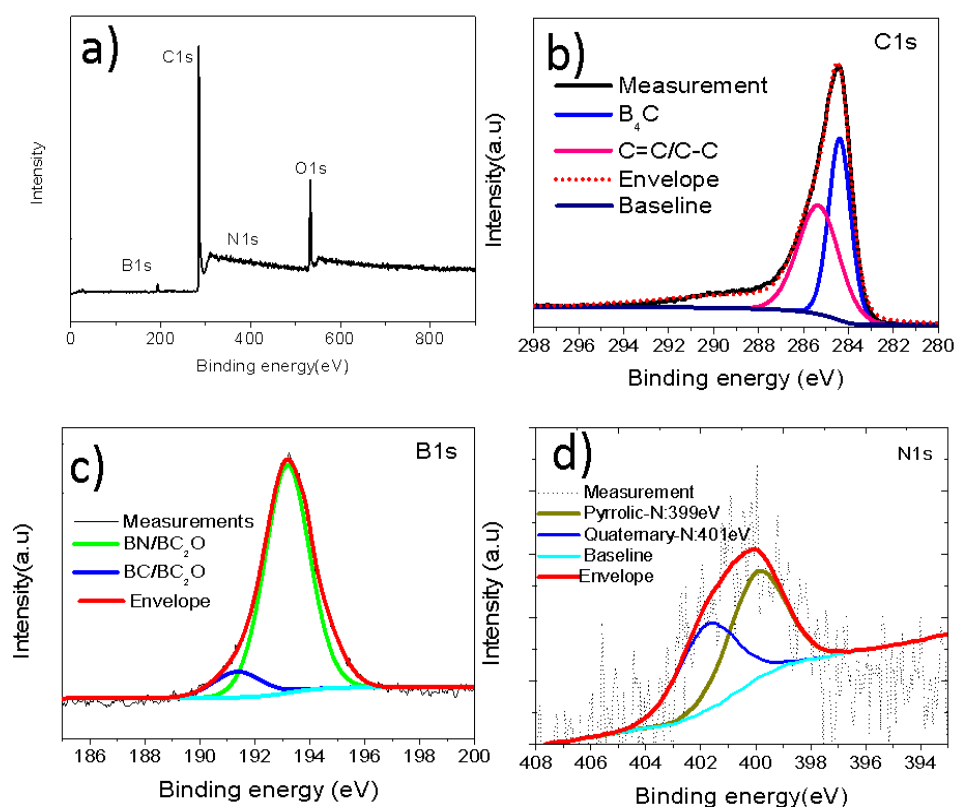
Figure 4.97-a) XPS survey of NBC-1000, **b)** XPS spectra of B 1s, and **c)** XPS spectra of N 1s.

Raman spectra (**Figure 4.98-a**) showed two characteristic peaks for D band and G band, with intensity ratio I$_D$/I$_G$ of 1.37 for sample NBC-900 and 1.28 for NBC-1000.The fact that both NBC-1000 and NBC-900 present higher I$_D$/I$_G$ ratio values than the I$_D$/I$_G$ ratio values of single boron doped carbon samples (BC-900 is 1.34, BC-1000 is 1.26), is due to introduction of defects with simultaneous nitrogen and boron co-doping. XRD diffraction pattern (**Figure 4.98-b**) showed two broad peaks at 23° and 43°, which were assigned to 002 and 100 planes of graphitic carbon. **[121]**-**[123]**
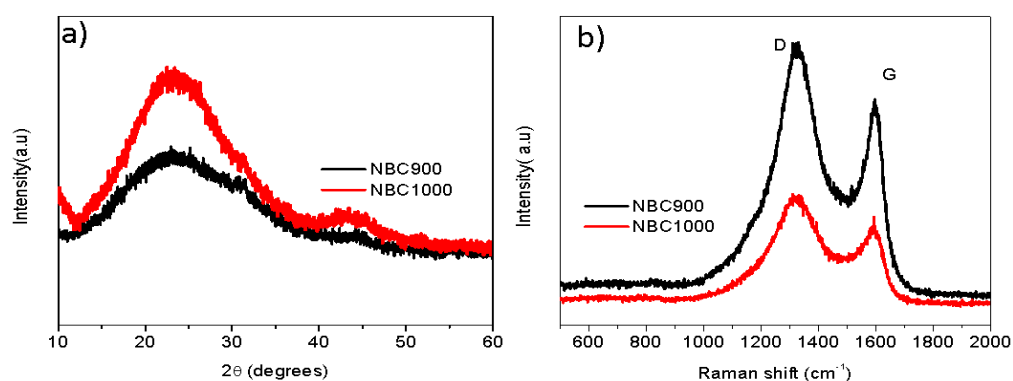
Figure 4.98-a) XRD patters of NBC-900 and NBC-1000. **b)** Raman spectra of NBC-900 and NBC-1000.

CV and LSV curves of sample NBC-900 showed the intense oxygen reduction peak in oxygen saturated 0.1 M KOH solution and onset potential at 0.82 V vs RHE (**Figure 4.99-a,b**). The LSV shows that the values of current increases with increasing the rotating speed. The electron transfer numbers were calculated from the data of Koutecky-Levich plot (**Figure 4.100-a**). **Figure 4.100-b** shows the electron transfer numbers with respective potentials as follows, 3.4 (0.2V), 2.9 (0.3V), 2.5 (0.4V), 2.3 (0.5V), and 2.1(0.6V). Sample NBC-900 also presented good methanol poisoning resistance with no loss in terms of onset potential and current density after adding methanol into the 0.1 M KOH electrolyte during ORR (**Figure 4.101-a**). The chronoamperometric test shows the loss in current of about 18% after 12 h (**Figure 4.101-b**).
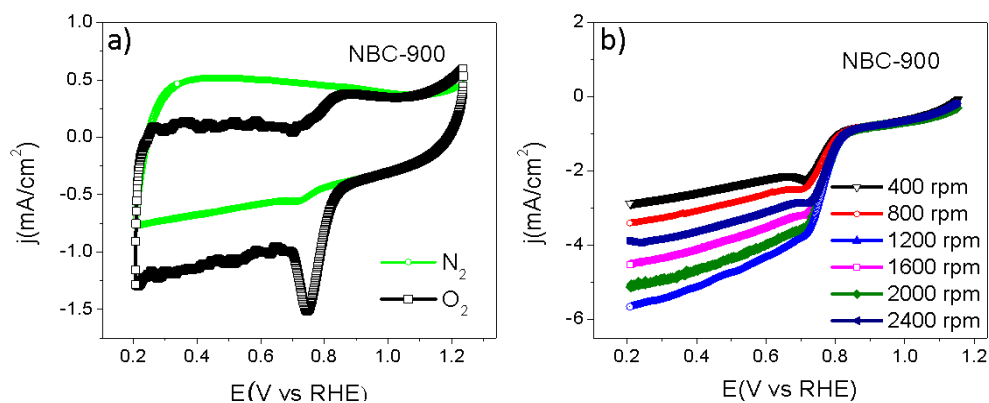
Figure 4.99-a) CV curves of NBC-900 and **b)** LSV curves of NBC-900.
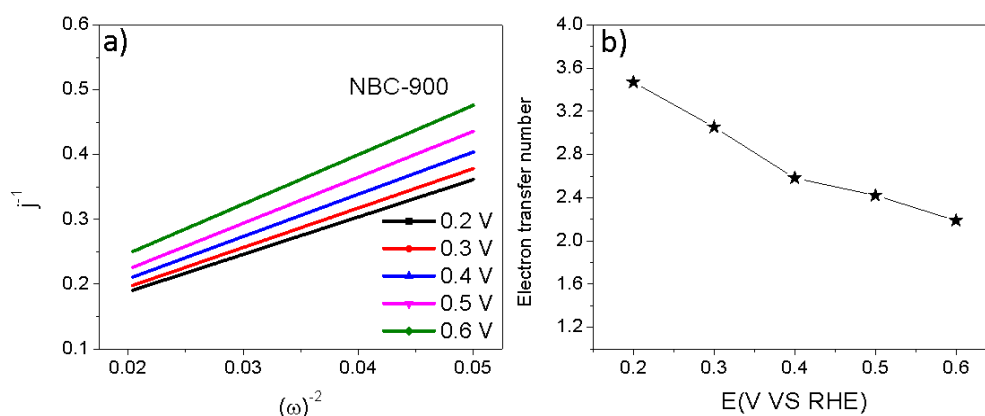
Figure 4.100-a) Koutecky-Levich plot of NBC-900 and **b)** corresponding electron transfer number values of NBC-900.
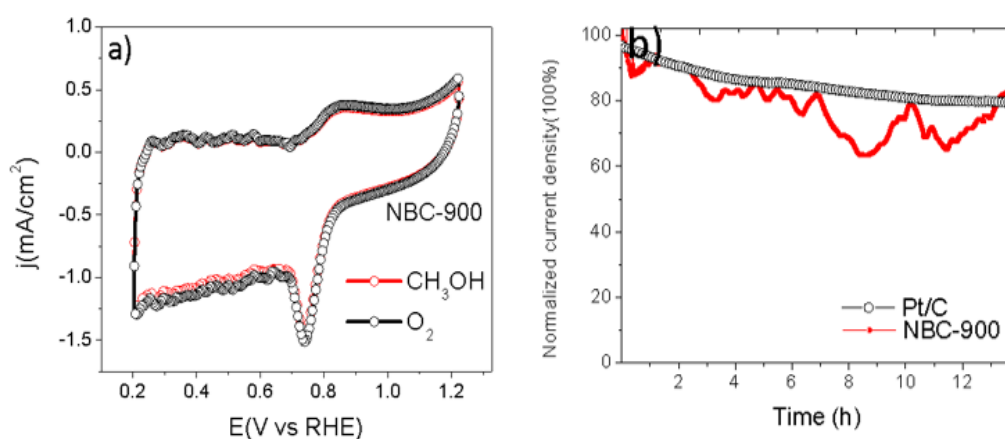
Figure 4.101-a) Methanol poisoning test for NBC-900, and **b)** Chronoamperometric test of NBC-900.

CV and LSV of sample NBC-1000 are presented in **Figure 4.102-a,b**. Sample NBC-1000 exhibited the oxygen reduction peak and an onset potential at 0.81 V vs RHE with 1.5 mA/cm^2 current density. The electron transfer numbers were calculated by using Koutecky-Levich plot (**Figure 4.103-a**), and the electron transfer numbers were measured as follows 2.5 (0.2V), 2.5 (0.3V), 2.45 (0.4V), 2.2 (0.5V) and 2 (0.6V) (**Figure 4.103-b**).
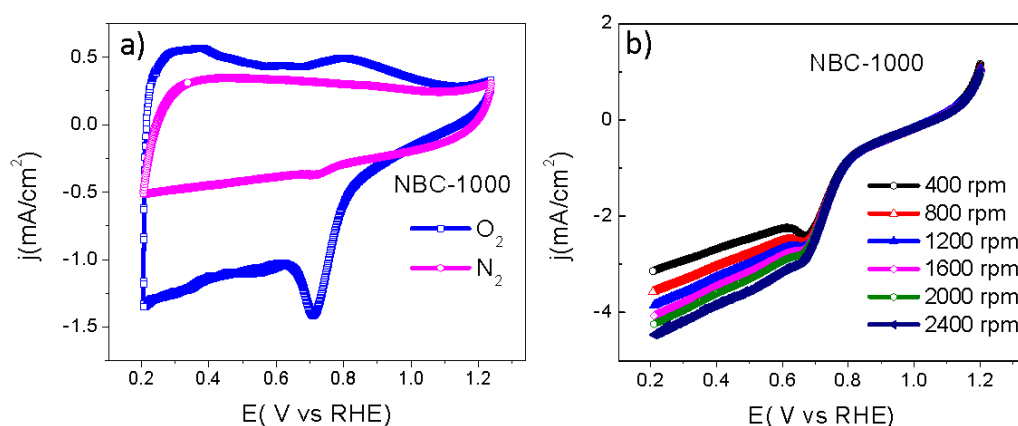
Figure 4.102-a) CV curve of NBC-1000 and **b)** LSV curves of NBC-1000.
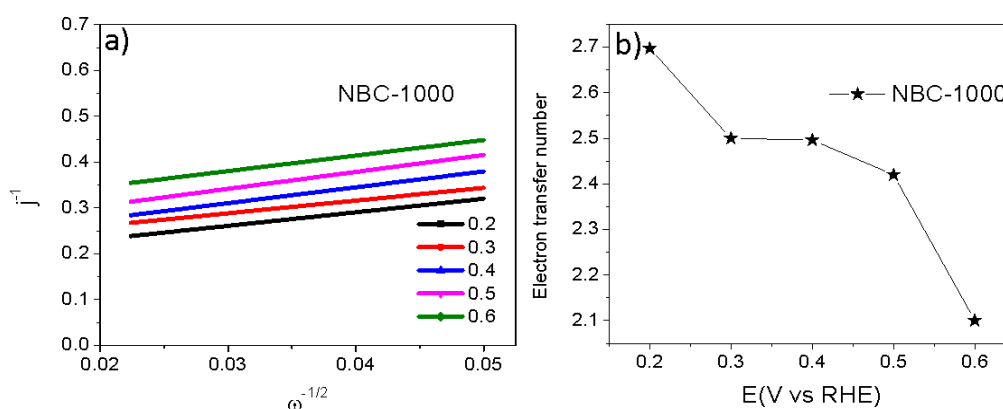
Figure 4.103-a) Koutecky-Levich plot of NBC-1000 and **b)** Corresponding electron transfer number values of NBC-1000.

Figure 4.104 shows the comparative CV curves of samples BC-900, BC-1000, NBC-900, NBC-1000, and benchmark Pt/C. Among the sample benchmark Pt/C shows better performance with most positive onset potential, which was expected. However, sample NBC-900 showed slight better ORR performance with onset potential of 0.82 V vs RHE among all the likewise prepared samples NBC-1000 (0.81 V vs RHE), BC-900 (0.78 V vs RHE), and BC-1000 (0.77 V vs RHE). The obtained performance, however, is comparable to that presented in several recently reported in literature. For example, nitrogen and boron carbon nano-onions from boric acid was reported with onset potential value of 0.78 V vs RHE and half wave potential value of 0.58 V vs RHE. **[122]**

Boron and nitrogen doped carbon from plasma treatment of triphenyl borate showed onset potential value of -0.18 V vs Ag/AgCl, (which was

approximately 0.78-0.79V vs RHE), and electron transfer numbers were measured in the range of 3 to 2.5 with respect of increasing potential. This is similar to the trend observed in our samples. **[123]** In another work, Qiao and coworkers prepared boron doped graphene which showed onset potential of -0.14 V vs Ag/AgCl (approximately 0.81 V vs RHE). **[124]**

The catalytic activity of our as-synthesized boron and nitrogen co-doped carbon materials is inferior when compared to the best PT/C catalyst. However, the catalytic activity of our boron and nitrogen co-doped carbon catalysts is consistent with that reported in earlier works that produced similar materials. **[123]- [124]**
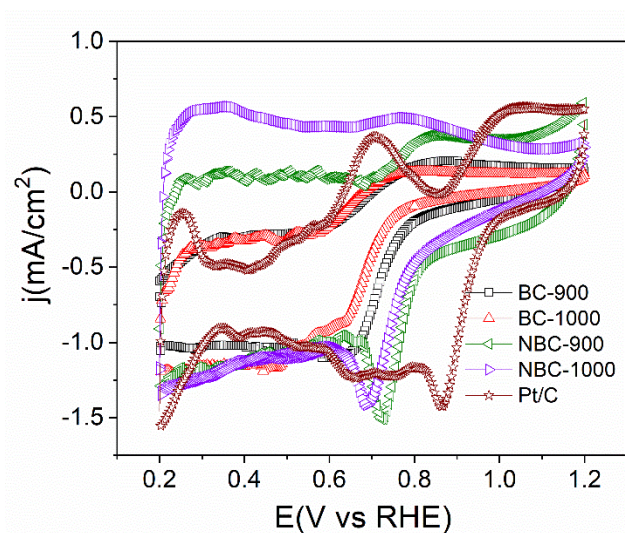
Figure 4.104- Comparison of CV curves of BC-900, BC-1000, NBC-900, NBC-1000, and Pt/C.

5 CONCLUSIONS

5.1 Specific conclusion about the work using silicon nitride, silicon dioxide, polyaniline and poly(3,4-ethylene-dioxythiophene)

In summary, we have synthesized a range of carbon materials with single and co-doped heteroatoms, using PANI and PEDOT precursors coated on Si_3N_4 and SiO_2 nanospheres followed by the carbonization process.

Nitrogen doped carbon coated on Si_3N_4 nanospheres and sulfur and nitrogen co-doped carbon coated Si_3N_4 nanospheres were prepared through sequential polymerization of aniline and EDOT monomers. The resulting carbon catalysts showed coral-like morphological structures with excellent electrocatalytic ORR properties. The nitrogen doped carbon coated on Si_3N_4 nanospheres exhibited the onset potential of 0.90 V vs RHE.

To the best of our knowledge, this was the first ever attempt to use Si_3N_4 nanospheres (20 nm) as core to produce coral-like doped carbon electrocatalyst for ORR. The Si_3N_4 nanospheres not only provided support to obtain coral-like structure of carbon but also indirectly provide high nitrogen content to catalyst material. Interestingly, even after the second polymerization step of EDOT followed by pyrolysis, the Si_3N_4 nanospheres remained coral-like nanostructure. The optimum presence of pyridinic, pyrrolic and quaternary-nitrogen species, ultimately contributed to the excellent performance of the nitrogen doped carbon samples. The sulfur and nitrogen co-doped carbon coated Si_3N_4 nanospheres showed excellent ORR activity achieving onset potential of 0.91 V vs RHE, benefitting from the synergy of co-doping effect.

In another work, the SiO_2 nanospheres were coated by aniline and EDOT monomers via polymerization and carbonized to construct nitrogen doped carbon, sulfur doped carbon, and nitrogen and sulfur co-doped carbon. The alternating sequence of aniline and EDOT coating on SiO_2 were also made in order to test their effect in catalysis performance.

Nitrogen and sulfur co-doped carbon coated on SiO_2 materials presented more positive onset potential, and current density, than the mono sulfur or

nitrogen doped carbon counterparts. This is attributed to the synergy between the N and S dopants.

In addition, the alternate sequence of PANI and PEDOT coating (NSC-900 and SNC-900) also caused different catalytic performance, when the outer coating was constituted by nitrogen doped carbon (from PANI) showed better ORR performance than the outer coating constituted by sulfur doped carbon (from PEDOT). Thus, highlighting that the synthetic route and sequence of polymerization plays an important role when combining polymer precursors to obtain co-doped carbon nanocatalyst.

Furthermore, the as-synthesized samples were subjected to HF etching to remove SiO_2 core from the carbon materials and tested for ORR electrocatalysis. After etching, the nitrogen and sulfur co-doped carbon catalysts (NSC-HF) showed the best ORR performance by achieving the onset potential 0.94 V vs RHE very close to the benchmark Pt/C catalyst (0.99 V vs RHE). This indicates that the SiO_2 does not contribute to catalytic performance, the ORR activity is merely originated from the nitrogen and sulfur co-doped carbon. The overall catalytic performance can be attributed to the high surface area, porous structured material, and the synergy of dual dopants.

Taking into consideration the importance of the electron transfer number values for evaluation of the catalyst materials activity towards ORR, we present in **Figure 5.1** the electron transfer number values according to the respective potentials for the samples NC-14-900-20, NC-14-1000-20, SNC, NC-900, NSC-900, NSC-HF, SNC-900, SNC-HF, SC-900 and SC-1000. The respective synthetic routes for each one of the samples are found in this Dissertation.
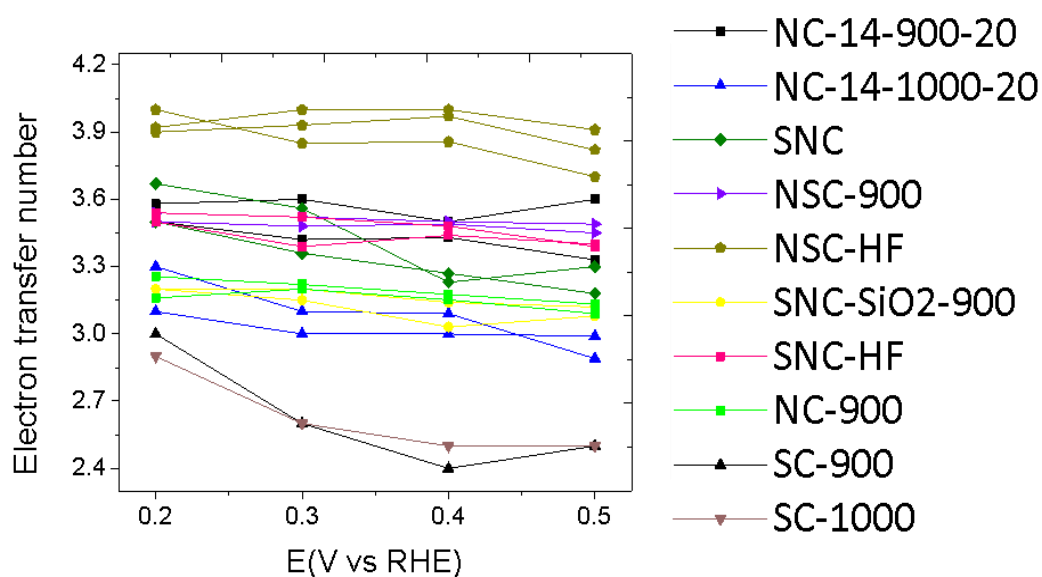
Figure 5.1- Electron transfer number values according to the potentials.

5.2 Specific conclusion about the work using silicon dioxide nanospheres, polyaniline and polythiophene

In this section of the work, the nitrogen and sulfur co-doped carbon nanomaterials were prepared using the precursors PANI and PTH followed by carbonization.

Herein, the synthesis of polyaniline was carried out via a simple oxidative polymerization in the presence of the sulfur doped carbon coated silicon dioxide (prepared from PTH). The co-doped samples were named as NSC-SiO$_2$-(PANI-PTH-900) and NSC-SiO$_2$- (PANI-PTH-1000) and showed relatively fair onset potential values of 0.88 V vs RHE, and 0.86 V vs RHE.

Via a second step of etching the samples, the material was turned into nitrogen and sulfur co-doped carbon, denoted as NSC-PTH-PANI-HF, which presented onset potential 0.9 V vs RHE. In fact, the nitrogen and sulfur co-doped material presented more positive value of onset potential than the sulfur doped carbon (0.79 V vs RHE).

5.3 Specific conclusion about the work using boric acid, sucrose and polyaniline

In this part of work, boron doped carbon materials (BC-900 and BC-1000) were prepared from hydrothermal method using sucrose and boric acid as precursors, followed by carbonization. The samples showed onset potential of 0.79 V vs RHE (BC-900) and 0.77 V vs RHE (BC-1000). Then, nitrogen and boron co-doped carbon samples were prepared using boron doped carbon spheres (BC-900) coated with PANI, followed by carbonization at 900°C and 1000°C. The nitrogen and boron co-doped carbon NBC-900 and NBC-1000 showed an onset potential of 0.82 V vs RHE and 0.81 V vs RHE, respectively. Overall, boron and nitrogen co-doped samples presented slightly more positive onset potential than that of boron doped carbon.

Figure 5.2 presents the values of electron transfer number calculated to each one of the potentials for the samples NSC-SiO$_2$-(PANI-PTH-900), NSC-SiO$_2$- (PANI-PTH-1000) NSC-(PANI-PTH-HF), BC-900, BC-1000, NBC-900 and NBC-1000.
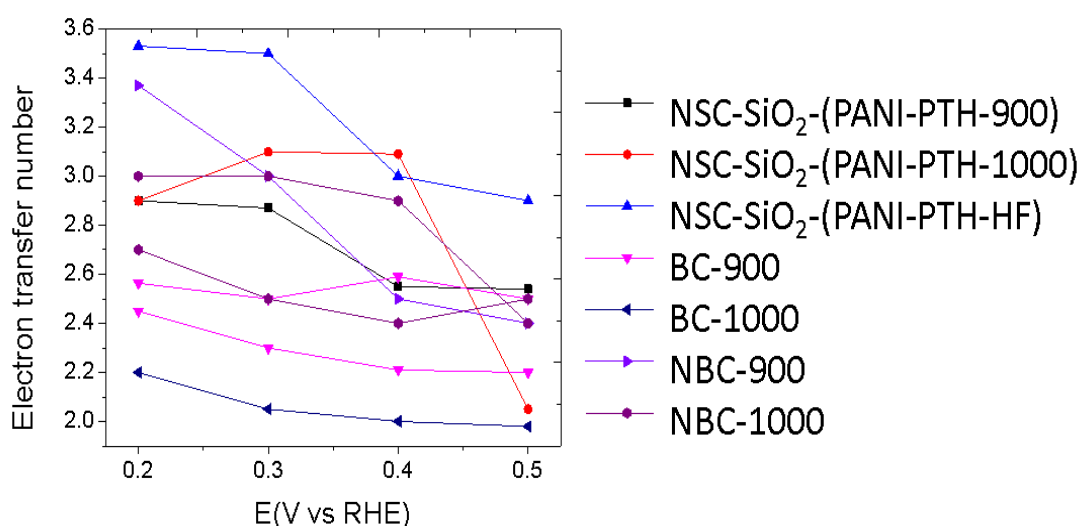
Figure 5.2- Electron transfer number values according to the potentials.

5.4 Specific considerations about hydrofluoric acid waste residues treatment

Hydrofluoric acid is considered a hazardous chemical and the treatment of its waste residues is very important to avoid environmental health problems.

There are different strategies for treating water containing hydrofluoric acid waste residues, such as chemical coagulation with polyaluminum chlorides or aluminum sulfates [125]; precipitation using calcium salts [126–128]; electrocoagulation [129,130]; reverse osmosis [131,132]; ion exchange [133,134]; and membranes for microfiltration, nanofiltration and ultrafiltration. [135]

Lin et al proposed the treatment of hydrofluoric acid waste water by ion exchange process consisting of two ion exchange and two regeneration steps. They used strong base anionic and strong acid cationic resins through a continuous operation system. As a result of their treatment, the wasted hydrofluoric acid was recovered and ready to be reused. The recovered hydrofluoric acid could also be converted into high purity calcium fluoride by calcium chloride. [134]

Chung and coworkers have studied the treatment of hydrofluoric acid waste water from semiconductor manufacturing facilities in Korea, and proposed three methods: coagulation, ion exchange and reverse osmosis. They found that the reverse osmose method affected effectively the quality of resulting water. In terms of reverse osmose treatment, they pointed out that the polyamide membranes were superior and more cost effective in reverse osmose when compared with cellulose acetate membranes. [135]

The treatment of hydrofluoric acid containing waste water is very important to avoid environmental contamination. The recovery of the acid in pilot scale for reuse can provide economic and environmental solutions as mentioned in literature, and seems an alternative when large amounts of hydrofluoric acid are used. [134]-[135] All residues from hydrofluoric acid produced during our research were properly stored and treated by the environmental health and safety department at Case Western Reserve University.

5.5 Final concluding remarks

The overall summary of this research work shows the preparation of mono and co-doped carbon nanomaterials and their electrocatalytic activity toward oxygen reduction reaction in alkaline medium. These materials may have other applications but in terms of fuel cells devices, they have been tested and specially designed to work in alkaline environment such as in Alkaline fuel cells.

Herein, we successfully synthesized mono (nitrogen/or sulfur) and co-doped (nitrogen and sulfur) carbon catalysts from the precursors of polyaniline, poly(3,4-ethylenedioxythiophene), and polythiophene using silicon dioxide and silicon nitride as templates. The as synthesized materials were characterized by TEM, SEM, XRD, Raman, XPS, and BET and electrochemical techniques such as CV and LSV.

We found that the alteration in synthesis process of materials in terms of the selection of carbon source (conductive polymers), polymerization, templates, and carbonization temperature play critical role in morphological structure and electrocatalytic properties of the final material. For example, the silicon nitride templates with PANI resulted in coral-like structure after carbonization while the silicon dioxide with PANI resulted in spherical core-shell structures under the same synthesis conditions. With respect to the electrocatalytic performances, the coral-like nitrogen doped carbon showed better oxygen reduction reaction activity than the spherical core-shell structured carbon catalysts. The good ORR performance of coral-like structured carbon catalyst could be associated with higher surface area, abundant mesoporous, and high nitrogen content.

The synthesized nitrogen and sulfur co-doped carbon catalyst demonstrated better catalytic properties than that of the nitrogen/or sulfur heteroatom doped-carbon catalysts. This behavior of co-doped carbon catalyst was attributed to the synergistic effect of dual doping agents and the regulation in the electronic structure of neighboring carbon atoms that promote facile adsorption of oxygen molecules on the active sites.

The nitrogen doped carbon showed the onset potential in the range of 0.87-0.90 V vs RHE. Sulfur doped carbon catalysts showed the onset potential in the range of 0.75-0.82 V vs RHE.

Most importantly, compared to the onset potential of the benchmark Pt/C (1 V vs RHE), our nitrogen and sulfur co-doped carbon material showed the onset potential in the range of 0.91 - 0.94 V vs RHE, which is extremely impressive.

However, boron and nitrogen co-doped carbon exhibited slightly less positive onset potential between the range of 0.78 V - 0.81 V vs RHE than that of the nitrogen and sulfur co-doped carbon.

We believe that our research work presents useful synthetic methods for the preparation of doped and co-doped carbon nanomaterials from conductive polymers towards ORR electrocatalysis in alkaline medium.

6 FUTURE WORKS

Energy is the central part of the global debate due to the drastic changes in the environment and industrial dissemination. Alternative ways of energy production are receiving considerable interest in order to reduce the dependence on conventional fossil fuel and limiting greenhouse gas emissions. Several countries in recent years have made policies in place to cut off large part of conventional fossil fuel by 2030 and encouraged the use of clean renewable systems such as fuel cell and metal air batteries in new energy vehicles. **[136]** However, such renewable energy systems are several years behind in terms of maturity.**[137]**

Beyond oxygen reduction reaction, intensive research efforts in preparation of electrocatalysts for methanol/ethanol oxidation, carbon dioxide reduction, nitrogen reduction, oxygen evolution and hydrogen evolution, have been devoted to unravel the fundamental catalytic mechanism. These reactions are the core of new renewable technologies and devices for sustainable energy production.

This research work on carbon nanomaterials derived from conductive polymers for ORR electrocatalysis, inspires us to pursue these catalyst materials in other electrochemical reactions.

For future work, we aim the development of new electrocatalyst nanomaterials from different polymer precursors via similar synthetic strategies.

7 BIBLIOGRAPHY

[1] ARMAROLI, N.; BALZANI, V., The Future of Energy Supply: Challenges and Opportunities. **Angewandte Chemie International Edition**, v.46, p. 52-66, 2007. Doi.org/10.1002/anie.200602373

[2] PAUL, R.; DU, F.; DAI, L.; ZHONG, L.; WEI, W.; ROY, F. 3D Heteroatom-Doped Carbon Nanomaterials as Multifunctional Metal-Free Catalysts for Integrated Energy Devices. **Advanced Materials**, v. 31, n.1805598, p.1-26, 2019.
Doi: 10.1002/adma.201805598

[3] SCARDAMAGLIA, M.; BITTENCOURT, C. Metal-free catalysis based on nitrogen-doped carbon nanomaterials: a photoelectron spectroscopy point of view. **Beilstein J. Nanotechnol.** v. 9, p. 2015-203, 2018.
Doi.org/10.3762/bjnano.9.191

[4] DAI, L. Carbon-based catalysts for metal-free electrocatalysis. Curr. **Opin. Electrochem.**, v.4, n.1, p.18-25, 2017.
Doi.org/10.1016/j.coelec.2017.06.004

[5] SHUI, J.; WANG, M.; DU, F.; Dai,L. N-doped carbon nanomaterials are durable catalysts for oxygen reduction reaction in acidic fuel cells **Sci. Adv.** 1,E1400129, p.1-7, 2015.
Doi: 10.1126/sciadv.1400129

[6] FENG, L. G.; SIN, X.J.; YAO, S.K.; LIU, C.P.; XING, W.; ZHANG, J.J. 3 - Electrocatalysts and Catalyst Layers for Oxygen Reduction Reaction Electrocatalysts, **Rotating Electrode Methods and Oxygen Reduction Electrocatalysts**, v. 26, n. 5, p. 67-132, 2014.
Doi.org/10.1016/B978-0-444-63278-4.00003-3

[7] GONG, K.; DU, F.; XIA, Z.; Durstock, M.; DAI, L. Nitrogen-doped carbon nanotube arrays with high electrocatalytic activity for oxygen reduction, Science, v. 323, p.760-764, 2009.
Doi: 10.1126/science.1168049

[8] BASU, R., **Ed., Recent Trends in Fuel Cell Science and Technology**, Springer, New York, p.112, 2007.

[9] SLJUKIC, B.; BANKS, C. E.; COMPTON, R. G. An overview of the electrochemical reduction of oxygen at carbon-based modified electrodes. **J. Iranian Chem. Soc.** v.2, p.1-25,2005.

[10] KHOTSEG, L.; RAY, A.; MUKHOPADHYAY, I.; PATI, R. K. Oxygen Reduction Reaction, **Electrocatalysts for Fuel Cells and Hydrogen Evolution. Theory to Design**. Intech Open ,2018.

[11] MA. R.; LIN, G.; ZHOU, Y.; LIU, Q.; ZHANG, T.; SHAN, G.; YANG, M.; WANG, J. A review of oxygen reduction mechanisms for metal-free carbon-based electrocatalysts. **Npj, computational materials**, v.7, n. 78, p.1-15, 2019.

[12] QU, L. ; LIU, Y.;BAEK, J.-B. Nitrogen-Doped Graphene as Efficient Metal-Free Electrocatalyst for Oxygen Reduction in Fuel Cells. **ACS Nano**, v.4, p.1321-1326, 2010.
Doi.org/10.1021/nn901850u

[13] QUIU, Z.; HUANG, N.; Zhang,J.; Zhou,S.; WANG, P. Fabricating carbon nanocages as ORR catalysts in alkaline electrolyte from F127 self-assemble core-shell micelle. **Int. J. Hydr. Ener**. V.44, n. 60, p. 32184-32191, 2019.
Doi: 10.1016/j.ijhydene.2019.10.066

[14] ZHANG, J.; LV, M.; LIU, D. Liu; LIANG, Z.   Nitrogen-doped carbon nanoflower with superior ORR performance in both alkaline and acidic electrolyte and enhanced durability. **Int. J. Hydr. Ener**. v. 43, i.9, n.1 p. 4311-4320, 2018.

[15] SINGH, S.K.; TAKEYASU, K.; NAKAMURA, J. Active Sites and Mechanism of Oxygen Reduction Reaction Electrocatalysis on Nitrogen-Doped Carbon Materials. **Adv. Mat.** V.31, n.13, p. 80497, 2019.
Doi: 10.1002/adma.201804297

[16] KONDO, T.; GUO, D.; SHIBUYA, R.; AKIBA, C.; SUJI, S.; NAKAMURA, J. Active sites of nitrogen-doped carbon materials for oxygen reduction reaction clarified using model catalysts. **Science**. v. 351, n. 6271, p. 361- 365, 2016.
DOI: 10.1126/science. aad0832

[17] LIU, C.; WANG, J.; HU, X.; LIN, P.; SHEN, J.; SUN, X., HAN, W. Controllable synthesis of N-doped hollow-structured mesoporous carbon spheres by an amine-induced Stober-silica/carbon assembly process. **J. Mater. Chem. A**, v. 4, 11916.
Doi: 10.1039/C6TA03748H

[18] LIANG, H.-W.; ZHUANG, X.; BRULLER, S.; FENG, X.; MULLEN, K.; Hierarchically porous carbons with optimized nitrogen doping as highly active electrocatalysts for oxygen reduction. **Nat. Commun.** V. 5, p. 4973, 2014.

[19] LIU, J.; SONG, P.; XU, W. Structure-activity relationship of doped-nitrogen (N)-based metal-free active sites on carbon for oxygen reduction reaction. **Carbon**. v.115, p. 763-772, 2017.
Doi: 10.1016/j.carbon.2017.01.080

[20] YU, H.; NING, X.; MING, J.; WANG, Q.; WANG, H.; CAO, Y.; PENG, F. Electronic synergism of pyridinic- and graphitic-nitrogen on N-doped carbons for the oxygen reduction reaction. **Chem. Sci**, v. 10, p. 1589-1596, 2019. Doi: 10.1039/C8SC04596H

[21] WANG, N.; LU, B.; LI, L.; NIU, W.; TANG, Z.; KANG, X.; CHEN, S. Graphitic Nitrogen Is Responsible for Oxygen Electroreduction on Nitrogen-Doped Carbons in Alkaline Electrolytes: Insights from Activity Attenuation Studies and Theoretical Calculations, **ACS Catalysis**, n.8, v.8, p.6827-6836, 2018. DOI: 10.1021/acscatal.8b00338

[22] TITIRICI, M. Defects win over pyridinic sites. **Nature Catalysis**. v.2, p. 642-643, 2019. Doi: 10.1038/s41929-019-0309-4

[23] JIA, Y.; ZHANG, L.; ZHUANG, L., LIU, H; YAN, X.; LIU, J.; WANG, J. Y.; TARAN, E.; DAI, L., YAO, X.; WANG, S. Identification of active sites for acidic oxygen reduction on carbon catalysts with and without nitrogen doping. **Nature Catalysis**. N.2, p.688-695, 2019. Doi: 10.1038/s41929-019-0297-4

[24] WANG, S.; IYYAMPERUMAL, E.; ROY, A.; XUE, Y; YU, D.; DAI, L. One-step scalable preparation of N-doped nanoporous carbon as a high-performance electrocatalyst for the oxygen reduction reaction. **Angew. Chem. Int. Ed**. v.50, p.11756, 2011

[25] ZHAO, Z.; LI, M.; ZHAHNG, L.; DAI, L.; XIA, Z. Design Principles for Heteroatom-Doped Carbon Nanomaterials as Highly Efficient Catalysts for Fuel Cells and Metal–Air Batteries. **Adv. Mater**. V. 27, p. 6834, 2015. Doi:10.1002/adma.201503211

[26] ZHANG.L; NIU, J; LI, M.; XIA, Z. Catalytic Mechanisms of sulfur-doped graphene as efficient oxygen reduction reaction catalysts for fuel cells. **J. Phys. Chem. C**. v. 118, 7, p. 3545-3553, 2014.

[27] KICINSKI W.; SZALA, M.; BYSTRZEJEWSKI, M. Sulfur-doped porous carbons: Synthesis and applications. **Carbon**. V. 68, p. 1-32, 2014.
Doi: 10.1016/j.carbon.2013.11.004

[28] WOLGEMUTH, S.; WHITE, R.J.; WILLINGER, M.; TITIRICI, M.; ANTONIETTI, M. A one-pot hydrothermal synthesis of sulfur and nitrogen doped carbon aerogels with enhanced electrocatalytic activity in the oxygen reduction reaction. **Green Chem**. V. 14, p. 1515, 2012.
Doi:10.1039/C2GC35309A

[29] QIE, L.; CHEN, W.; XIONG, C.; HU, C.; ZOU, F.; HU, P.; HUANG, W. Sulfur-Doped Carbon with Enlarged Interlayer Distance as a High-Performance Anode Material for Sodium-Ion Batteries. **Adv. Sci**. v.2, 12, 1500195e, 2015. Doi:10.1002/advs.201500195

[30] HU, C.; DAI, L. Carbon-Based Metal-Free Catalysts for Electrocatalysis beyond the ORR. **Angew. Chem. Int. Ed**. v. 55, p. 11736-11758,2006. Doi:10.1002/anie.201509982

[31] YANG, L.; JIANG, S.; ZHAO, Y.; ZHU, L.; CHEN, S., WANG, X., WU, Q.; MA, J., MA, Y.; HU, Z. Boron-Doped Carbon Nanotubes as Metal-Free Electrocatalysts for the Oxygen Reduction Reaction. **Angew. Chem. Int. Ed.**, 50: 7132-7135. 2011. Doi: 10.1002/anie.201101287

[32] FENG, L.; QIN, Y.; HUANG, K.; WANG, F.; YAN, Y.; CHEN, Y. Chen, Boron-, sulfur-, and phosphorus-doped graphene for environmental applications. **Science of The Total Environment**. 698, 134239,2020.
Doi: 10.1016/j.scitotenv.2019.134239

[33] ZHAO,Y.;YANG, L.; CHEN, S.; WANG, X.; MA, Y.; WU, Q.; JIANG, Y.; QIAN, W.; HU, Z. Can Boron and Nitrogen Co-doping Improve Oxygen Reduction Reaction Activity of Carbon Nanotubes? **J. Am. Chem. Soc**.v.135, 4, p.1201–1204, 2013.

[34] YANG, L.; JIANG, S.; ZHAO, L.; ZHENG, Z.; JING, M. Boron-Doped Carbon Nanotubes as Metal-Free Electrocatalysts for the Oxygen Reduction Reaction. **Angewandte Chemie**. v.123,31, p.7270-7273, 2011.

[35] FERRIGHI, L.; DATTEO, M.; DI VALENTI, Di Valent, C. Boosting Graphene Reactivity with Oxygen by Boron Doping: Density Functional Theory Modeling of the Reaction Path. **J. Phys. Chem. C**, v.118, 1, p. 223–230, 2014. Doi:10.1021/jp410966r

[36] DI VALENTIN, C.; FERRIGHI, L.; FAZIO, G. Theoretical Studies of Oxygen Reactivity of Free-Standing and Supported Boron-Doped Graphene. **Chem. Sus. Chem**, v. 9, 1061, 2016.

[37] XIONG, D.; LI, X.; FAN, L.; BAI, Z. Three-Dimensional Heteroatom-Doped Nanocarbon for Metal-Free Oxygen Reduction Electrocatalysis: A Review. **Catalysts**. v.8, i. 8, p.301, 2018.

[38] JEON, I.-Y.; ZHANG, S.; ZHANG, L.; CHOI, H.-J.; SEO, J.-M.; XIA, Z.; DAI, L.; BAEK, J.-B. Edge-Selectively Sulfurized Graphene Nanoplatelets as Efficient Metal-Free Electrocatalysts for Oxygen Reduction Reaction: The Electron Spin Effect. **Adv. Mater.** V. 25, p. 6138-6145, 2013.

[39] WANG, X.; WANG, J.; WANG, D.; DOU, S.; MA, Z.; WU, J. One-pot synthesis of nitrogen and sulfur co-doped graphene as efficient metal-free electrocatalysts for the oxygen reduction reaction. **Chem. Commun**. v.37 p. 4839-4842, 2014.

[40] YOU, C.; JIANG, X.; HAN, L.; LIN, Q.; HUA, Y.; WANG, C.; LIU, X.; LIAO, S. Uniform nitrogen and Sulphur co-doped hollow carbon nanospheres as efficient metal-free electrocatalysts for oxygen reduction. **J. Mater. Chem**, A, v.5, p.1742-1748, 2017.

[41] LIU, Z.; NIE, H.; YANG, Z.; ZHANG, J.; JIN, Z.; LU, Y.; XIAO, Z.; HUANG, S. Sulfur–nitrogen co-doped three-dimensional carbon foams with hierarchical pore structures as efficient metal-free electrocatalysts for oxygen reduction reactions. **Nanoscale**, v.5,8, p.3283-3288, 2013.

[42] ZHU, J.; LI, K.; XIAO, M.; LIU, C.; WU, Z.; GE, J.; XING, W. Significantly enhanced oxygen reduction reaction performance of N-doped carbon by heterogeneous sulfur incorporation: synergistic effect between the two dopants in metal-free catalysts. **J. Mater. Chem.**, v.4,19, p.7422-7429, 2016.

[43] SONG, Z.; LIU, W.; CHENG, N.; BANIS, M. N.; LI, X. SUN, Q.; XIAO, B.; LIU, Y. LI, R.; SUN, X. Origin of the high oxygen reduction reaction of nitrogen and sulfur co-doped MOF-derived nanocarbon electrocatalysts. **Mater. Horiz.** v.4,900-917, 2017.

[44] FENG, L.; ZHIYI, Q.; HUANG, Y; PENG, K; WANG, F.; CHEN, Y. Boron-, sulfur-, and phosphorus-doped graphene for environmental applications. **Sci. of the total environ.**, v. 698,134239, 2020.

[45] QUIN, L.; WANG, L.; YANG, X.; DING, R.; ZHENG, Z.; CHEN, X. **J. Am. Chem. Soc**. v.359, p.242-250, 2018.

[46] ROZLIVKOVA, Z.; TRCHOVA, M.; EXNEROVA, M.; STEJSKAL, J. The carbonization of granular polyaniline to produce nitrogen-containing carbon, **Synthetic Metals**.62- v.161, 11–12, 2011, p.1122-1129, ISSN 0379-6779, 2011. Doi: 10.1016/j.synthmet.2011.03.034.

[47] GONG, Y.; FEI, H.; ZHOU, X.; YANG, S.; YE, G.; LIU, Z. PENG, Z.; VAJTAI, R.; YACOBSON, B.I.; TOUR, J.M.; AJAYAM, P.M. Boron- and Nitrogen-Substituted Graphene Nanoribbons as Efficient Catalysts for Oxygen Reduction Reaction **Chem. Mat**. v.27, p.1181-1186, 2015.

[48] CHOI, C.H.; PARK, S. H.; WOO, S.I. Binary and Ternary Doping of Nitrogen, Boron, and Phosphorus into Carbon for Enhancing Electrochemical Oxygen Reduction Activity. **ACS Nano**, 2012, p.6, v.8, p. 7084-709,2012.
 DOI: 10.1021/nn3021234

[49] WU, Z.; LEI, W.; WANG, J.; WANG, D. Nitrogen and sulfur co-doping of 3D hollow-structured carbon spheres as an efficient and stable metal free catalyst for the oxygen reduction reaction. **Nanoscale**, p. 8, 19086, 2016.
Doi: 10.1039/C6NR06817K

[50] XU, Z.; ZHANG, F.; LIN, W.; ZHANG, H. Polymer network-derived nitrogen/Sulphur co-doped three-dimensionally interconnected hierarchically porous carbon for oxygen reduction, lithium-ion battery, and supercapacitor. **RSC, Adv**. P. 9, 36570, 2019.

[51] DENG, H.; LI, Q.; LIU, J.; WANG, F. Active sites for oxygen reduction reaction on nitrogen-doped carbon nanotubes derived from polyaniline. **Carbon**. v.112, p. 219-229, 2017.
Doi: 10.1016/j.carbon.2016.11.014.

[52] CHEN. C. Thermal and morphological studies of chemically prepared emeraldine-base-form polyaniline powder. **J. Appl. Polym. Sci**., 89, p.2142-2148, 2003. Doi:10.1002/app.12361.

[53] BERMEJO, J.Q.; GONZALEZ-GAITAN, C.; MORALLON, E.; CAZORLA-AMOROS, D. Effect of carbonization conditions of polyaniline on its catalytic

activity towards ORR. Some insights about the nature of the active sites, **Carbon**, v.119, p.62-71, 2017.ISSN 0008-6223.

Doi: 10.1016/j.carbon.2017.04.015

[54] GENG, D.S.; CHEN, Y.; CHEN, Y.G.; LI, Y.L.; LI, R.Y.; SUN, X.L.; YE, S.; KNIGHTS, S. High oxygen-reduction activity and durability of nitrogen-doped graphene. **Energy Environ. Sci.** v. 4, p. 760-764, 2011.

[55] LAI, L.; POTTS, J. R.; ZHAN, D.; WANG, L.; POH, C. K.; TANG, C.; GONG, H.; SHEN, Z.; LIN, J. and RUOFF, R. S. Exploration of the active center structure of nitrogen-doped graphene-based catalysts for oxygen reduction reaction. **Energy Environ. Sci**., v.5, i.7 p. 7936-7942, 2012.

Doi:10.1039/C2EE21802J

[56] ZHENG, Y.; JIAO, Y.; ZHU, Y.; LI, L. H.; HAN, Y.; DU, A.; JARONIEC, M.; QIAO, S. Z. Hydrogen evolution by a metal-free electrocatalyst. **Nat. Commun**. p.5, 3783.

[57] DAI, L.; XUE, Y.; QU, L.; CHOI, H.-J.; BAEK, J.-B. Metal-Free Catalysts for Oxygen Reduction Reaction. **ACS Nano**. 2015 115, p. 4873-4892.

[58] DENIS, P. A.; FACCIO, R.; MOMBRU, A. W. Is It Possible to Dope Single-Walled Carbon Nanotubes and Graphene with Sulfur? **Chem. Phys. Chem**, v.10, p. 715-722, 2009.

Doi:10.1002/cphc.200800592.

[59] Zhang, K., Zhao, Q., Tao, Z. et al. Composite of sulfur impregnated in porous hollow carbon spheres as the cathode of Li-S batteries with high performance. **Nano Res.** v. 6, p. 38, 2013.

Doi:10.1007/s12274-012-0279-1

[60] SEVILLA, M.; FUERTES, A.B.; MOKAYA, R. Preparation and hydrogen storage capacity of highly porous activated carbon materials derived from polythiophene**. International Journal of Hydrogen Energy**. V.36, 24, 2011, p.15658-15663,2011. ISSN 0360-3199,
Doi: 10.1016/j.ijhydene.2011.09.032.

[61] SEVILLA, M.; FUERTES, A.B. Highly porous S-doped carbons. **Microporous and Mesoporous Materials. v**.158, p.318-323, 2012.
Doi:10.1016/j.micromeso.2012.02.029.

[62] XU, D.; WU, D. The role of sulfur-related species in Oxygen Reduction Reactions. **Intech Open**, 2018.

[63] WANG, H.; BO, X.; ZHANG, Y.; GUO, L. Sulfur-doped ordered mesoporous carbon with high electrocatalytic activity for oxygen reduction. **Electrochemica Acta**, p.108, p.404-411, 2013.
Doi: 10.1016/j.electacta.2013.06.133.

[64] ZHOU, Z.; ZHANG, X.; XING, L.; LIU, J.; KONG, A.; SHAN, Y. Copper-assisted thermal conversion of microporous covalent melamine-boroxine frameworks to hollow B, N-codoped carbon capsules as bifunctional metal-free electrode materials. **Electrochimica Acta**. v.298, p. 210-218, 2019

[65] INAMDAR, S.; CHOI, H-S.; WANG, P.; SONG, M.Y.; YU, J.S. Sulfur-containing carbon by flame synthesis as efficient metal-free electrocatalyst for oxygen reduction reaction. **Electrochem. Commun.** v. 30; p. 9-12, 2013.

[66] BOTTGER- HILLER, F.; MEHNER, A.; ANDERS, S.; KROLL, L.; COX, G.; SIMOD, F. Sulphur-doped porous carbon from a thiophene-based twin monomer. **Chem. Commun**. v.48, p.10568-10570, 2012.

[67] SHIN, Y.; FRYXELL, G.E; UM, W.; PARKER, K; MATTIGOD, S.V.; SKAGGS, R. Sulfur-Functionalized Mesoporous Carbon. **Adv. Funct. Mater**. v.17, p.2897-2901, 2017

[68] SEVILLA, M.; FUERTES, A.B.; VALLE-VIGON, P. Functionalization of mesostructured silica-carbon composites. **Materials Chemistry and Physics**, 139,1,15, p. 281-289, 2013.

[69] YANG,Z.; YAO, Z.; LI, G.; FANG, G.; NIE, H.; LIU, Z.; ZHOU, X.; CHEN, X. ; HUANG, S. Sulfur-Doped Graphene as an Efficient Metal-free Cathode Catalyst for Oxygen Reduction. **ACS Nano**, v. 6, 1, p. 205–211, 2012.

[70] FAN, J.J.; FAN, Y.J.; WANG, R.X.; XIANG, S.; TANG, H.J.; SUN, S.J. A novel strategy for the synthesis of sulfur-doped carbon nanotubes as a highly efficient Pt catalyst support toward the methanol oxidation reaction. **J. Mater. Chem. A**, v.5, p. 19467-19475, 2017.

[71] QIE, L.; CHEN, W.; XIONG, X.; HU, C.; ZOU, F.; HU, P.; HUANG, Y. Sulfur-Doped Carbon with Enlarged Interlayer Distance as a High-Performance Anode Material for Sodium-Ion Batteries. **Adv. Sci.** v.2, 1500195, 2015.
DOI: 10.1002/advs.201500195

[72] REN, Y.; HU, J.; ZHONG, H.; ZHANG, L. Synergistic catalytic effect of N-doped carbon embedded with Co Fe-rich $CoFe_2O_4$ clusters as highly efficient catalyst towards oxygen reduction **Journal of Alloys and Compounds**. v.837,155498, 2020

[73] MATSUSHITA, S.; YAN, B.; MATSUI, T.; KIM, J-D.; AKAGI, K. Conjugated polymer-based carbonaceous films as binder-free carbon electrodes in supercapacitors. *RSC Adv.* v.8**,** p. 19512-19523, 2018.

[74] IMAN, M.; HOGLUND, C.; JENSEN, J.; SCHIMDT, S.; IVANOV, I. G.; WILTON, R.H.; BIRCH, J.; PEDERSEN, H. Trimethyl boron as Single-Source Precursor for Boron–Carbon Thin Film Synthesis by Plasma Chemical Vapor Deposition. **J. Phys. Chem. C**. v. 120, p. 21990−21997, 2016.

[75] LIANG, M.; WANG, J.; ZHAO, M.; CAI, J.; ZHANG, M.; DENG, N.; WANG, B.; LI, B.; ZHANG, K. Borax-assisted hydrothermal carbonization to fabricate monodisperse carbon spheres with high thermostability. **Materials Research Express**, v. 6, 6, 065615, 2019

[76] LU, X.; CHEN, L. Boron-Doped Carbon Nano-/Micro balls from Orthoboric Acid-Starch: Preparation, Characterization, and Lithium-Ion Storage Properties. **Hindawi Journal of Nanomaterials**. 4987340, 8, 2018.

[77] KALIJADIS, A.; DORDEVIC, J.; TRTIC-PETROVIC, T.; VUKCEVIC, M.; POPOVIC, M.; MAKSIMOVIC, V.; RAKOCEVIC, Z.; LAUSEVIC, Z. Preparation of boron-doped hydrothermal carbon from glucose for carbon paste electrode. **Carbon**, v.95, p. 42-50, 2015.

[78] XIAO,S.; LUO, F.; HU, H.; YANG , Z. Boron and nitrogen dual-doped carbon nanospheres for efficient electrochemical reduction of N2 to NH3. **Chem. Commun.** v.56, p. 446-449, 2020

[79] QUI, Y.; ZHANG, M.; QUI, L.; QI, Y. Mechanism for the formation and growth of carbonaceous spheres from sucrose by hydrothermal carbonization. **RSC Adv**. 6, 20814-20823, 2016

[80] ZHAO, H.; LU, X.; WANG, Y. *et al.* Effects of additives on sucrose-derived activated carbon microspheres synthesized by hydrothermal carbonization. *J Mater Sci*. v. 52, p. 10787–10799, 2017.

[81] BAIK, S.; SUH, B. L.; BYEON, A.; KIM, J.; LEE, J. W. In-situ boron and nitrogen doping in flue gas derived carbon materials for enhanced oxygen reduction reaction. **Journal of CO₂ Utilization**, v. 20, p. 73-80, 2017.

[82] FERRARI, A. C.; ROBERTSON, J. Interpretation of Raman spectra of disordered and amorphous carbon. **Phys. Rev**. v. 61, n.20, 2000, p. 14096-14107,2000.

[83] NADERI, M. Chapter Fourteen- Surface area: Brunauer – Emmet – Teller (BET). **Progress in Filtration and Separation**, p. 585-608. Academic Press. Edited by Steve Tarleton, 2015.

[84] SUSI, T.; PICHLER, T.; AYALA, P. X-ray photoelectron spectroscopy of graphitic carbon nanomaterials doped with heteroatoms. **Beilstein J. Nanotechnology**. v.6, p. 177-192, 2015.

[85] CHEVION, S.; ROBERTS, M.A., CHEVION, M. The use of cyclic voltammetry for the evaluation of antioxidant capacity**. Free Radical Biology & Medicine**. v. 28, n. 6, p. 860 – 870, 2000.

[86] ARREBOLA, J.; HERAN, L.; CABALLERO, A.; MORALLES, J. Graphitized Carbons of Variable Morphology and Crystallinity: A Comparative Study of Their Performance in Lithium Cells. **Journal of Electrochemical Society.** v.156, 12, p. 986-992, 2009.

[87] C. Du, Q. Tan, G. Yin, J. Zhang. **Chapter Five: Rotating disk electrode method. Rotating Electrode Methods and Oxygen Reduction Electrocatalysts**. Edited by Xing W., Yin G., Zhang, J. p.171-198, 2014, Elsevier.

[88]KIM, M.; CHO, S.; SONG, ; SON, S.; JANG, J.; Controllable Synthesis of Highly Conductive Polyaniline Coated Silica Nanoparticles Using Self-Stabilized

Dispersion Polymerization. **ACS Appl. Mater. Interfaces**. 2012, 4, 9, p. 4603–4609.

[89] HONORATO, A. M. B.; KHALID, M.; DAI, Q.; PESSAN, L. A. Nitrogen and sulfur co-doped fibrous-like carbon electrocatalyst derived from conductive polymers for highly active oxygen reduction catalysis. **Synthetic Metals**, v. 264, 116383, 2020.

[90] ZHANG, J.; ZHAO, Z.; XIA, Z.; DAI, L.A metal-free bifunctional electrocatalyst for oxygen reduction and oxygen evolution reactions. **Nature Nanotechnology**. v.10, p. 444-452, 2015.

[91] HU, C.; DAI, L. Multifunctional Carbon-Based Metal-Free Electrocatalysts for Simultaneous Oxygen Reduction, Oxygen Evolution, and Hydrogen Evolution. **Adv. Mater.** v.29, 1604942, 2017.

[92] MALDONADO, S.; STEVENSON, K.J. Influence of nitrogen doping on oxygen reduction electrocatalysis at carbon nanofiber electrodes. **J. Phys. Chem. B.** v.109, p. 4707-4717, 2005.

[93] WANG, S.Y.; LYYAMPERUMAL, E.; ROY, A.; XUE, Y.H.; YU, D.S.; DAI, L. Vertically Aligned BCN Nanotubes as Efficient Metal-Free Electrocatalysts for the Oxygen Reduction Reaction: A Synergetic Effect by Co-Doping with Boron and Nitrogen. **Angew. Chem. Int. Ed**. v. 50, p.11756-11960, 2011. Doi:10.1002/anie.201105204

[94] HU, C.G.; XIAO, Y.; ZHAO, Y.; CHEN, Zhao, N.; ZHANG, Z.P.; CAO, M.H.; QU, L.T. Highly nitrogen-doped carbon capsules: scalable preparation and high-performance applications in fuel cells and lithium-ion batteries. **Nanoscale**. v. 5, p. 2726-2733, 2013.

[95] QU, L.T.; LIU, Y.; BAEK, J.-B.; DAI, L. Nitrogen-Doped Graphene as Efficient Metal-Free Electrocatalyst for Oxygen Reduction in Fuel Cells. **ACS Nano**, v. 49, p. 1321-1326, 2010.

[96] KARAJAGI, I.; RAMYA, K.; GHOSH, P. C.; SARKARD, C.; RAJALAKSHIMI, N. Co-doped carbon materials synthesized with polymeric precursors as bifunctional electrocatalysts. **RSC Adv**. v. 10, 35966, 2020.

[97] WANG, Z.; XU, D.; WANG, H.G.; WU, Z.; ZHANG, X.B. In Situ Fabrication of Porous Graphene Electrodes for High-Performance Energy Storage. **ACS Nano**, v.7, p. 2422-2430, 2013.

[98] EL-SAWY, A.M.; MOSA, I.M.; SU, D.; GUILD, C.J.; KHALID, S.; JOESTEN, R.; RUSLING, J.F.; SUIB, L. Oxygen Reactions: Controlling the Active Sites of Sulfur-Doped Carbon Nanotube–Graphene Nano lobes for Highly Efficient Oxygen Evolution and Reduction Catalysis. **Adv. Ener. Mater**. v.6, 1501966, 2016.

[99] ZHOU, R.; ZHENG, Y.; HULICOVA- JURCAKOVA, D.; QIAO, S.Z. Enhanced electrochemical catalytic activity by copper oxide grown on nitrogen-doped reduced graphene oxide. **J. Mater. Chem. A**. v.1, p. 13179-13185, 2013.

[100] ZHOU, R.F.; QIAO, S.Z. An Fe/N co-doped graphitic carbon bulb for high-performance oxygen reduction reaction. Chemical Communications. v. 26, p. 5868-5873.

[101] ZHENG, Y.; ZHOU, R.; JARONIEC, M.; QIAO, S.-J. Determination of the Electron Transfer Number for the Oxygen Reduction Reaction: From Theory to Experiment. **ACS Catal**. v.6, 7, 4720–4728, 2016

[102]FERNANDEZ-ESCAMILLA H.N.;GURRERO-SANCHEL, J.; CONTRERAS, G. et al. Understanding the Selectivity of the Oxygen Reduction Reaction at the

Atomistic Level on Nitrogen-Doped Graphitic Carbon Materials. **Adv. Energy Mater.** 2002459, 2020.
Doi:10.1002/aenm.202002459

[103] WU, P.; LV, H.; PENG, T.; HE, D.; MU, S. Nano Conductive Ceramic Wedged Graphene Composites as Highly Efficient Metal Supports for Oxygen Reduction. **Sci. Rep**. v.4, n. 3968, 2014.

[104] XU, J.; GONG, G.; JIN, C.; HUANG, M.; GUAN, L. Sulfur and nitrogen co-doped, few-layered graphene oxide as a highly efficient electrocatalyst for the oxygen-reduction reaction. **Chem. Sus. Chem**. v. 6, p. 493-499, 2013.

[105] BAG, S.; MONDAL, B.; DAS, A. K.; RAJ, C. R. Nitrogen and Sulfur dual-doped reduced graphene oxide: synergistic effect of dopants towards ORR. **Electrochim. Acta.** v.163, p.16-23, 2015.

[106] FERRARI, A.C.; BASKO, D.M. Raman spectroscopy as a versatile tool for studying the properties of graphene. **Nature Nanotechnology**. v. 8, p. 235-246, 2013.

[107] HOANG.V.C.; HASSAN, M.; GOMES, V.G. Gomes, Coal derived carbon nanomaterials–Recent advances in synthesis and applications. **Appl. Mater**. **Today**. 12, p. 342-358, 2018.

[108] HOUSKA, C.R.; WARREN, B.E. X-Ray Study of the Graphitization of Carbon Black. **Journal of Applied Physics**. V.25, 1503 ,1954

[109] HOANG, V.C.; NGUYEN, L.H.; GOMES, V.G. High efficiency supercapacitor derived from biomass based carbon dots and reduced graphene oxide composite. **J. Electroanalytical. Chem**. v.832, p. 87-96, 2019.

[110] LIU, X.; DAI, L. Carbon-based metal-free catalysts. **Nat. Rev. Mater.** v. 1, 16064, 2016.

[111] ZHANG, J.; XIA, Z.; DAI, L. Carbon-based electrocatalysts for advanced energy conversion and storage. **Sci. Adv**. v. 1, n. 7, e1500564, 2015.

[112] PAUL,R.; DAI, L. Interfacial aspects of carbon composites. **Composites Interfaces**. v.25, p.539-605, 2018.
Doi:10.1080/09276440.2018.1439632

[113] JIAO, Y.; ZHENG, Y.; JARONIEC, M.; QIAO, S. Z. Origin of the Electrocatalytic Oxygen Reduction Activity of Graphene-Based Catalysts: A Roadmap to Achieve the Best Performance. **J. Am. Chem. Soc.** v.136, p. 4394-4403, 2014.

[114] BIDDINGER, E. J.; KNAPKE, D. S.; VON DEAK, D., OSKANU. S. Effect of sulfur as a growth promoter for CNx nanostructures as PEM and DMFC ORR catalysts. **Applied Catalysis B: Environmental**. v. 96, i. 1-2, p.72–82, 2010.

[115] LI, J.-C.; QIN, X.; HOU, P.-X. CHENG, M.; LIU, C.; CHENG, H.-M.; SHAO, M. Identification of active sites in nitrogen and sulfur co-doped carbon-based oxygen reduction catalysts, **Carbon**. v.147, p. 303-311, 2019.

[116] ARIHARAN,A.; BALASUBRAMANIAN, V.; VAIYAPURI, N. 2016. Hydrogen storage on boron substituted carbon materials. **International Journal of Hydrogen Energy**. v.41, i.5, p.3527-353641, 2016.
Doi: 10.1016/j.ijhydene.2015.12.169.

[117] SAHOO, M.; SREENA, K.P.; VINAYAN, B.P.; RAMAPRABHU, S. Green synthesis of boron doped graphene and its application as high-performance anode material in Li ion battery. **Materials Research Bulletin**. v.61, p. 383–390, 2014. Doi: 10.1016/j.materresbull.2014.10.049

[118] WANG, D.-W.; LI, F.; CHEN, Z.-G.; LU, G. Q.; CHENG, H. -M. Synthesis and Electrochemical Property of Boron-Doped Mesoporous Carbon in Supercapacitor. **Chem. Mater**. v.20, p. 7195–7200, 2008. Doi:10.1021/cm801729y

[119] MUTUMA, B. K.; MATSOSO, B. J.; MOMODU, D.; OYEDOTUN, K. O.; COVILLE, J.; MANYALA, N. Deciphering the Structural, Textural, and Electrochemical Properties of Activated BN-Doped Spherical Carbons. **Nanomaterials**. V.9, 446, 2019. Doi:10.3390/nano9030446

[120] JAQUES, S.; GUETTE, A.; BODRRAT, X.; LANGLAIS, F.; GUIMON, C.; LABRUGERE, C. LPCVD and characterization of boron-containing pyro carbon materials. **Carbon**. v. 34, i.9, p.1135-1143, 1996.

[121] KONNO, H.; NAKAHASHI, T.; INAGAKI, M.; SOGABE, T. Nitrogen incorporation into boron-doped graphite and formation of B–N bonding. **Carbon**. v.37, p. 471–475, 1999.

[122] CAMISASCA, A.; SACCO, A.; BRESCIA, R.; GIORDANI, S. Boron/nitrogen-codoped carbon nano-onion electrocatalysts for the oxygen reduction reaction. *ACS Appl. Nano Mater*. v.1, i.10, p. 5763–5773,2018. Doi:10.1021/acsanm.8b01430

[123] PANOMSUWAN, G.; SAITO, N.; ISHIZAKI, T. Electrocatalytic oxygen reduction activity of boron-doped carbon nanoparticles synthesized via solution plasma process. **Electrochemistry Communications**. v. 59, p. 81-85, 2015. Doi: 10.1016/j.elecom.2015.07.005

[124] ZHENG, Y.; JIAO, Y.; GE, L.; JARONIEC, M.; QIAO, S. Z. Two-step boron and nitrogen doping in graphene for enhanced synergistic catalysis. **Angewandte Chemie Int. Ed.** v.52, p. 3110-3116, 2013. Doi:10.1002/ange.201209548

[125] PARTHASARATHY, N.; BUFFLE, J.; HAERDI, W. Combined use of calcium salts and polymeric aluminum hydroxide for defluorination of waste waters. **Water Research.** v.20, i.4, p.443–448, 1986. Doi:10.1016/0043-1354(86)90191-0

[126] SIMONSSON, D. Ind. Eng. Chem. Reduction of Fluoride by Reaction with Limestone Particles in a Fixed Bed. **Process Des. Dev**. v.18, i.2, p. 288–292, 1979.

[127] BENEFIELD, L.D.; JUDKINS, J.F.; WEAND, B.L. **Process Chemistry for Water and Wastewater Treatment, Prentice-Hall,** Englewood Cliffs, N.J., USA, 1982.

[128] SAHA, S. Treatment of aqueous effluent for fluoride removal. **Water Res.** v. 27, i. 8, p. 1347–1350, 1993.

[129] HU, C.Y.; LO, S.L.; KUAN, W.H.; LEE, Y.D. Removal of fluoride from semiconductor wastewater by electrocoagulation–flotation. **Water Res.** v.39, i.5, p.895–901, 2005.

[130] HU, C.Y.; LO, S.L.; KUAN, W.H. Effects of co-existing anions on fluoride removal in electrocoagulation (EC) process using aluminum electrodes, **Water Res**. v. 37, i.18, p. 4513–4523, 2003.

[131] MUKHERJEE, D.; KULKARNI, A.; GILL, W.N. Membrane based system for ultrapure hydrofluoric acid etching solutions. **J. Membr. Sci.** v.109, i.2, p. 201–211, 1996.

[132] INTO, M.; JONSSON, A.S.; LENGDEN, G. Reuse of industrial wastewater following treatment with reverse osmosis. **J. Membr. Sci.** v. 242, i.1, p. 21–25, 2004.

[133] CASTEL, C.; SCHWEIZER, M.; SIMONNOT, M.O.; SARDIN, M. Selective removal of fluoride ions by a two-way ion-exchange cyclic process. **Chem. Eng. Sci**. v. 55 i.17, p. 3341–3352, 2000.
Doi:10.1016/S0009-2509(00)00009-9

[134] LIN, S.H.; LIU, J. M. Liu, Hydrofluoric acid recovery from waste semiconductor acid solution by ion exchange. **J. Environ. Eng**. v.129, p. 472-478, 2003.
Doi:10.1061/(ASCE)0733-9372(2003)129:5(472)

[135] WONA, C.-H.; CHOI, J.; CHUNG, J. Evaluation of optimal reuse system for hydrofluoric acid wastewater. **Journal of Hazardous Materials.** v.239–240, p. 110–117, 2012.
Doi: 10.1016/j.jhazmat.2012.08.004

[136] SCHMIDT, J.; KLINGER, M.; KLOCK, C.; CAMARGO, L.R.; REGENER, P.; TURKOVSKA, E.; WEHRE, S.; WETTERLUND, E. A new perspective on global renewable energy systems: why trade in energy carriers matters. **Energy Environ. Sci.**, v.12, p. 2022-2029, 2019.
 Doi: 10.1039/c9ee00223e

[137] ARMAROLI, N.; BALZAN, V. The future of energy supply: challenges and opportunities. **Angew. Chem. Int. Ed.** v.46, p. 52 – 66, 2007.
Doi: 10.1002/anie.200602373

APPENDIX

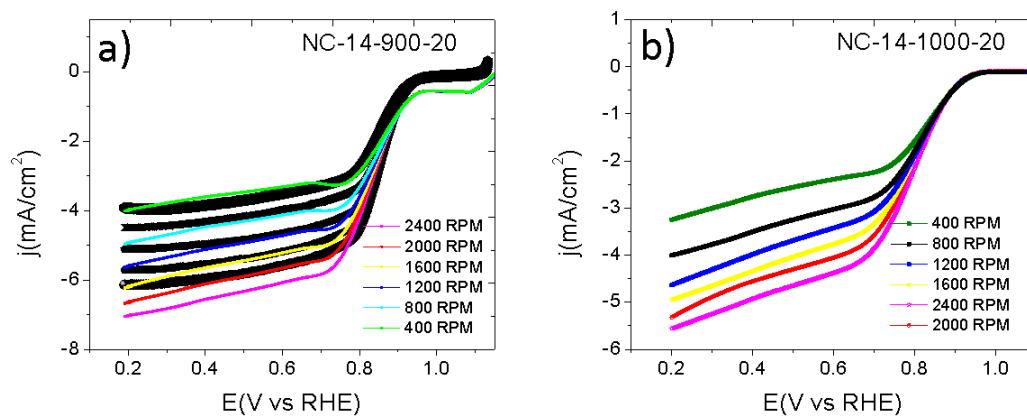Supplementary linear sweep voltammetry curves.

Figure A ‑ 1) Supplementary linear sweep voltammetry curves of NC-14-900-20, **2)** supplementary linear sweep voltammetry curves of NC-14-1000-20.

Figure B ‑ 1) Supplementary linear sweep voltammetry curves of SNC, **2)** supplementary linear sweep voltammetry curves of NC-900.
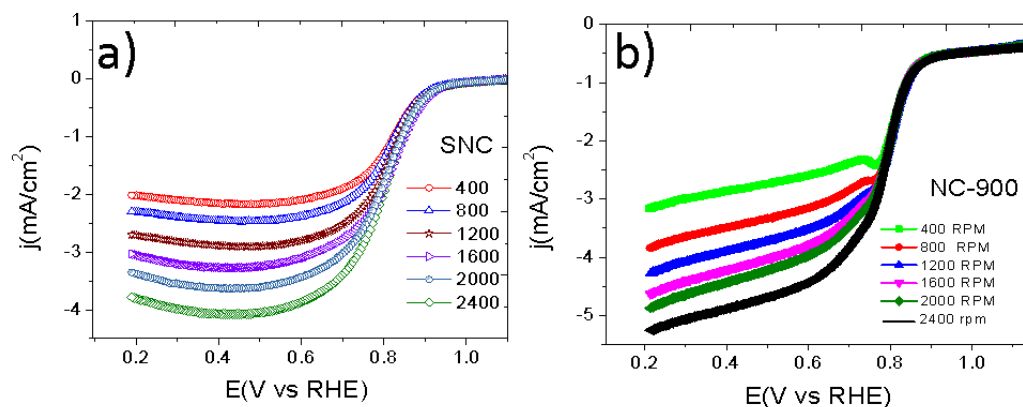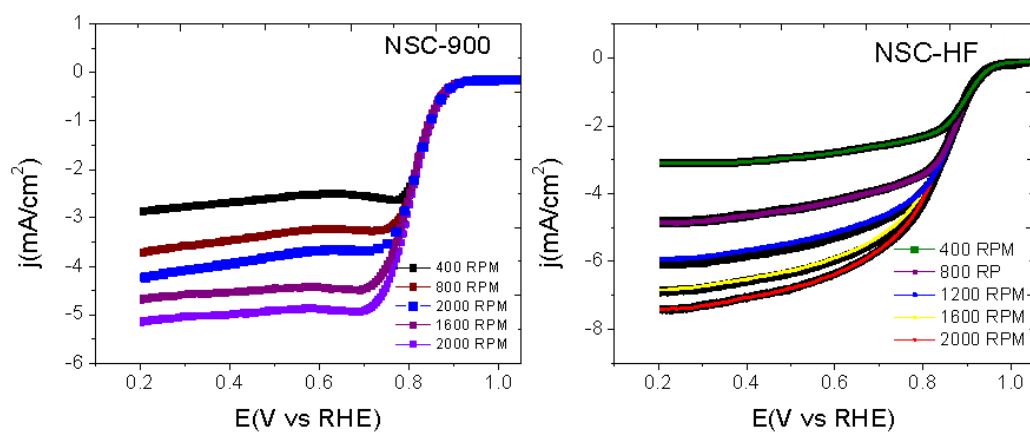
Figure C - 1) Supplementary linear sweep voltammetry curves of NSC-900,

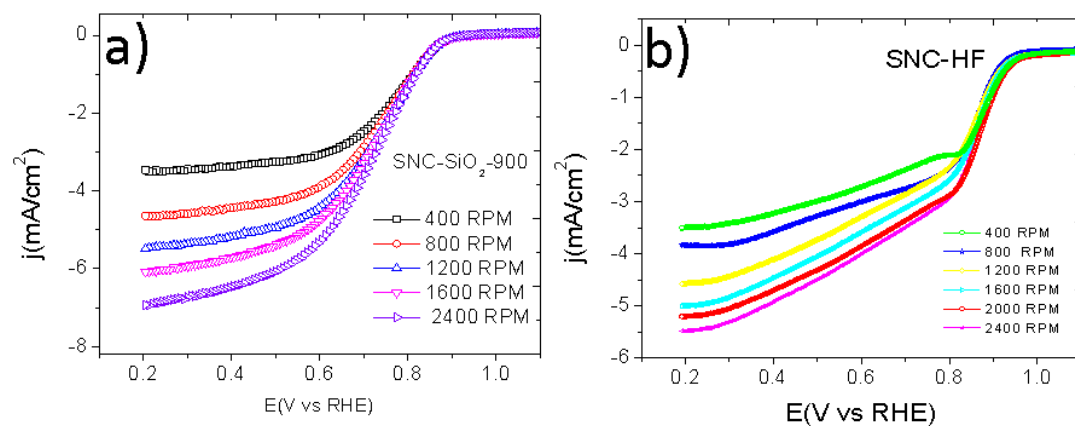 **2)** supplementary linear sweep voltammetry curves of NSC-HF.

Figure D- 1) Supplementary linear sweep voltammetry curves of SNC-SiO₂-900,

2) supplementary linear sweep voltammetry curves of SNC-HF.

Table A - Physical and electrochemical characterizations of samples NC-14-900-20, NC-14-1000-20, and SNC.

Sample	Core	Polymer	Carb. Temp.	Elem. Comp.	N-species	C-species	S-species	Surface area $m^2 g^{-1}$	H-W pot. (V vs RHE)	Onset pot.(V vs RHE)	n
NC-14-900-20	Si_3N_4	PANI	900	O:33.4%, C :26.6%, Si :21.3%, N:18.4%	Pyridinic-N:70.4% Pyrrolic-N: 29%	C=C(Sp2):57.7%, C-N/C-C (Sp3) :25.8%, C-O :16.5%		403	0.85	0.9	3.4
NC-14-1000-20	Si_3N_4	PANI	1000	O:34%, C:27%, Si: 22%, N:16.8%	Pyridinic:20.5% Pyrrolic-N: 79.5%	-C-O- :17.8%,C-N /C-C:29.6%, C=C(Sp2):52.57%		420	0.82	0.89	3
SNC	Si_3N_4	PEDOT + PANI	900	O:18% C:52%, N:13%, S:less <1% Si:16%	Pyrrolic-N:58.3%, Pyridine-N:33.5%, Quatern. -N:8.2%	C=O/C-O :28, C-N / C-C(Sp3):17%, C=C/C-C(Sp2):60%	C-S:32%, C=S:29% Oxid.-S (39%)		0.84	0.9	3.3

Table B – Physical and electrochemical characterizations of diverse samples (SiO$_2$).

Sample	Core	Pol.	Carb. Temp.	Elem. Comp.	N	C	S	HWP	OP	n
NC-900	SiO$_2$	PANI	900	N:6.2%, O:6%, C:86.80% Si:1%	Pyrr.-N:23%, Quarter.-N:72% Oxid.-N:5%	-C=C-:75.8% -C-C-:24.2		0.83	0.87-0.89	3
SNC-900	SiO$_2$	PEDOT/PANI	900	N:4.2%,C:59% O:46%,S:3.4% Si:8.1%	Pyrid.-N:15%, Pyrr.-N:11%, Quarter.-N:74%	C-C:31% C=C:58% O-C:11%	C-S/C=S: 82% Oxid-S:18%	0.80	0.88-0.89	3
SNC-HF		PEDOT/PANI	900	N:3% C:87% O:6%.S:4%	Pyrr.-N:11%, Quarter.-N:68.5% Oxid.-N:19.7%	C-C:33% C=C:53.4% O-C:13.6%	S/C=S: 74.5% Oxid-S:25.5%	.81	0.91-0.93	3.6
SC-900	SiO$_2$	PEDOT/PANI	900	Si:18.6%, S:1.1%, O:19.5%, :70.8%		C=C:71.2% C-C:17.3% C-O:11.5%	-S-C/-S=C:99% Oxi-S:1%	0.7	0.80-0.81	2.7
NSC-900	SiO$_2$	PEDOT/PANI	900	N:2.2%, S:1%, O:12.9%, C:70% Si:13.5%	Pyrid.-N:15.2% Pyrr.-N :21% Quatern. :63.8	C-C:35.6% C=C:64.4%	C-S/C=S: 96% Oxid-S:4%	0.83	0.89-0.91	3.5

Table C –Physical and electrochemical characterizations of samples BC-900, BC-1000, NBC-900 and NBC-1000.

Samp.	Precursors	Carb. Temp.	Elem. Comp.	N-species	C-species	B-species	HWP	OP	n
BC-900	Sucrose, boric acid	900	B: 3 % C: 82% O: 15%		B4C:50% C=C: 37.4% C=O:12.6%	BCO$_2$:62%, BC$_2$O: 25.4%, B-O:12.6%	0.7	0.78	2.3
BC-1000	Sucrose, boric acid	1000	B: 2 %; C: 85% O: 13%		B4C:50.5% C=C: 36.1% C=O:13.4%	BCO$_2$: 51.4%, sp2 C-B:48.6%	0.7	0.77	2.2
NBC-900	PANI, Sucrose, boric acid	900	B:1.8%; C: 82.2% O:13 % N: 3%	Pyrrolic-N:37% Pyridinic-N:41%. Quaternary-N:22%	B4C:48% C-C: 38.5% C=O:13.5	B-C :40%, BN/BC$_2$O: 31%, sp2 C-B-N:19%	0.75	0.82	2.6
NBC-1000	PANI, Sucrose, boric acid	1000	B:0.8 % C: 83.2% O: 15% N: 2%	Pyrrolic-N:49.66%. Pyridinic-N:25%. Quatern.-N:25.34%	B4C:53.7% C-C:34.8% C=O:11.4%	B-C/BC$_2$O:18% BN/BC$_2$O:60% sp2 C-B-N:22%	0.72	0.81	2.5